NONDESTRUCTIVE TESTING OF RAIL TUNNEL LININGS

A Thesis

by

NATHAN DOUGLAS WILLIAMS

Submitted to the Office of Graduate and Professional Studies of
Texas A&M University
in partial fulfillment of the requirements for the degree of

MASTER OF SCIENCE

Chair of Committee,   Stefan Hurlebaus
Committee Members,   Gary Fry
                      Alex Fang

Head of Department,   Robin Autenrieth

December 2014

Major Subject: Civil Engineering

ABSTRACT

Rail tunnel linings are currently visually inspected and hammer sounded on all structural elements at random locations or where visual inspection shows the need for it. These methods are good; however, there will not always be visual signs of problems that occur below the surface. Therefore, nondestructive testing methods need to be implemented into inspection techniques to provide information below the surface of the lining. The best approach would be to use relatively fast methods to determine potential problems and then test those areas with slow, detailed methods. This would provide a more thorough investigation of the tunnel lining's health.

Infrared thermography (IRT), ground penetrating radar (GPR), and ultrasonic tomography (UST) techniques were used to do blind testing of slabs and field testing of tunnels. Once the blind testing of the slabs was complete, the data analysis was compared to the known conditions of the slabs. This provided information on the limitations, accuracy, and ease of use for each device. The two slow, detailed methods (UST and GPR) detected all of the anomalies within the slabs when the data was analyzed together. The depths of the problems determined from the devices was fairly accurate with an average delta of 10.6 mm. The infrared camera was only able to detect the shallowest problems. The field testing provided more information on limitations and testing procedures. The first tunnels tested were the five tunnels along the Historic Railroad Trail. The tunnels were bare rock and too rough for the devices. The changes in surface area created temperature variations that limited the effectiveness of the infrared imaging. Also, one area was tested with the UST but no useful information was provided. Finally, the Moab

Tunnel was tested which had concrete lined sections. The infrared was able to locate two testing areas and one of them had an anomaly that was found with both the GPR and UST. When testing with the infrared camera, scans need to be taken traveling in both directions so that both perspectives are seen. The two detailed methods provided information on how the lining was constructed by finding the rebar and reinforcing beams. Ultimately, the methods worked well for inspecting the tunnel and the data resulted in a better understanding of the structure underneath the surface.

DEDICATION

In honor of my late grandmother, Patricia A. Williams.

ACKNOWLEDGEMENTS

NOMENCLATURE

NDT   Nondestructive Testing

IRT   Infrared Thermography

GPR   Ground Penetrating Radar

UST   Ultrasonic Tomography

TABLE OF CONTENTS

Page

LIST OF FIGURES

LIST OF TABLES

CHAPTER I

INTRODUCTION

1.1 Background

The railroad serves a vital purpose in the United States by transferring cargo and people safely across the country. Every railroad company is continually improving their safety regulations and wants to be the safest railroad. A major concern for railroads is the well-being of their tunnels. If a tunnel lining has any issues such as voiding, spalling, delaminations, excess water infiltration, or corrosion it could weaken the integrity of the lining and in the worst case result in tunnel collapse. Problems with the lining can be expensive and difficult to fix because the tunnel must be shut down, or the repair must be done around the train schedule which would increase the repair time. However, if an issue is not found or repaired in time, it could result in tunnel failure which would be even more detrimental to the rail line.

Tunnel inspection can be very time consuming and subjective due to the fact that the primary method of inspection is visual identification of defects. Visual inspections can be very difficult since most rail tunnels are not lit so inspectors must bring light into the tunnel. This makes it difficult to see the entire picture which can result in missing issues. The tunnel inspection manual also states that hammer soundings should be taken on structural components to try and detect defects under the surface (USDOT 2005). Hammer soundings are subjective since it is based on on the sound the strike makes and the inspector must know what to listen for. Also, it is unlikely that hammer soundings will detect a defect unless there is some type of surface defect that suggests something could

be hiding underneath the surface of the tunnel lining. Impact echo is a nondestructive testing (NDT) technique that is suggested by the inspection manual but not mandatory. It is also a slow method like soundings and does not cover a very large surface area resulting in a reduced likelihood of finding a defect without surface issues.

1.2 Research Objective

The objectives of this research are:

- Determine which nondestructive testing methods can be used in the inspection of concrete rail tunnel linings.
- Conduct blind NDT in a controlled setting.
- Conduct NDT on a concrete rail tunnel lining.
- Provide results with the selected methods that shows their strengths, limitations, and accuracy.

There are a lot of NDT methods used but not all of them can be used for tunnel lining inspection. For these inspections, access to only one side of the specimen is available and typically the lining is curved either at the top or both the walls and the top. Testing in a controlled setting allows for testing on known specimens which will provide accuracy results. Field testing shows that the methods can operate in a real world setting and find defects that might go unnoticed using current inspection methods.

1.3 Organization of Thesis

This thesis contains seven chapters. Chapter I provides an introduction to the research and explains the objective of the study. Chapter II presents the various tunnel lining types that are in use and the current methods of nondestructive testing along with some of their strengths and limitations. Chapter III discusses the chosen NDT methods of

testing for this project and the units that will be used. The blind testing of slabs and their results are described in Chapter IV. Chapter V discusses the testing and results that were collected on the Historic Railroad Trail's five tunnels. Chapter VI provides the background, testing, and results on the Moab Tunnel. Finally, Chapter VII presents the conclusions from the research and offers subjects for future research.

CHAPTER II

LITERATURE REVIEW

This chapter discusses the types of tunnel linings that are currently in use and various types of nondestructive testing methods that exist. It also presents research that has looked into the NDT methods strengths and weaknesses.

2.1 Tunnel Lining Types

Rail tunnel linings can be fabricated out of various materials and constructed different ways; the type of lining ultimately used is highly dependent on the excavation type. For most tunnels there will be two linings, an initially fast applied lining then a second finishing lining; however, if a tunnel boring machine is used only one lining is used (Townsend and Speers 2007). Some tunnels do not have a lining except at points where there are areas of weak rock or at portals. Tunnels that do not have a continuous liner are older railroad tunnels that primarily exist in the western mountains of the United States (USDOT 2005). Where rock is weak or has structural defects, rock reinforcement systems can be installed. These systems are composed of metal straps and mine ties that are attached to the tunnel wall with bolts or dowels. The rest of the tunnel wall may be covered in wire mesh or a thin layer of shotcrete or concrete to keep rock from spalling (USDOT 2005). Another type of lining is shotcrete which is primarily used as a temporary lining until something more permanent can be constructed, but it can be applied in multiple layers with some type of reinforcing and be used as a liner itself. If shotcrete is the final liner, it can be finished so that it will have a smooth surface giving it a cast concrete look. Ribbed systems are usually constructed in two stages and used for lining a drill-and-blast

tunnel. As the tunnel is constructed, ribs constructed from steel, concrete, or timber are placed with blocking in-between the ribs for stability. Then poured concrete is placed between the ribs as the final stage of construction. If a tunnel boring machine is used in soft ground, the primary type of lining used is a segmental lining. Each segment is prefabricated out of steel, concrete, or cast iron and erected within the tail shield of the tunnel boring machine. The segments are then bolted together compressing gaskets to provide a water tight barrier. A precast concrete tunnel lining can be seen in Figure 2.1. Placed concrete linings are a final lining that can be placed on top of any of the other types of linings mentioned above. It can be a thin layer to give the tunnel a cover or to enclose a waterproofing membrane. The concrete layer can be structural or non-structural and with or without reinforcement (USDOT 2005). Due to the fact that concrete/shotcrete is a primary part of many lining types the research will focus on the testing of concrete.

Figure 2.1. Rail tunnel with a precast segmental lining (www.railway-technology.com)

2.2 Nondestructive Testing Methods

This sections looks at the various methods of NDT testing that are currently available. It investigates how the different methods work and whether they are applicable for the testing of tunnel linings.

2.2.1 Visual Inspections

Visual inspections are the primary type of testing method used in the rail industry in the United States. The current standards for rail tunnel lining inspections is the Highway and Rail Transit Tunnel Inspection Manual, 2005 Edition. The procedure for the visual inspections are given in Chapter 4 of the Inspection Manual, and it states that all structural surfaces that are exposed must be visually inspected and all defects that are noted must be measured for their width, length, and depth (USDOT 2005). If there is anything on the surface that hampers an inspector from seeing the surface it must be cleared, such as efflorescence, debris, or corrosion. After the inspector notes the type and size of the defect; it must be categorized as to its severity. The manual (USDOT 2005) also says that one needs to pay special attention to transition areas within the tunnel looking for differential settlement. Transition areas are defined as sections of the tunnel where the support or lining of the tunnel changes or station buildings (USDOT 2005). Differential settlement often causes many of the other types of defects, which is why these areas are critical.

Visual inspections are extremely useful and will always be necessary, but they are also subjective. Also, classifying the defects can be very subjective even though the manual has the classifications defined for each type of expected defect for each material.

It is difficult to be able to see everything, and it is impossible to see past the surface of the lining.

2.2.2 Image Acquisition and Analysis

Image acquisition uses a CCD line camera to take photos of the tunnel lining and then through analysis can find and measure cracks in the surface of the lining (Ko et al. 2003). This type of device is used to enhance and minimize the subjectivity of visual scans. The camera will not tire or be distracted and miss a crack or miss measure it. In the test done by Ko et al. (2003), they used the device in a subway tunnel to find cracks in its concrete lining. An example of the results can be seen in Figure 2.2. Their system had an error rate of 70% to 80% overall and the crack measuring error was 10% or less of all recognized cracks. Therefore, Ko et al. (2003) believes it could be a viable method but needs more development.
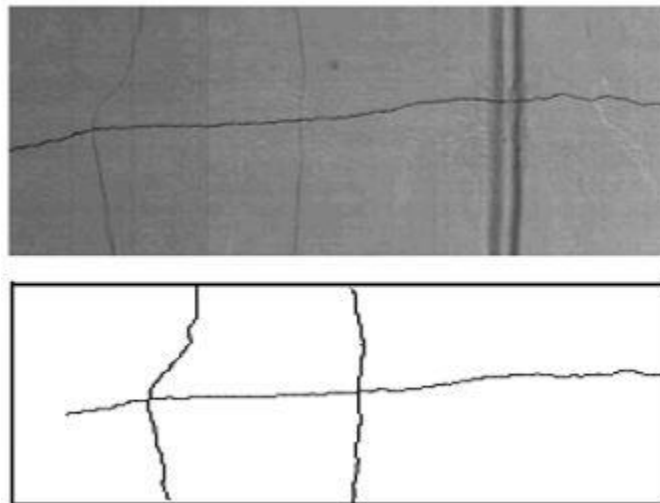
Figure 2.2. Image of cracks (top) Output of image analysis (bottom) (Ko et al. 2003)

Image acquisition and analysis would be useful; however, there are other methods that can find more than surface flaws. This type of system also requires some user inspection to be accurate at this point. With most other devices, a visual inspection would still occur but be enhanced by devices that can see passed the surface which would be a more plausible system.

2.2.3 Soundings

Hammer soundings are required by the Tunnel Inspection Manual (USDOT 2005). It states that hammer sounding must be periodically taken on all structural elements so that defects below the surface can be found. After striking the surface of the element with a hammer, the sound produced will indicate if a defect exists below the surface (USDOT 2005). If a high-pitched sound occurs then the area below the strike is good, sound material. However, a low sounding thud indicates that there is a defect below the surface. In concrete, this usually means that there is a delamination, honeycombing, or voiding below the surface at or near the sounding location (Rens and Kim 2007). Also a hollow sound in timber typically indicates that decay is present.

Sounding can be useful but only if you strike the correct spot on the element and will not work well for small voids or deep delaminations. Soundings are very subjective and do not give very much information. All it shows is that there is something below the surface but does not give any detailed information of what the defect might be.

2.2.4 Impact Echo

Impact echo uses an impulse hammer and an accelerometer mounted next to the impact location. It was developed to determine the thickness and integrity of concrete

when only one side was accessible (McCann and Forde 2001). Previously the receiver needed to be applied to the opposite side of the concrete element being tested. The results are better interpreted in the frequency domain using the Fourier transform. Then a frequency response function (FRF) is determined for the system and peaks in the frequency spectrum indicate reflections or echoes of the compression wave created by the impulse hammer (McCann and Forde 2001). The peaks that occur in the data represent the resonant frequencies of flaws or thickness. Knowing the compression wave velocity in the material, the depth to the flaw or thickness can be calculated. However, the results can be ambiguous due to the three dimensional dispersion of the impact echo wave in concrete, frequency reduction of the signal caused by surface concrete crumbling, and insufficient sensitivity of the response transducer (McCann and Forde 2001). Impact echo has been shown useful in determining the bonding state of shotcrete linings (Song and Cho 2009). By analyzing the data in both the frequency domain and time-frequency, the condition of the shotcrete could be determined as fully bonded, debonded, or voided condition. These different conditions can be more easily seen by using time-frequency analysis calculated using the short-time Fourier transform (STFT). Figure 2.3 shows the different time-frequency analyses for each of the different conditions.
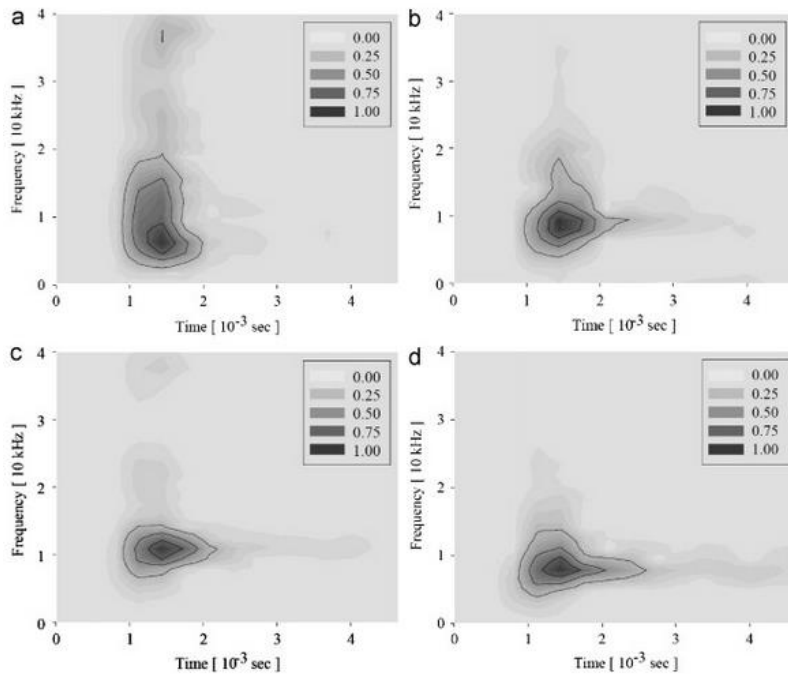
Figure 2.3. Time-frequency domain analysis results via STFT. (a) Fully bonded condition. (b) Debonded condition. (c) Void condition (shotcrete thickness = 18cm). (d) Void Condition (shotcrete thickness = 13cm) (Song and Cho 2009)

The Tunnel Inspection Manual (USDOT 2005) suggests using impact-echo with concrete or masonry surfaces of tunnel linings. This is due to impact echo's ability to find voids, deterioration, concrete thickness, and rebar debonding. A major repair can be avoided by using this method because the issue can be detected earlier and repaired much easier (USDOT 2005).

Impact echo requires trained personnel to perform the test and to interpret the data. Also, the transducer must be attached to the surface of the material using a bonding agent and the surface needs to be smooth which limits its use.

10

2.2.5 Infrared Thermography

Infrared thermography (IRT) uses specialized cameras that can convert heat at any temperature into a thermal image. Thermal images can be used to determine if concrete has any defects. If there are any cracks, delaminations, or voiding close to the surface, the concrete will heat and cool at a different rate than the surrounding concrete (McCann and Forde 2001). Therefore, a uniform image means that the concrete has no surface defects or shallow voids or delaminations, but if there are areas of differing temperature a defect could be present. The areas that are different temperatures can then be inspected closer. McCann and Forde (2001) state that infrared thermography has proven itself to be an effective preliminary survey tool to assess large buildings. In a lab test with controlled heating rates and constant ambient temperature, infrared thermography was able to detect defects up to 20 mm deep from the concrete surface (Kamoi et al. 2004). Wimsatt et al. (2013) showed that it works for tiles in road way tunnels, and one of their thermal images can be seen in Figure 2.4

The best time to use infrared thermography is during times of day when the ambient temperature is changing so that one gets the best results of the concrete area changing temperatures at differing rates. To do this in a tunnel that does not receive direct sunlight, temperature sensors should be installed in the tunnel prior to testing to collect temperature data (Wimsatt et al. 2013). From the data, an ideal time can be determined based on the greatest temperature variation. If the test is done at a different time, the temperatures could have evened out resulting in data error. Also, it can only find defects that are relatively close to the surface of the material.

11
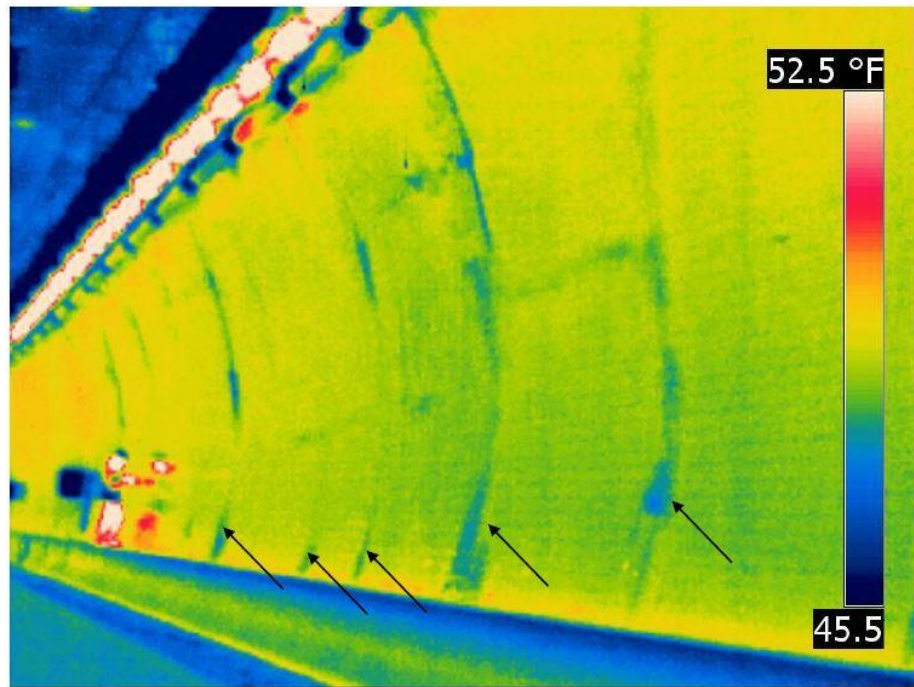
Figure 2.4. Infrared image of tiled tunnel. Areas in blue are areas of debonded tiles (Wimsatt et al. 2013)

2.2.6 Ground Penetrating Radar

Ground penetrating radar (GPR) is a system that emits electromagnetic waves at a certain frequency and receives the reflections of the wave. The frequency that the waves are emitted at has an effect on the depth of penetration and scan resolution. The lower the frequency the deeper it can penetrate but the higher frequencies give better resolution resulting in better detail (McCann and Forde 2001). Different mediums have varying electromagnetic properties; therefore, the amplitude and phase of the reflected wave will change as the wave crosses different medium interfaces (Li et al. 2011). According to Li et al. (2011), this property allows for different layers to be determined within a tunnel lining which can be seen in Figure 2.5. Then based upon the dielectric properties of the

material, arrival time, amplitude, and reflection coefficients the thickness of the layer can be determined. In another test, GPR was able to detect anomalies in a concrete water supply tunnel (Parkinson and Ekes 2008). They showed that GPR could detect honeycombing, rebar, and timber within the concrete lining (Figure 2.6), as well as liner-rock separation. A test in Italy determined that GPR was sufficient to reconstruct the interior profile of a pier and detect deformations due to strain in the structure (Orlando et al. 2010). The strain deformations were detected by the variation in amplitude deflections and wave velocity. Orlando et al. (2010) also stated that the theoretical data was useful in interpreting the data collected on the actual pier because it allowed for separation of signal and noise. Wang et al. (2012) describes GPR as a method that can successfully gauge engineering quality. They had used GPR to test a section of the Qinghai-Tibet railway tunnel; their results showed that the entire section of the tunnel had problems from thickness defects to backfill cavities. The majority of the issues were minor but there were extremely serious cavities and backfill imperfections found (Wang et al. 2012). For shotcrete, GPR works well to find voiding; however, it cannot determine the bonding condition of the rock and shotcrete (Song and Cho 2009). Another use for GPR is to determine the surface dielectric of the material which can be used to determine if there is moisture present in concrete (Rappaport et al. 2010). If moisture is present, it can be a sign that a defect is located below the surface or there is a crack in the area allowing water to penetrate the lining. GPR is a highly effective NDT method especially when it is used in conjunction with other methods (White et al. 2014).

13
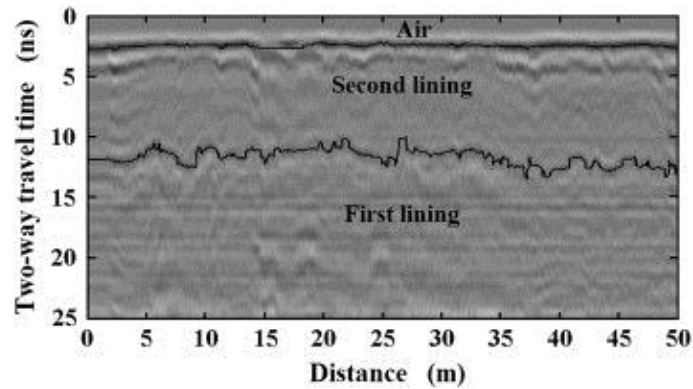
Figure 2.5. GPR scan showing multiple layers (Li et al. 2011)
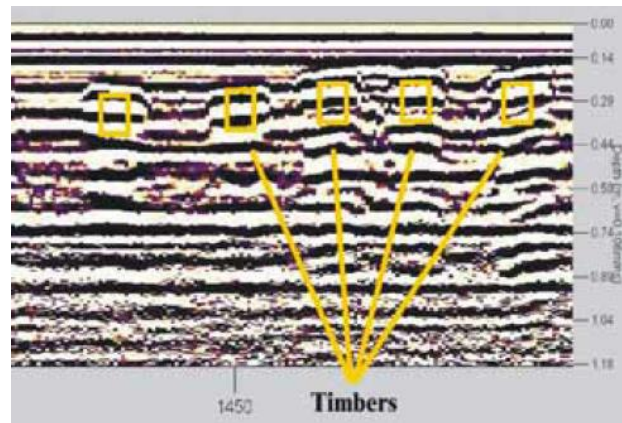
Figure 2.6. GPR scan showing timbers embedded in concrete (Parkinson and Ekes 2008)

GPR results can be difficult to interpret meaning it takes a trained technician to analyze the results. A down fall of GPR is that it cannot see through steel but is very effective in concrete and rock. The steel reflects all of the waves not allowing them to penetrate the surface. It also has problems with shotcrete if it is reinforced with steel filings or slag. However, it is a very powerful tool for detection of rebar, thicknesses, and anomalies in concrete and masonry.

14

2.2.7 Ultrasonic Tomography

Ultrasonic tomography (UST) is a relatively new technique that is based on the ultrasonic reflection method which emits ultrasonic waves through a transducer and receives the reflections through another transducer and impact echo. The ultrasonic reflection method was the first nondestructive testing (NDT) method created for testing concrete (McCann and Forde 2001); however, this method did not work well for concrete due to the material's heterogeneity and problems getting the piezoelectric transducer properly coupled to the surface to effectively conduct the ultrasonic waves. It has been used successfully for metals and in medical applications (Hoegh et al. 2011). It is also very slow to move from point to point because a coupling agent must be used to attach the transducer (McCann and Forde 2001). The ultrasonic tomography method has been developed specifically as a NDT method for concrete. The MIRA device used by Hoegh et al. (2011) has a set of transducers arranged in a four by twelve grid. In turn each row of four transducers emits ultrasonic waves and the other transducers act as receivers (Figure 2.7). By using more transducers and receivers, the device can better determine what the state of the concrete is and overcome the materials heterogeneity. It also does not need the coupling agent and can work on rough surfaces with a variation of one centimeter because the transducers are spring loaded. Hoegh et al. (2011) used the Mira system on concrete pavements and were able to find rebar, delaminations, deteriorated concrete, and the base or thickness of the pavement; examples of MIRA results can be seen in Figure 2.8. All of their findings were proven by taking cores at the tested areas which also showed the depth determined from the system to accurate.
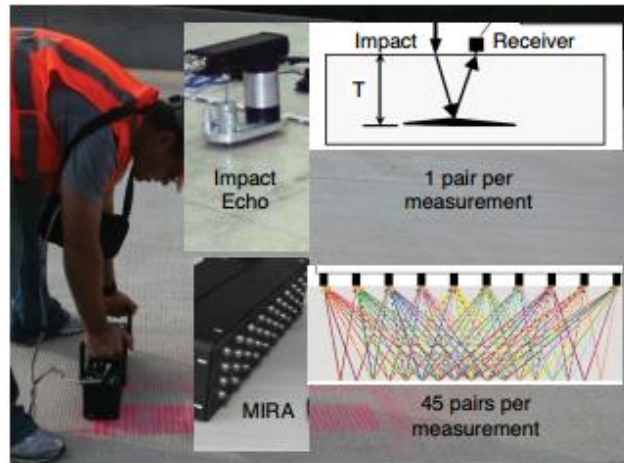
Figure 2.7. Difference between impact echo and the MIRA device (Hoegh et al. 2011)
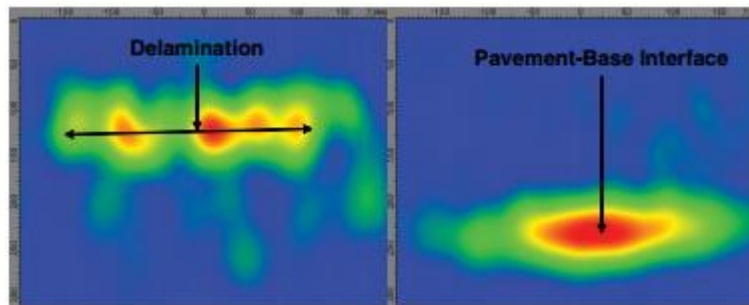
Figure 2.8. Results from the MIRA device; (left) Delamination in concrete; (right) Base or back of the concrete pavement (Hoegh et al. 2011)

Ultrasonic tomography is a very powerful tool but it does have some downfalls. It cannot see past an air gap. Therefore, if there is a fairly shallow delamination or void, the device will not be able to see what is below it. Also if the reinforcing grid is too tight the waves will be reflected and not penetrate deeper into the concrete.

2.2.8 X-ray Systems

X-ray systems are widely used in the medical industry but for scanning electrically "lossy" materials such as concrete and steel more intense radiation is required (McCann

16

and Forde 2001). These portable X-ray systems use electron linear accelerators to produce high intensity X-rays that can be used for scanning structures. They can be used to determine the interior structure of steel and concrete members up to 16 inches and 62 inches thick, respectively (Owen 1998). A seismic retrofit needed to drill cores into concrete girders without severing post-tensioned cables. A MINAC X-ray system was used to scan the girders and showed that the X-ray technology could be used to determine the location of rebar and PT cables with in the concrete as seen in Figure 2.9 (Owen 1998). Another test was done on two steel cable-stay bridges in Alaska where they scanned the cables and their anchorages. The X-ray tests showed voids and cracks in the poured zinc, but the cables and steel socket casings did not have any problems (Owen 1998).

A major issue with X-ray systems is that access to both sides of the member is required which is not possible in tunnel linings. The radiation produced is also detrimental; therefore, safety is a very big issue to deal with. In the case of the above testing, which was done in a library, it had to be done after hours so that accidental exposure would not occur.
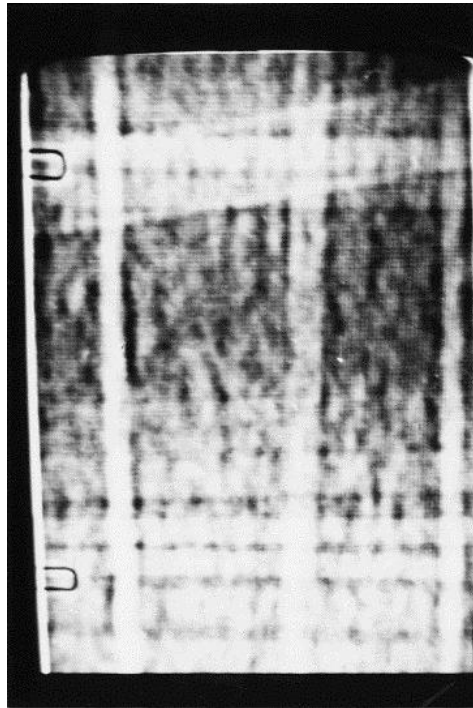
Figure 2.9. X-ray scan of girder (Owen 1998)

2.2.9 SPACETEC Scanning System

SPACETEC is a German company that specializes in the evaluation of rail and highway tunnel linings. They develop all of their own equipment and software so that it will meet the needs of their work. Their surveys use three different noncontact methods of evaluation: image recording, distance measuring, and thermal recording (SPACETEC 2014). All of the methods are completed simultaneous as they go through the tunnel; their TS3 unit can be seen in Figure 2.10. The image recording is practically a visual recording of the tunnel which is then ran through software that can determine cracking. It can find cracks as small as 0.3 mm wide, and the cracks are found based on the slight color change of each pixel that the crack runs through. To find this small of a crack, the scan must be

done at its highest resolution of 10,000 pixels which is controlled by scanning speed. For this maximum resolution, the scan must be done at a maximum of 5 km/h (SPACETEC 2014). The distance measuring uses lasers to determine the profile of the tunnel. The lasers calculate the distance to the lining and the software creates an entire profile of the tunnel. This allows for the determination of sag, movement, or differential settlement and whether the clearance tolerances are still met. SPACETEC also uses thermal recording of the tunnel to find areas of abnormal temperature differences (SPACETEC 2014). All of the data collected is provided to the client along with the SPACETEC software so the data can be examined. All three of the different measurements can be viewed individually or together to better understand the data (White et al. 2014). Viewing the data together allows for a better understanding of what could be causing anomalies.

Figure 2.10. SPACETEC TS3 tunnel scanner (SPACETEC 2014)

CHAPTER III

CHOSEN NONDESTRUCTIVE TESTING METHODS

This chapter will discuss the NDT methods chosen for testing and the specific units that will be used. The three methods that have been chosen for testing are infrared thermography, GPR, and UST.

3.1 Infrared Thermography

Infrared thermography is a fast and easy to use method. It does not require a lot of training to use to get beneficial results. It is basically like using a camera but instead of a visual image it shows temperature. From the images, temperature anomalies can be found that can represent moisture infiltration, delaminations, or shallow voiding. The primary weakness is that it can only be used to find shallow defects. The most useful time to use the device is when the ambient temperature is rising or declining at a high rate. This allows for the material to change temperature and if there is a defect or moisture then that area will change at a different rate. The uneven cooling or heating provides the anomalies that show up in a temperature profile.

The thermal device used for this research is the FLIR T640 which can be seen in Figure 3.1. It can be used for a temperature range of -40°F to 3632°F and is calibrated to an accuracy within +/- 2% of the reading. It can take individual images and video. When taking individual pictures it can be set to take a digital image along with the thermal so that the thermal image can be compared with the digital to see what is located where and if any objects would be affecting the temperature in that area. The frame rate for the camera is 30 Hz. The device will also be used in conjunction with the FLIR Tools+

program. The program allows for post processing of images and allows for video to be saved directly to a computer.

Figure 3.1. FLIR T640 thermal camera

3.2 Ground Penetrating Radar

Ground penetrating radar is a slow, detailed NDT method. It was chosen based on its usefulness and resolution in concrete. The GPR emits electromagnetic radiation and receives the reflections off of material changes due to their surface dielectric properties. The higher the frequency of the device the shallower the radiation can penetrate, but it increases resolution.

The GPR device chosen for this research is the GSSI StructureScan Mini HR, seen in Figure 3.2. It has a frequency of 2600 MHz. This frequency allows it to penetrate up to

16 inches and provide high resolution. It is also a small handheld device that weighs 3.6 pounds making it easy to travel with and use for a tunnel lining. There are lasers on three sides of the unit that line up with the antenna so the user can know where the scan is located and can mark the area if needed. The device provides the ability to do individual 2D scans or to build a grid that can be developed into a 3D scan. It has preprogrammed grid sizes in the device that match provided grids or using the software, RADAN, provided by GSSI a custom grid can be used. The RADAN software also allows for post processing of the collected data.

Figure 3.2. GSSI StructureScan Mini HR GPR device

3.3 Ultrasonic Tomography

Ultrasonic Tomography is another slow method that provides high resolution. It emits ultrasonic shear waves and receives the reflection. The primary cause for the

reflected waves is a density change. Also shear waves cannot propagate through the air, therefore, a strong reflection is created when there is debonding or voiding.

The unit used in the research was the A1040 MIRA device seen in Figure 3.3. It is small and light weight making it easy for travel and was developed for use on concrete structures. The device has 48 transducers that are aligned in twelve rows of four. The center frequency can be set at 25, 50, or 85 kHz. The device can be used to test on depth of 50 to 2000 mm. The software in the device uses the synthetic aperture focusing technique (SAFT) which allows the device to create a 2D image based on the transit time measurements. When the device is used on a grid a 3D image can be obtained by using the IDEALviewer software on a computer.

Figure 3.3. A1040 MIRA UST device

CHAPTER IV

BLIND TESTING OF SLABS

Chapter IV will discuss the testing of slabs with known defects. The slabs were created for another project and are unknown before testing. Test results will be presented and compared to the known defect types and locations.

4.1 Slab Specimens

The 24 slabs were constructed with various voids, delaminations, and reinforcement so that testing methods could be verified. Therefore, this research project is using them for the same reason but the locations of the problems and reinforcement were unknown prior to testing and data analysis for this project. Concrete was used to construct 11 of the slabs, and 13 were shotcrete. They were all 6' x 6' and located at Texas A&M's Riverside campus, and an overview image of the slabs can be seen in Figure 4.1.

Figure 4.1. Overview of slabs

4.2 Slab Testing

This section will discuss how each method was used. It will also provide information on what user inputs were used for each device.

4.2.1 Testing with UST

The MIRA unit was used twice on the slabs. Once the horizontal axis (Figure 4.2) was oriented east and west, and the other time it was oriented north and south. Testing in both directions provides better results because the resolution is better along the horizontal axis. The unit was used on a grid that covered the entire slab with the device overhanging along the horizontal axis so the end of the slab could be determined. The grid spacing was 50 mm in the vertical direction and 150 mm in the horizontal direction for both testing directions. For each slab an average wave velocity was determined and used for both tests on that slab, and they can be seen in Table 4.1. The unit frequency was set to 50 kHz for all scans.
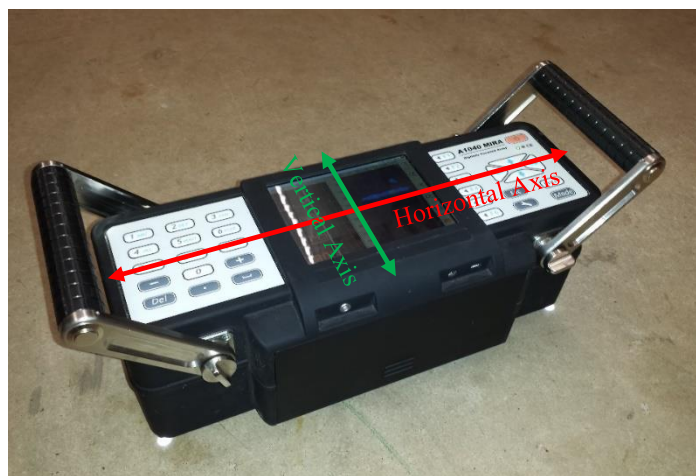

Figure 4.2. MIRA axes

Table 4.1. Slab wave velocities

Concrete Slabs		Shotcrete Slabs	
Name	Wave Speed (m/s)	Name	Wave Speed (m/s)
Alpha	2998	A	2305
Beta	2800	B	2335
Gamma	2930	C	2293
Delta	2980	D	2388
Epsilon	2948	E	2445
Zeta	2893	F	2513
Eta	2698	G	2358
Theta	2645	H	2313
Iota	2483	I	2413
Kappa	2695	J	2473
Lambda	2573	K	2443
		L	2410
		M	2383

4.2.2 Testing with GPR

The GPR unit was used on its 3D scan setting with a GSSI provided 4' x 2' grid with 2" spacing which can be seen in Figure 4.3. The grid was placed in the center of the slab for scanning. The dielectric used for all slabs was 8. The depth setting was set at a value that was at least 2" deeper than the actual depth except for the concrete slabs that were 24" thick because the maximum depth for the unit was 20". Once the settings were ready, the device was run across each grid line in both directions, and then the data was downloaded to a computer for processing.
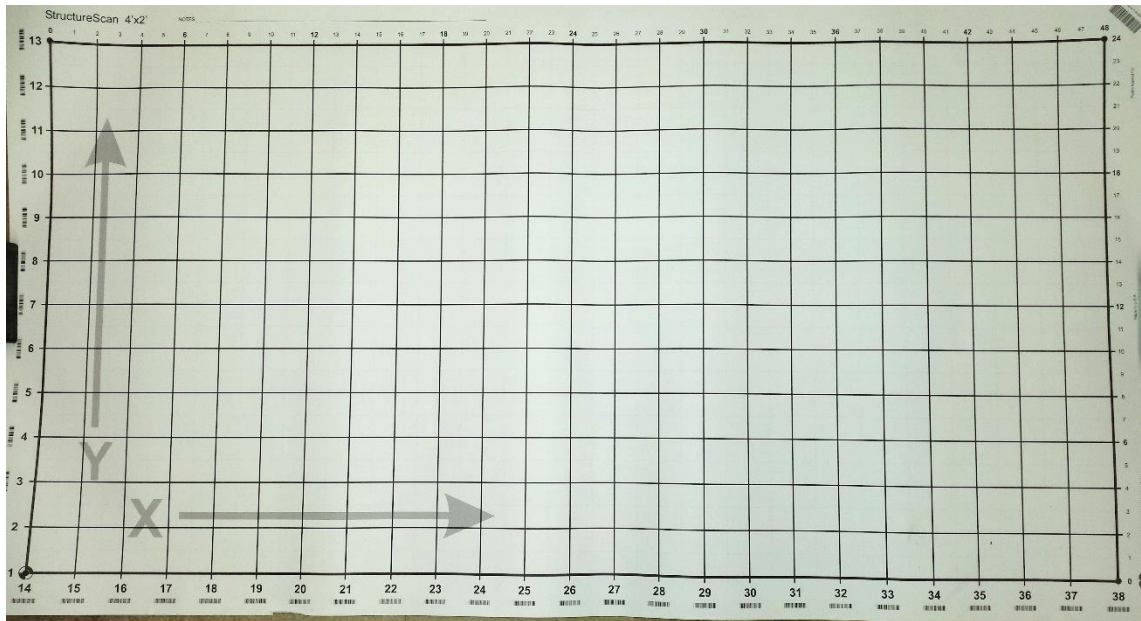
Figure 4.3. GSSI 4' x 2' grid

4.2.3 Testing with IRT

The infrared camera was used to take images of all the slabs between around 3:00 PM on November 11 during the testing of the slabs with the other methods. After testing was complete and the data had been analyzed, some of the slabs were tested again. This time 8 slabs were chosen that had the best chance of their defects being detected by infrared. They were chosen based on the depth and type of their defect. Testing was done at 9:00 AM, 11:00 AM, 12:00 PM, 1:00 PM, and 2:00 PM on June 5, 2014. The temperature and cloud cover was recorded at each time. This allowed for the determination of the best time and conditions for testing the slabs.

4.3 Slab Results

This section presents the results of all the testing done on the 24 slab specimens. An overview of all the results can be seen in Table 4.2. The actual built conditions can be seen in Table 4.3.

Table 4.2. Results from slab testing

Specimen	Material	Specimen Depth (mm)	Reinforcement Depth*		Defect	
			Top Layer (mm)	Bottom Layer (mm)	Type	Depth (mm)
Alpha	Concrete	325	None	None	None	---
Beta	Concrete	450	121	376	None	---
Gamma	Concrete	300	127	236	None	---
Delta	Concrete	636	None	None	None	---
Epsilon	Concrete	620	129	None	None	---
Zeta	Concrete	367	121	291	None	---
Eta	Concrete	369	124	312	Delamination	72
Theta	Concrete	367	127	294	Delamination	98
Iota	Concrete	355	124	271	Delamination	34
Kappa	Concrete	375	127	274	Void	210
Lambda	Concrete	367	118	268	Void	213
A	Shotcrete	98	None		None	---
B	Shotcrete	144	None		None	---
C	Shotcrete	188	None		None	---
D	Shotcrete	291	170		Void	182
E	Shotcrete	291	156		Void	196
F	Shotcrete	297	164		Void	78
G	Shotcrete	277	147		Void	83
H	Shotcrete	268	150		Delamination	190
I	Shotcrete	283	158		Delamination	95
J	Shotcrete	289	167		Delamination	83
K	Shotcrete	280	156		Delamination	68
L	Shotcrete	277	150		Delamination	15
M	Shotcrete	277	158		None	---

* Concrete reinforcement layers are believed to be mat reinforcement, and the shotcrete slabs seem to have a single girder reinforcement in the lateral direction at the specified depth

28

Table 4.3. Slab as built conditions

Specimen	Material	Specimen Depth (mm)	Reinf. Detail (mm)	Defects	True Depth of Defects (mm)
Alpha	Concrete	305	None	None	N/A
Beta	Concrete	457	127*	Natural Crack	N/A
Gamma	Concrete	305	127*	None	N/A
Delta	Concrete	610	None	None	N/A
Epsilon	Concrete	610	127*	None	N/A
Zeta	Concrete	381	127*	None	N/A
Eta	Concrete	381	127*	0.05 mm thin plastic	51
Theta	Concrete	381	127*	0.05 mm thin plastic	76
Iota	Concrete	381	127*	0.05 mm thin plastic	25
Kappa	Concrete	381	127*	Air-filled void (13mm foam)	203
Lambda	Concrete	381	127*	Water-filled void (Ziploc bag)	203
A	Shotcrete	102	None	None	N/A
B	Shotcrete	152	None	None	N/A
C	Shotcrete	203	None	None	N/A
D	Shotcrete	305	**	Air-filled void (13mm foam)	193
E	Shotcrete	305	**	Water-filled void (Ziploc bag)	191
F	Shotcrete	305	**	Air-filled void (13mm foam)	76
G	Shotcrete	305	**	Water-filled void (Ziploc bag)	76
H	Shotcrete	305	**	0.25 mm thin cloth	203
I	Shotcrete	305	**	0.25 mm thin cloth	102
J	Shotcrete	305	**	0.25 mm thin cloth	76
K	Shotcrete	305	**	0.25 mm thin cloth	51
L	Shotcrete	305	**	0.25 mm thin cloth	25
M	Shotcrete	305	**	None	N/A

*Two mats of No. 5 Rebar, at depth from top and bottom, 203 mm on center

**One lattice girder in center of slab, sitting on bottom form

4.3.1 UST Results

The images produced by the A1040 MIRA are color coded based on the reflective intensity with dark blue being no reflection and red being high reflectivity. The green and yellow colors are in between the blue and red. This device worked well in determining all the various defects that were in the concrete and shotcrete slabs. Figure 4.4 shows a C-scan and B-scan of a delamination and void in concrete slabs, and Figure 4.5 is the same but in shotcrete slabs.

The UST images for the concrete slabs are clearer than the ones for the shotcrete. This is likely due to poor construction of the shotcrete slabs due to the placement method. The top area did not get vibrated properly resulting in groups of air pockets which resulted in the images having a green spotting at the top of the B-scan. Also, the back wall can be seen in the B-scans, but the back wall does not show up in the scan beneath the defect area because the shear waves cannot pass through the defects. Another area to note is the almost black sections on the left and right edges of the images, these are due to the MIRA device hanging off the edge of the slab. This provides a reference for the edge of the slab.
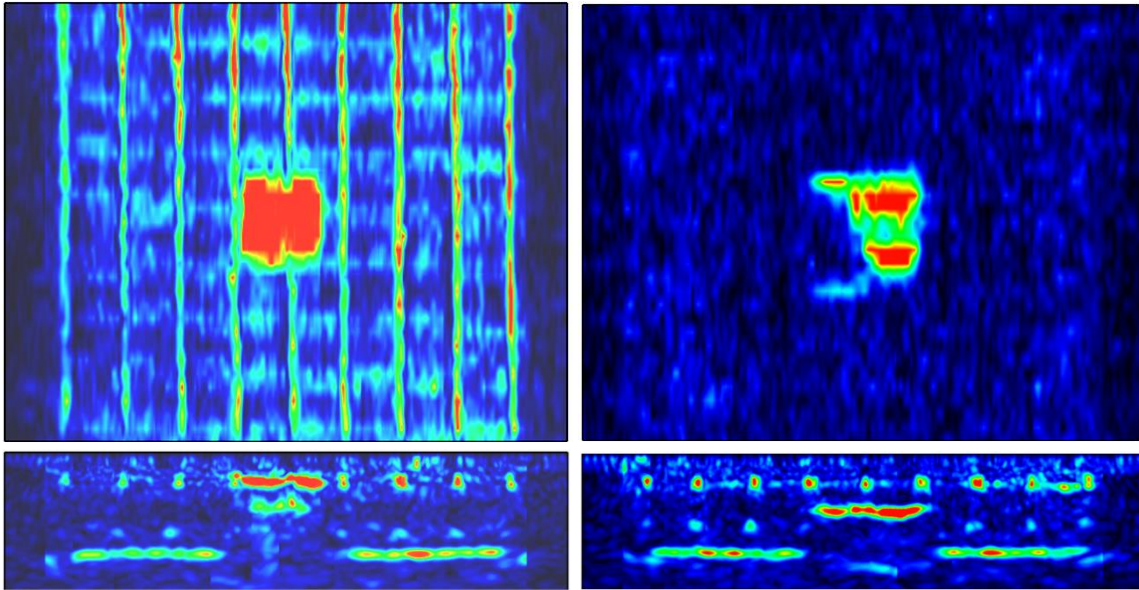
Figure 4.4. UST scans of concrete slabs: Specimen Theta with delamination C-scan at depth of 98 mm (top left), Specimen Theta B-scan at 850 mm (bottom left), Specimen Lambda with void C-scan at depth of 213 mm (top right), Specimen Lambda B-scan at 650 mm (bottom right)
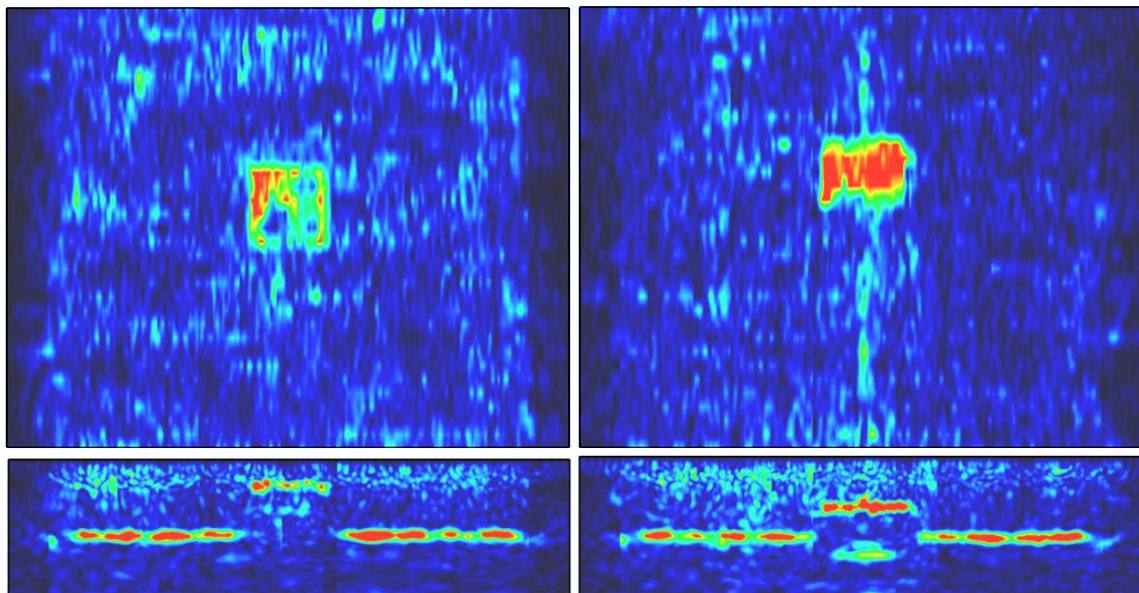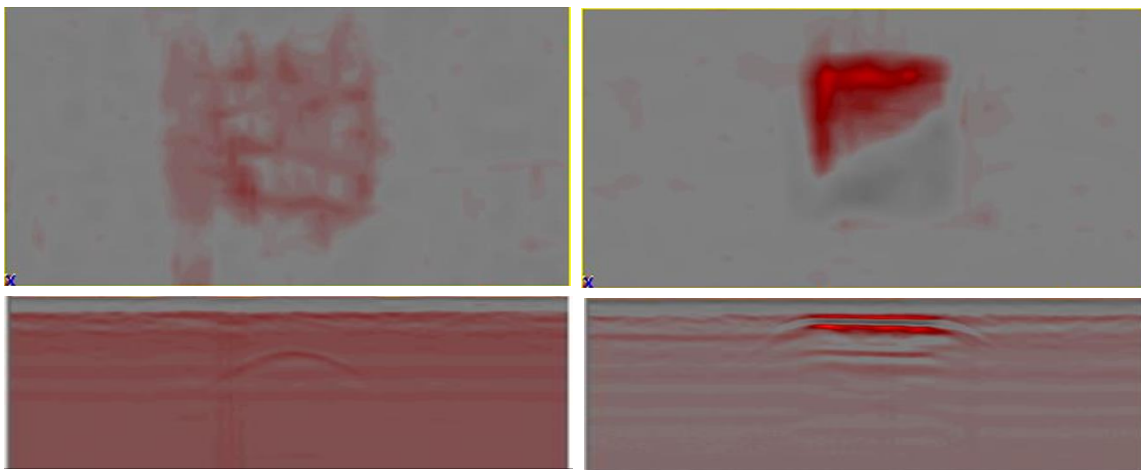

Figure 4.5. UST scans of shotcrete slabs: Specimen I with delamination C-scan at depth of 95 mm (top left), Specimen I B-scan at 700 mm (bottom left), Specimen D with void C-scan at depth of 182 mm (top right), Specimen D B-scan at 550 mm (bottom right)

4.3.2 GPR Results

The GPR worked well for finding rebar and some of the voids and delaminations. It only found two of the delaminations in the concrete slabs and one definitively in the shotcrete slabs, and they were difficult to find. The UST data was looked at first and then the GPR data so that there would be a reference and an area to look in. The images for the GPR are color coded with grey meaning no reflection and the red color gets darker with more reflectivity. Also if the reflectivity is very high it will turn yellow and go through multiple colors with white being the highest. Figure 4.6 shows C-scans for two concrete slabs, one with a void, and one with a delamination. Figure 4.7 is the same type of image but for shotcrete slabs and with B-scans.

The B-scans are not shown for the concrete slabs because they do not show anything but the rebar similar to the B-scan of Specimen L. The parabola in the B-scan of Specimen L is the girder reinforcement used in the shotcrete slabs. However, the void in Specimen F can be seen in the B-scan which is due to the shallowness of the void. The void in Specimen G which is at the same depth as Specimen F's void can also be seen in the B-scan but is not shown here.
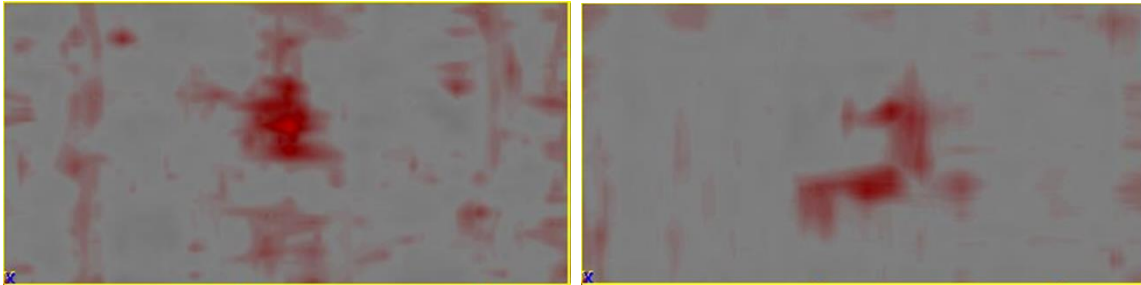
Figure 4.6. GPR C-scans of concrete slabs: Specimen Iota with delamination (left) Specimen Kappa with void (right)

Figure 4.7. GPR scans of shotcrete slabs: Specimen L with delamination C-scan at 15 mm (top left) Specimen L B-scan at 305 mm (bottom left) Specimen F with void C-scan at 78 mm (top right) Specimen F B-scan at 305 mm (bottom right)

4.3.3 IRT Results

Infrared thermography worked well for the shallow defects in the shotcrete slabs. During the initial scan, it detected a possible issue in 3 of the 13 shotcrete slabs but none in the concrete slabs. This is believed to be due to the difference in the slab's color. The concrete slabs are lighter than shotcrete slabs; therefore, the concrete slabs do not absorb as much light and heat from the sun. The three infrared images showing problems can be seen in Figure 4.8.

The second IRT testing was done at various times throughout the day on Specimens Eta, Iota, Kappa, Lambda, F, G, K, and L. Only one slab showed anything at the first scan at 9:00 AM. At 11:00 AM, nothing was visible on any of the slabs. From 12:00 PM to 2:00 PM, defects started to be able to be seen with four being detected at 2:00 PM. This testing allowed for one of the defects in a concrete slab to show up in the image. It was Specimen Iota which has a delamination at a depth of 25 mm. Table 4.4 lists the conditions at the various times of testing, and Figure 4.9 through 4.13 shows the four slabs that a defect was detected in at each testing time.

Table 4.4. Conditions at time of testing

Time	Temperature (°F)	Cloud Cover (%)
9:00 AM	77	100
11:00 AM	80	100
12:00 PM	82	100
1:00 PM	84	80
2:00 PM	86	70
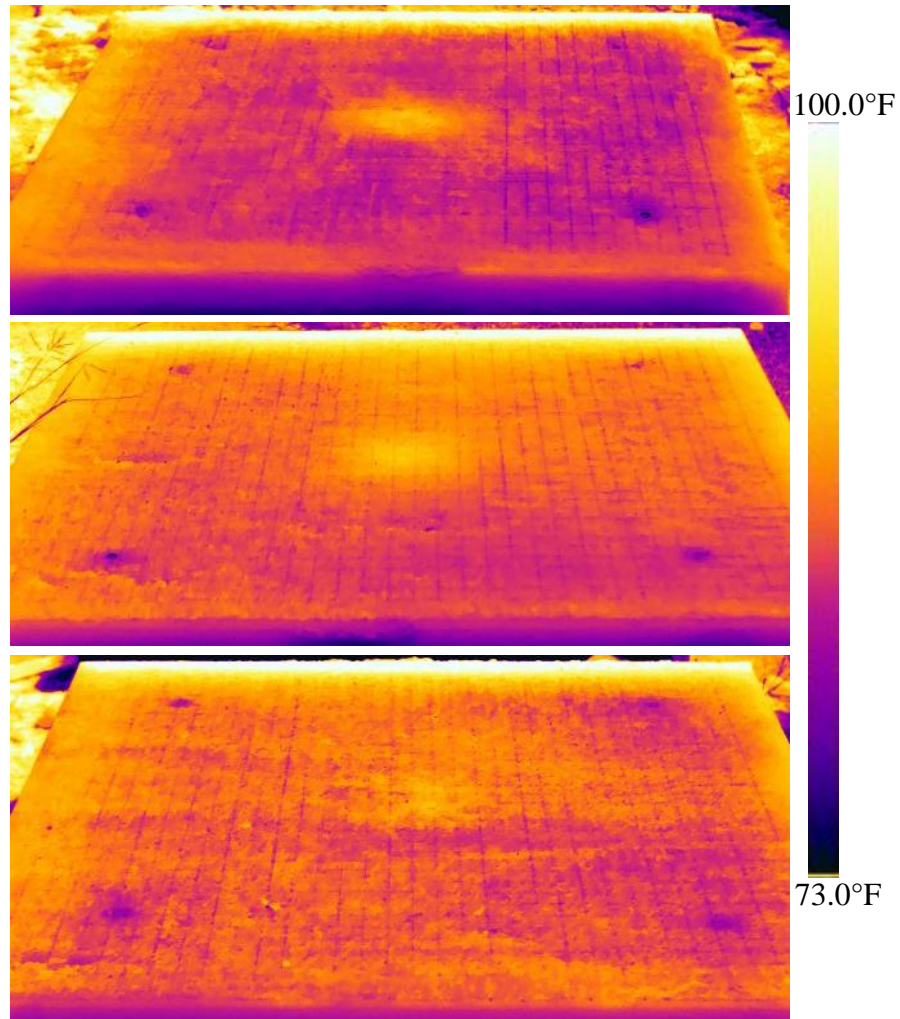
Figure 4.8. IRT images: Specimen F (top), Specimen G (middle), and Specimen L (bottom)

Specimen F is cooler in the middle where the void is located. The ambient temperature has not warmed enough at that point in the morning so the differential cooling is still evident. Specimens L and F look like there may be something showing but it is not definitive. In Figure 4.10 which is two hours later, the temperatures have evened out so that there is no evidence of a defect on any slab.
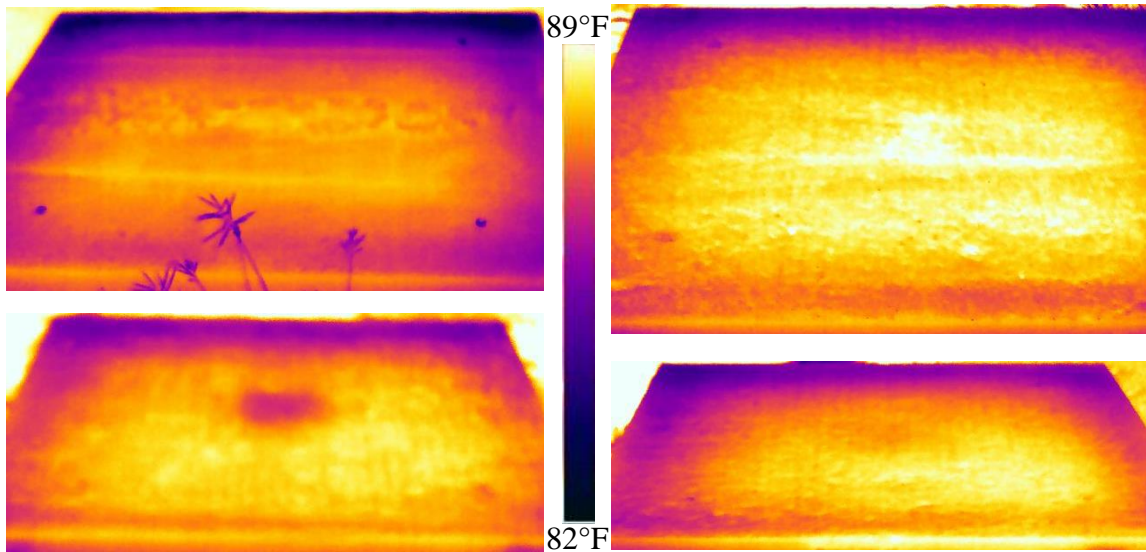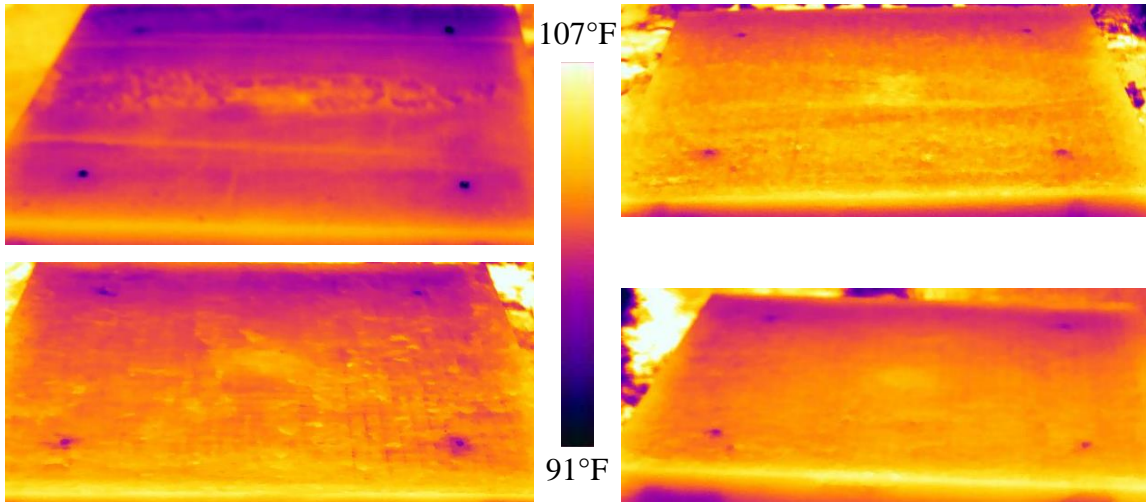
Figure 4.9. 9:00 AM Thermal images: Specimen Iota (top left), Specimen L (top right), Specimen F (bottom left), Specimen G (bottom right)
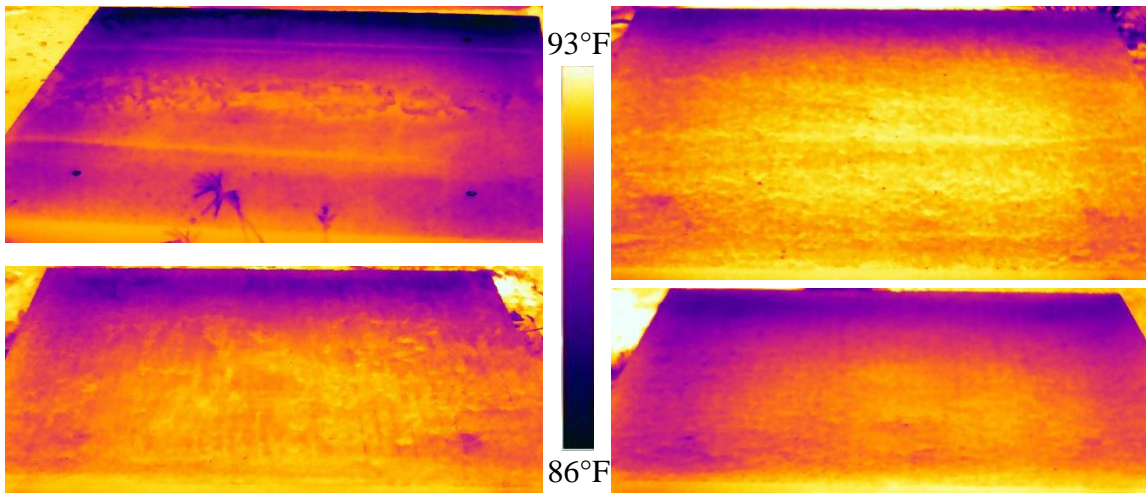
Figure 4.10. 11:00 AM Thermal images: Specimen Iota (top left), Specimen L (top right), Specimen F (bottom left), Specimen G (bottom right)

The scans at noon are still a consistent temperature over the slab. Specimen L is starting to look like there may be something, but it cannot be certain. However, in the next scans the cloud cover started to diminish which allowed the sun to heat the slabs some.

This allows for an increased heat flux into the slabs creating a greater temperature differential over the defects. Resulting in more of the defects becoming detectable with IRT.

The scans at 2:00 PM (Figure 4.13) show all the defects in the four slabs. This was due to the sun coming out around 1:00 PM and allowing the slabs to warm. However, this will not work for tunnels because there will not be a heat source other than the ambient temperature. Therefore, the testing of a tunnel needs to occur during the steepest slope of temperature change of the ambient temperature within the tunnel. This will be when the concrete is warming or cooling the most and a temperature differential will develop in the concrete. Also, the only defects that were detectable were delaminations around 25 mm deep or voids about 80 mm deep. So IRT will only be able to detect shallow defects.
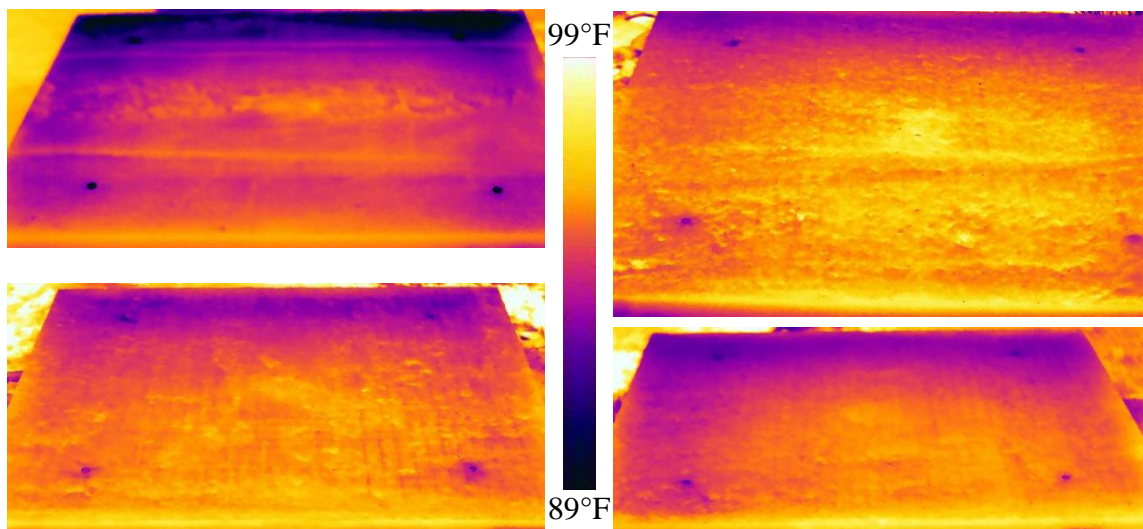
Figure 4.11. 12:00 PM Thermal images: Specimen Iota (top left), Specimen L (top right), Specimen F (bottom left), Specimen G (bottom right)

Figure 4.12. 1:00 PM Thermal images: Specimen Iota (top left), Specimen L (top right), Specimen F (bottom left), Specimen G (bottom right)
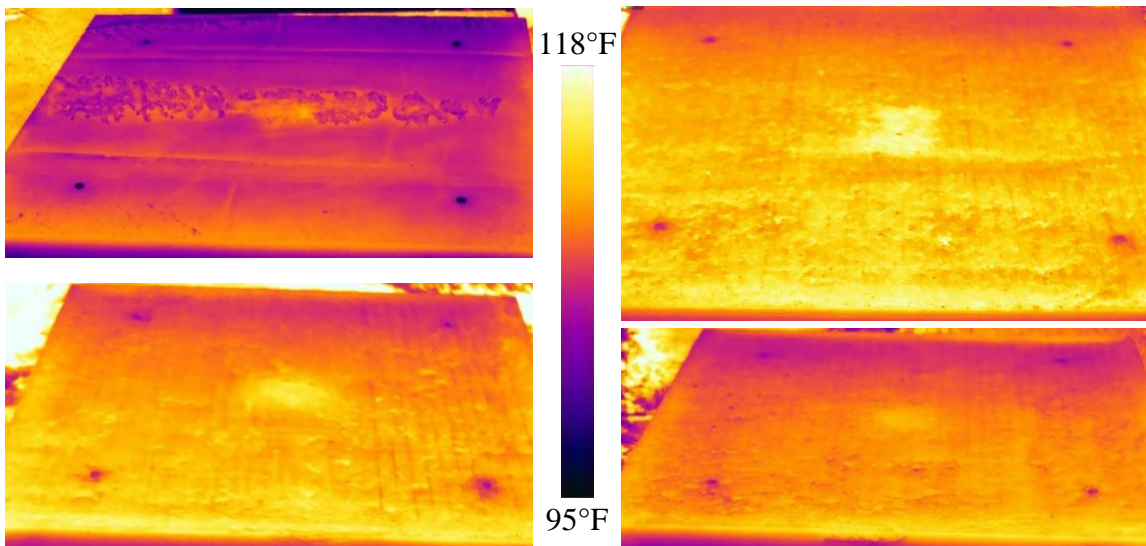
Figure 4.13. 2:00 PM Thermal images: Specimen Iota (top left), Specimen L (top right), Specimen F (bottom left), Specimen G (bottom right)

CHAPTER V

HISTORIC RAILROAD TRAIL

Chapter V will discuss the background of the Historic Railroad Trail, the testing of the tunnels, and the results from testing. The results will provide information on the use of UST and IRT on rock tunnels that do not have a lining.

5.1 Background

The Historic Railroad Trail has five tunnels along the path. They were a part of the rail line that was constructed in 1931 by Lewis Construction Company for rail access to the Hoover Dam construction project. They were completed in only five months. The railroad was last used in 1961 and then the tracks were dismantled and sold in 1962 (National Park Service 2014). It was then turned into a hiking trail for tourists. A map of the trail can be seen in Figure 5.1.

The five tunnels are primarily rock with no lining. They do have some rock bolts and tunnel one, two, and three have wooden vertical supports with parts covered by wood plank to prevent rock from falling onto the tracks (National Park Service 2014). The tunnels are 18 feet wide and 27 feet tall so that the trains could hall the large equipment needed for the Hoover Dam project. Tunnel two was burned in 1990 due to an arson fire and was then sprayed with shotcrete because the rock was loosened due to the heat. Tunnel five burned in 1978 and was closed but then reopened in 2001 after it was remodeled (National Park Service 2014). Tunnels 2 and 5 can be seen in Figure 5.2.
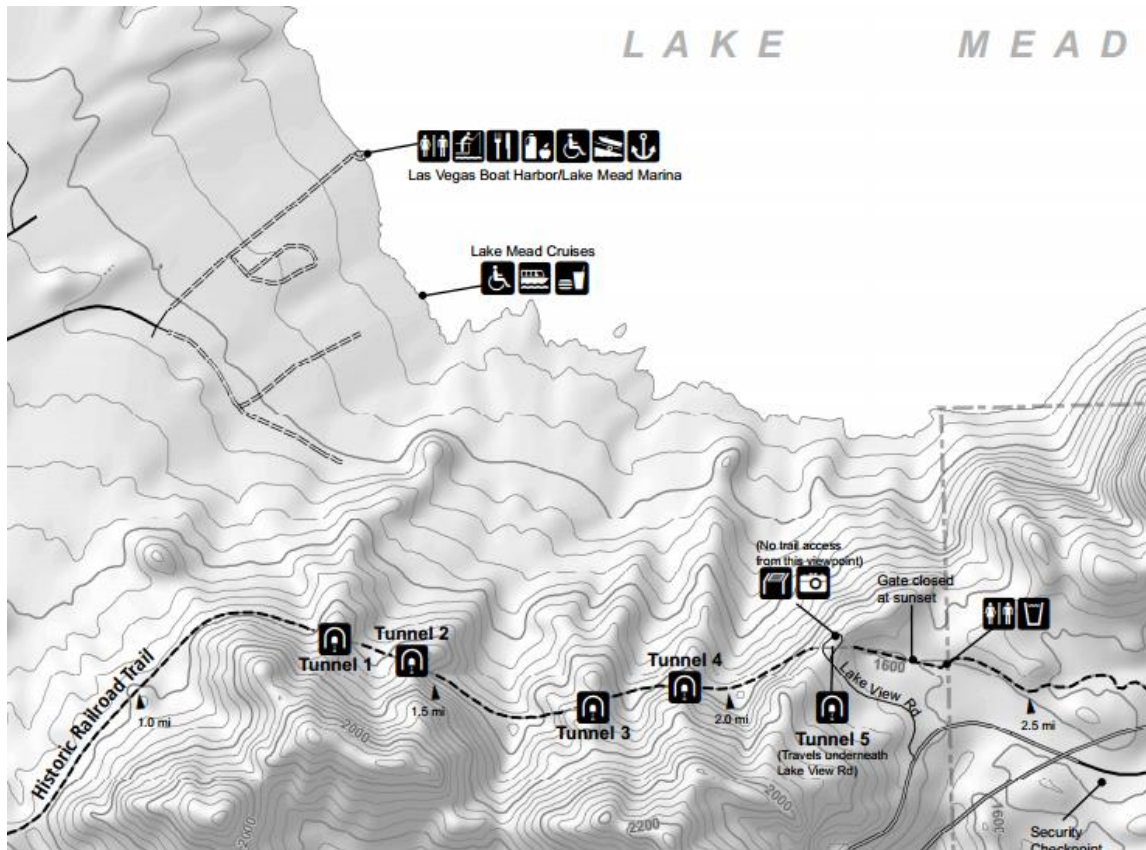
Figure 5.1. Map of the Historic Railroad Trail (National Park Service 2014)
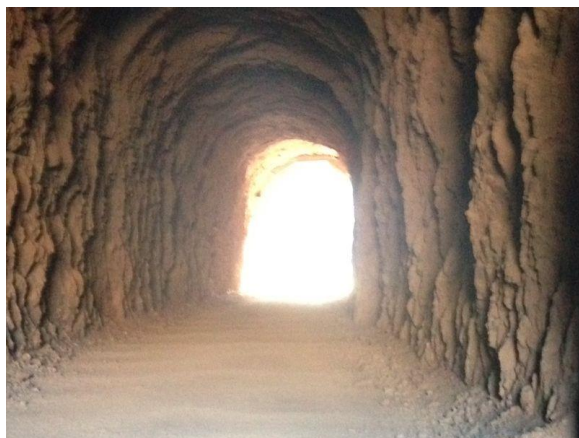
Figure 5.2. Photo of Tunnel 2 (left) and Tunnel 5 (right)

5.2 Testing

The tunnels were tested using infrared thermography and ultrasonic tomography. Infrared images were taken throughout all of the tunnels. The MIRA unit was only used in a few places due to the uneven surfaces of the rock tunnels. Therefore, the ultrasonic tomography was only used where a flat enough surface existed. The wave velocity was set to 2800 m/s for all UST scans and a frequency of 50 kHz.

5.3 Results

The surface roughness of the tunnels were challenging and created problems for both units. The thermal images were not conclusive due to the changes in surface area which results in temperature variations. A thermal image of each tunnel can be seen in Figure 5.3 through Figure 5.7. In Figure 5.5, the odd line in the image is from the thermal camera's lens accidentally looking at the sun. Also, Tunnel 3 has a smooth area that is visible in the thermal image. Tunnel 5 is curved which is why the opposite end cannot be seen in Figure 5.7. The line is the path the sun took across the lens. A few cracks could be seen in the thermal images, but they were also easily seen visually, an example can be seen in Figure 5.8.

41

62°F

46°F
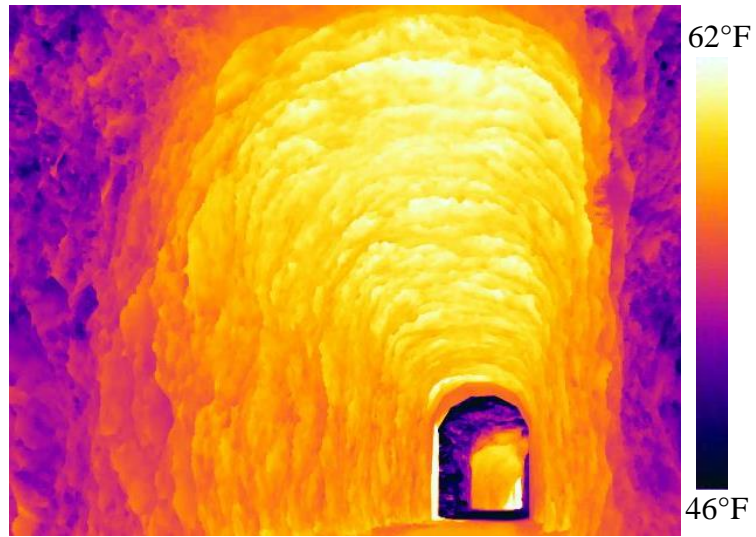
Figure 5.3. Thermal image of Tunnel 1

63°F

47°F
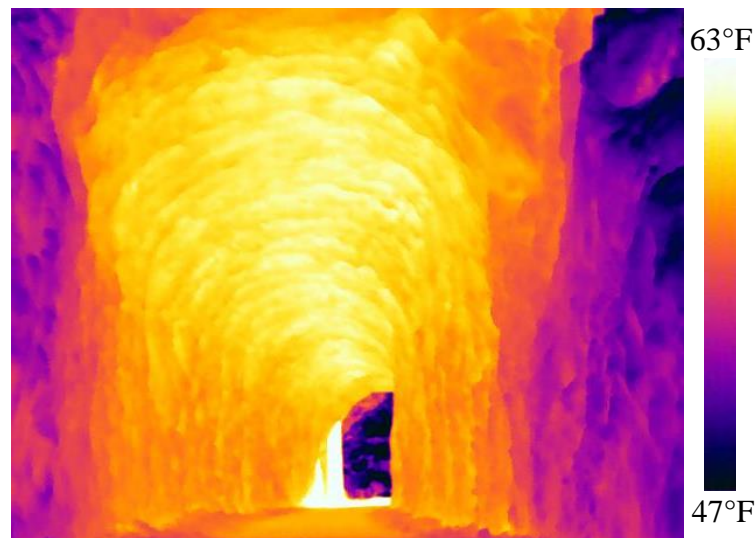
Figure 5.4. Thermal image of Tunnel 2
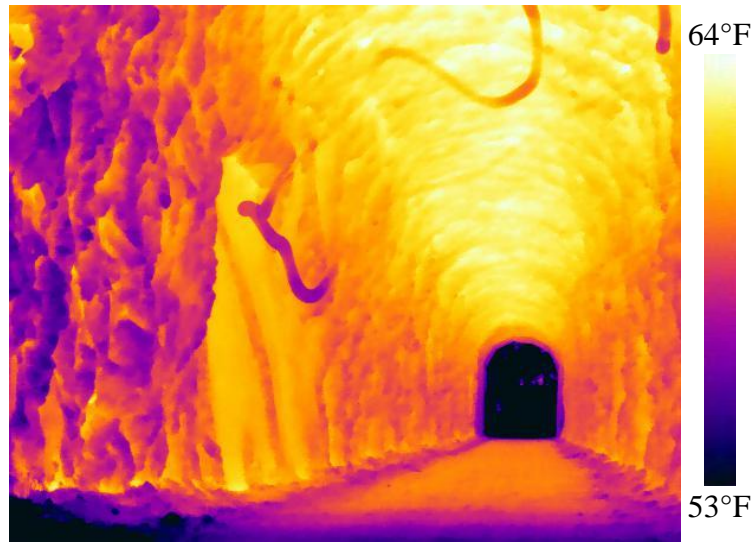
Figure 5.5. Thermal image of Tunnel 3

64°F
53°F
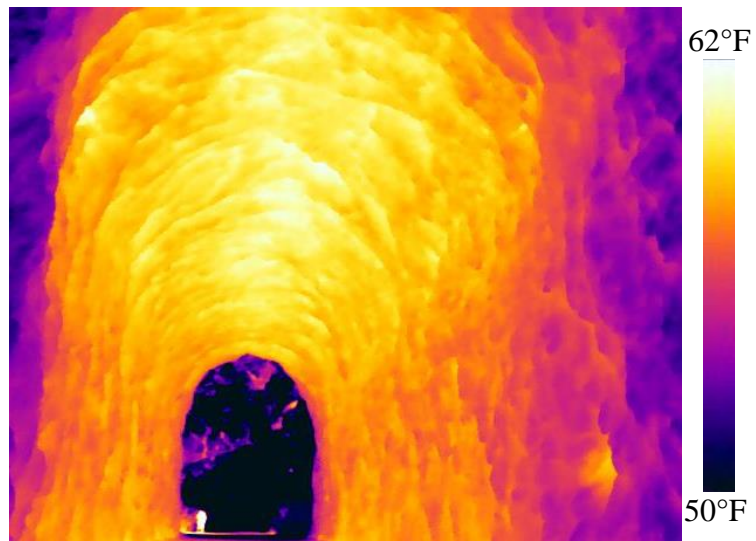
Figure 5.6. Thermal image of Tunnel 4

62°F
50°F

60°F

53°F
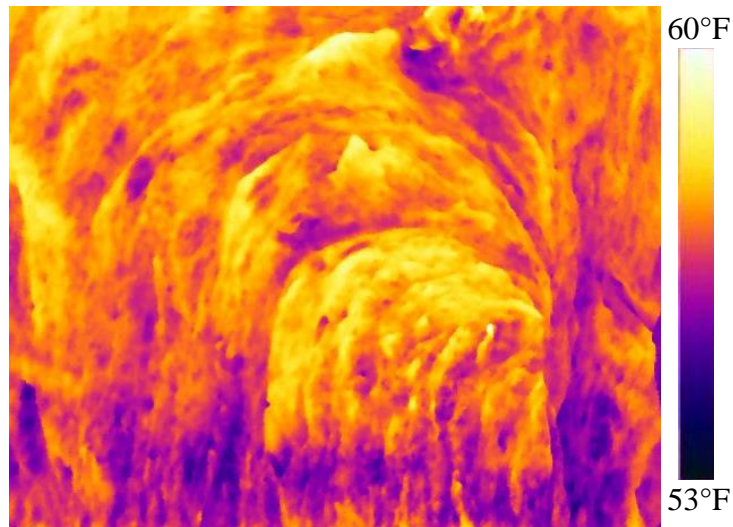
Figure 5.7. Thermal image of Tunnel 5

55°F

47°F
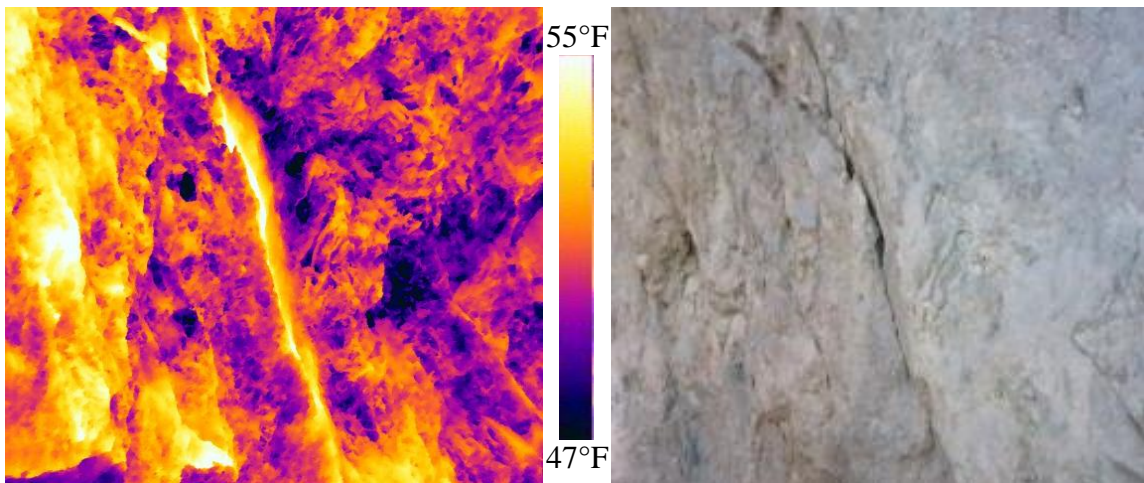
Figure 5.8. Images of crack: Thermal (left) and visual (right)

The UST was challenging to use on the rock. It was not able to be used on most of

the tunnels due to the uneven surfaces. Also, the areas that did get scanned the data was

inconclusive. This is most likely due to the hardness of the rock, and the fact that rock is

in layers. The MIRA device is specifically designed for concrete and rock is different in

its structure. Figures 5.9 and 5.10 show scans done on the smooth surface of Tunnel 3 and

44

is typical of all the other scans done. The figures show the full thickness on all the scan types so they are not at a certain depth or point on the axis not shown. The UST shows some red but it is within a large cloud of greens which makes it look erroneous. It is either a layer boundary or an area of non-homogeneity.
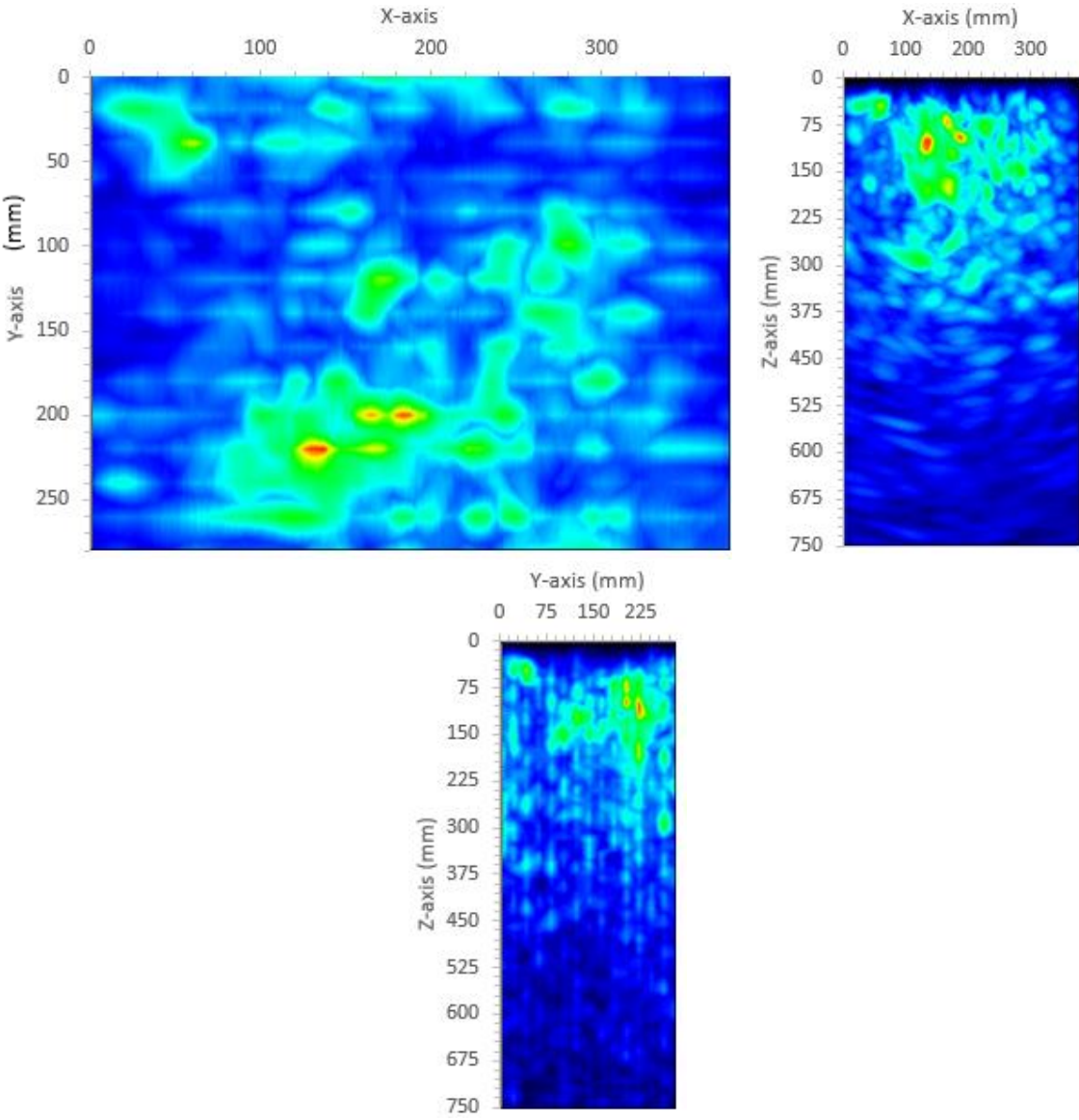
Figure 5.9. UST images: C-scan (top left), B-scan (top right), and D-scan (bottom)
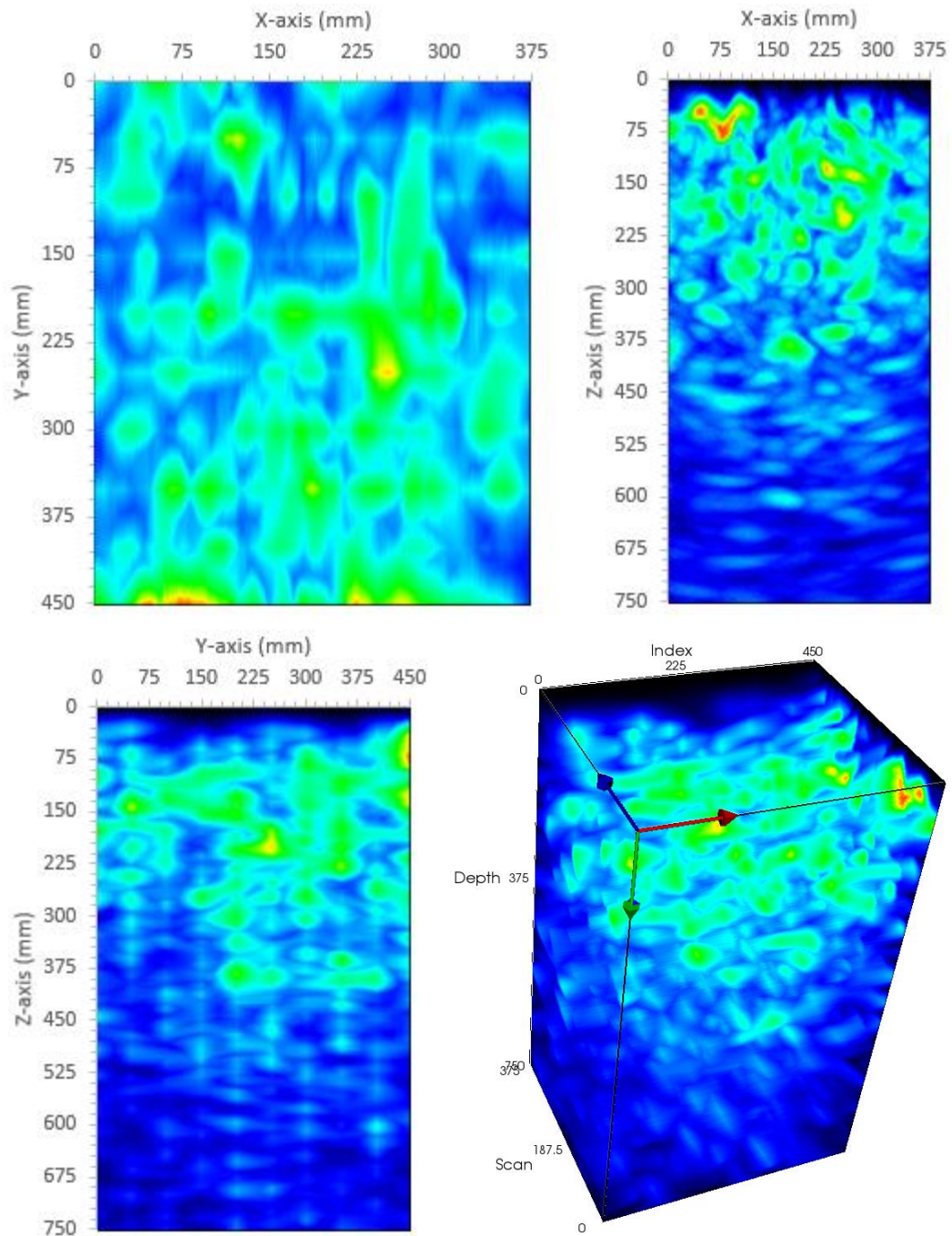
Figure 5.10. UST images: C-scan (top left), B-scan (top right), D-scan (bottom left), and 3D volume (bottom right)

46

CHAPTER VI

MOAB TUNNEL

Chapter VI provides information on the background of the Moab Tunnel as well as the testing procedures and results from the various scans. This tunnel was scanned using all three of the methods mentioned in Chapter III.

6.1 Background

The Moab Tunnel was constructed in 1962 and was built for access to the Potash Mine. It is owned by Union Pacific which still runs one train a week through the tunnel. The west and east portal can be seen in Figure 6.1. The drill and blast method was used in construction, and the tunnel is primarily rock with rock bolts and shotcrete, with some bare rock sections. Concrete sections are located at the beginning and the end of the tunnel and two are at various locations within the tunnel. The length of each section and its location can be seen in Table 6.1. The concrete sections of the tunnel were 23 feet high and 16 feet wide. The lining construction was unknown but was determined via testing.

Figure 6.1. Moab Tunnel: West portal (left) and east portal (right)

Table 6.1. Moab Tunnel segment lengths

Moab Tunnel			
Segment	Length (ft)	Curve Length (ft)	Lining
A	45	45	Concrete
B	263	263	Natural Rock
C	96	96	Concrete
D	2417	2417	Natural Rock
E	125	125	Concrete
F	3900	79	Natural Rock
G	215	0	Concrete
Total	7061	3025	

6.2 Testing

The testing of the Moab Tunnel focused on the four concrete sections. This was due to the fact that the focus of the research was on concrete linings and because of the results in Chapter V. The testing was performed Tuesday, July 15th through Thursday, July 17th of 2014. Since the only train runs on Sundays, this time frame provided all the track time that was necessary to complete the testing.

6.2.1 IRT Testing

Infrared thermography testing was done using the FLIR camera's video mode. The camera was hooked up to a laptop with FLIR Tools+ so that the video could be saved directly to the computer to avoid memory issues. Prior to testing a temperature study was done for the three days of testing for the previous three years. The results of the study can be seen in Figure 6.2. Based on the figure the best time for testing would be in the morning

48

between 7:00 AM and 12:00 PM or in the evening between 6:00 PM and 8:00 PM due to the steep temperature change. The actual testing occurred on July 15, 2014, in the morning between 9:00 AM and 12:00 PM. Four thermal videos were taken at various speeds and times which can be seen in Table 6.3. The set-up for the infrared camera can be seen in Figure 6.2. The tunnel temperature was measured during testing on July 16th and 17th at two locations. This was done to determine temperature change throughout the day and to compare to the exterior temperature.
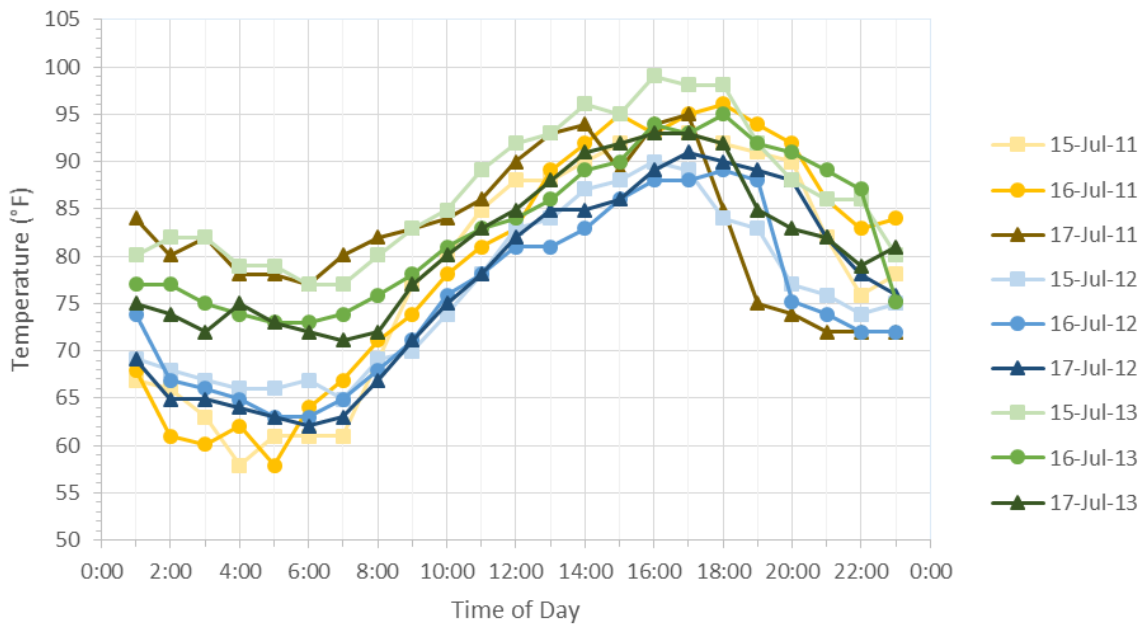
Figure 6.2. Temperature study prior to testing (Weather Underground 2014)

Table 6.2 IRT video details

Run	Start Time	Speed (mph)	Direction (Segment)
1	9:17 AM	2	A to G
2	10:32 AM	4	A to G
3	11:03 AM	8	A to G
4	11:46 AM	5	G to A

49

Figure 6.3. Thermal camera set-up on high rail truck

6.2.2 UST and GPR Testing

Ultrasonic tomography and ground penetrating radar were used at three locations in the tunnel. Two of the locations were determined using the infrared data, and the third was chosen because rebar was visible at the end of the concrete lining section. The third section was used to determine how well the UST and GPR could find the rebar within the lining. Testing with GPR in the tunnel was done by creating a custom grid in the computer software and then loading the scans to make a 3D scan instead of using the GSSI grid used in the slab testing. Therefore, the GPR grid was the same as the drawn grid. The UST scans were done similar to the slabs with a step size of 50 mm in the vertical direction and 150 mm in the horizontal. The first location was in Segment C and was close to the top of the tunnel. A 1.75 m by 1.20 m with a spacing of 50 mm grid was used and can be seen in Figure 6.4. The MIRA device was only used oriented in the horizontal direction. The

second grid was located in Segment E and was on the left side of the tunnel traveling from Segment A to Segment G. This grid was 3 m by 2.40 m with 50 mm spacing, shown in Figure 6.5. For this location, UST scanning was done with the unit oriented both horizontally and vertically. The final location was in Segment G on the left, and a grid of 1.20 m by 1.20 m was used which is shown in Figure 6.6. Since the visible rebar was longitudinal, the MIRA device was used oriented vertically, so that it would have the best chance of finding the rebar.
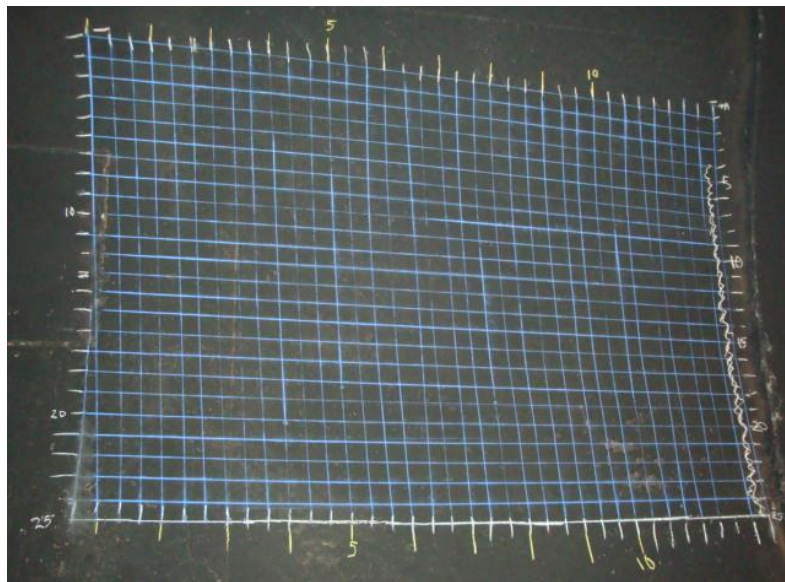
Figure 6.4. Grid located at Segment C

51
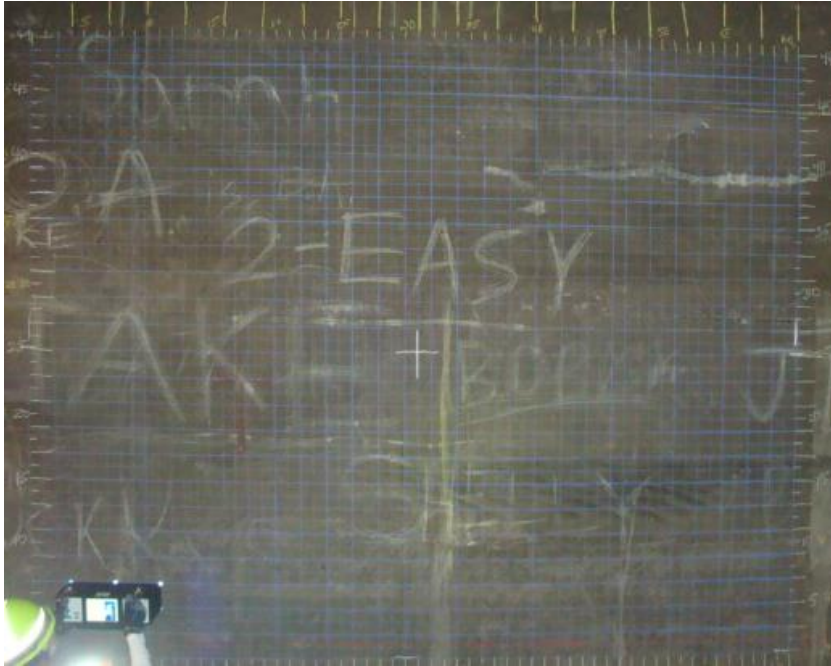
Figure 6.5. Grid located at Segment E, and UST oriented horizontally
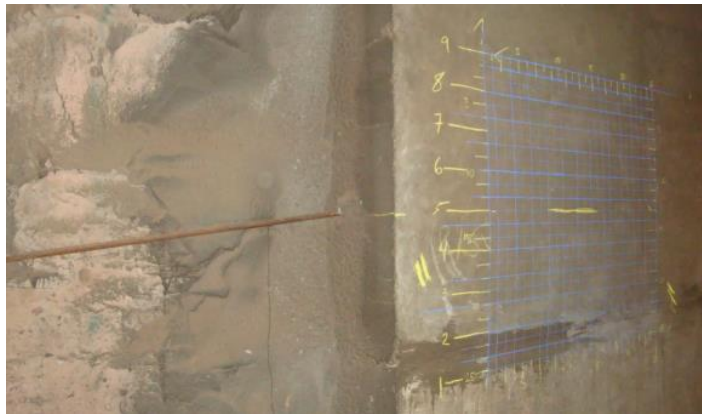
Figure 6.6. Grid located at Segment G with the visible rebar

6.3 Results

All of the methods provided significant results on the tunnels structure and/or issues. The tunnel seems to be constructed with a steel ribbed system at the concrete

sections. This type of lining was mentioned in Chapter II; however, there did not seem to be any blocking between the ribs. The steel ribs were used as preliminary support then reinforced concrete was poured over and between the ribs as the final support system. The rest of the results in this section are organized by the grid used and then a general results section for areas that did not correspond to a grid.

6.3.1 Grid 1 Results

Grid 1's location was determined by the thermal videos taken of the tunnel. All of the videos detected an area of temperature change over a short distance in Segment C. Figure 6.7 shows the area from the run 4 video. The segment has a lot of temperature variations; however, the chosen area is unique because the change occurred over a shorter distance than the other infrared deviations and it was not across a construction joint. The grid was placed over the area with the middle of the grid placed at the location of the
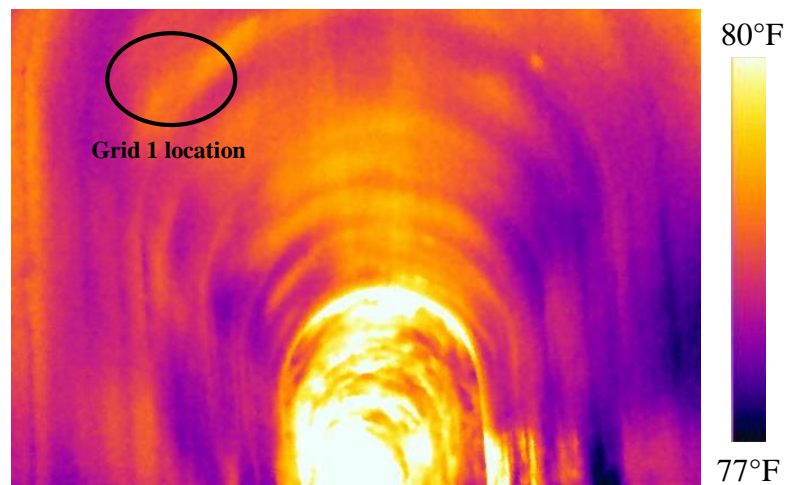
Figure 6.7. Run 4 image of Segment C

largest temperature change. This provided adequate area over both the cool and warm sections.

The GPR device detected the reinforcement beam and a problem area within this grid. Figure 6.8 shows two C-scans and a B-scan that provide the beam and problem area locations within the grid. The issue area was located at depth of about 64 mm according to the GPR which would mean that the infrared camera would be able to detect it. The detection of the beam allowed for a better understanding of the construction method used to build the tunnel and the lining. There was not any rebar detected in this location; however, later testing showed that the grid was most likely in between longitudinal bars. The GPR could not find the back wall which is most likely due to the fact that the rock and concrete materials have similar dielectrics, and the gap between the two was too small to reflect the electromagnetic waves.

The UST device detected the problem area better than the GPR did; although, the UST did not detect the steel beam as well. The issue area was larger and detected deeper within the concrete with the MIRA device. The area was detected between 50 mm and 150 mm with the center being near 90 mm. Figure 6.9 provides scans that show the problem area along with the reinforcing beam. Since shear waves are not able to be transmitted across any type of air gap, the ultrasonic method was able to detect the back wall over a small portion of the grid which the GPR was not able to accomplish.

Based on the infrared, GPR, and UST data the problem area is most likely a thin, shallow void. The GPR detected both sides of the void with a gap in between which can

be seen in the B-scan of Figure 6.8. The UST shows a cloudy area with some high reflections similar to what the voids detected during the slab testing.
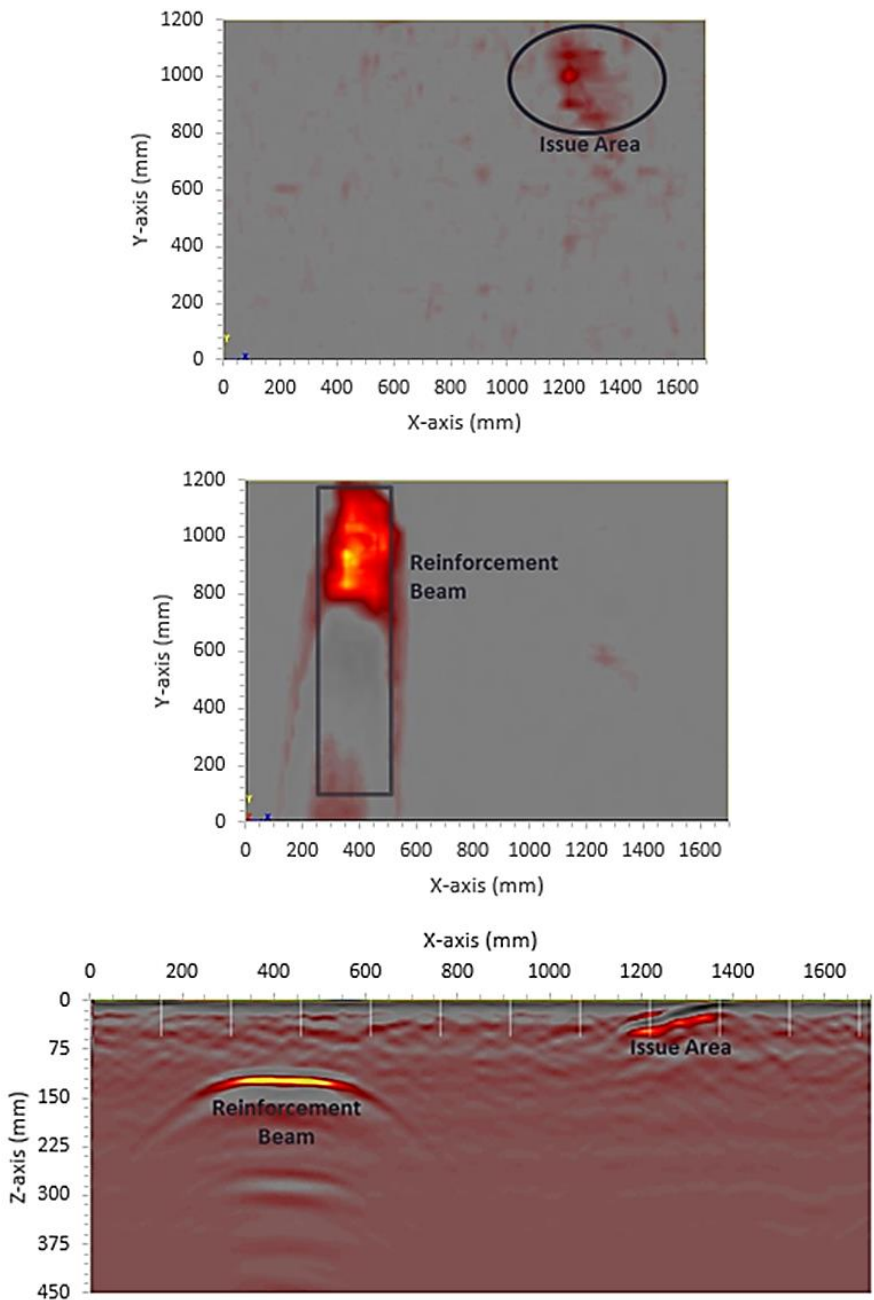
Figure 6.8. GPR scans of Grid 1: C-scan at 64.5 mm (top), C-scan at 135.5 mm (middle), and B-scan at 1000 mm (bottom)
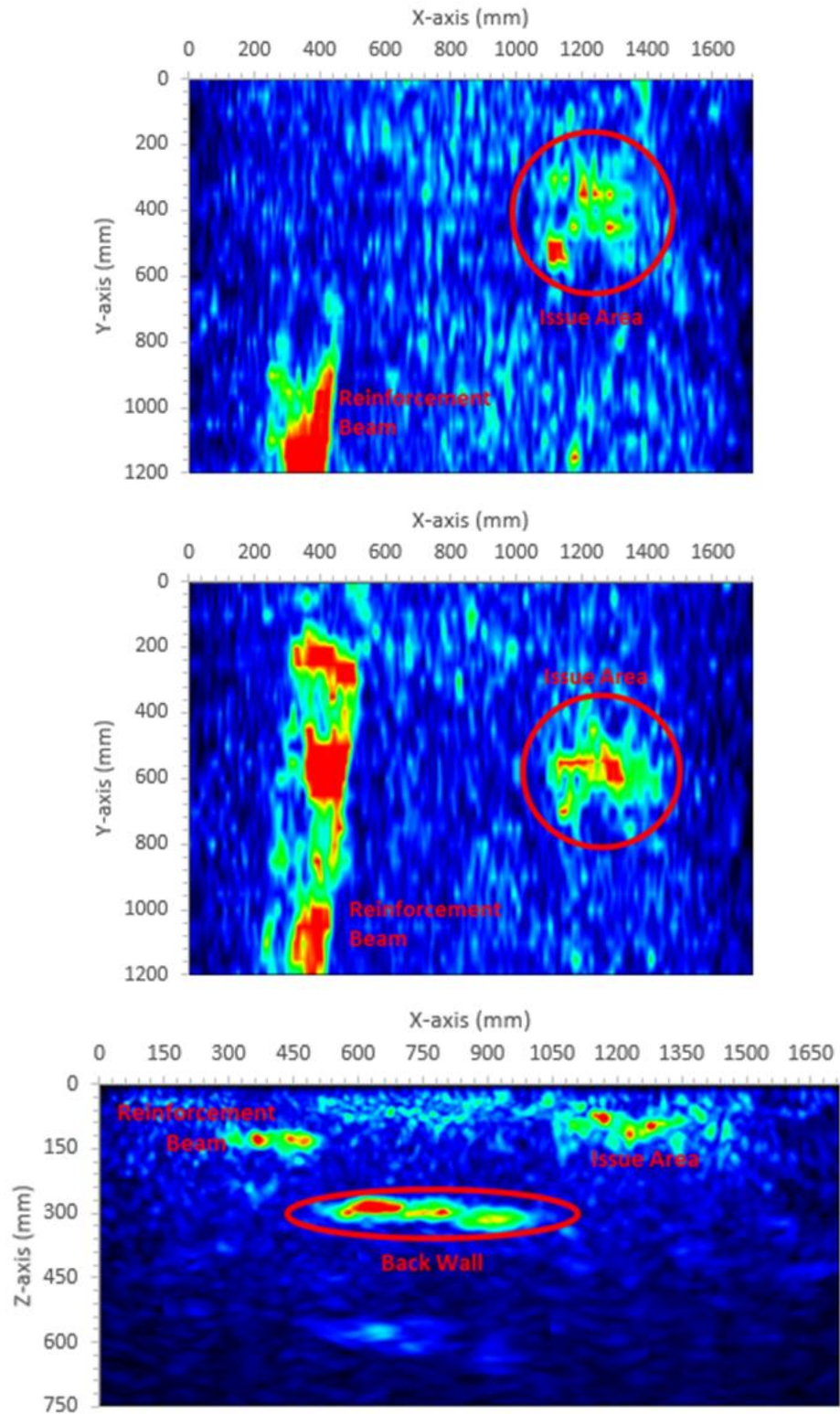
Figure 6.9. UST scans of Grid 1: C-scan at 90.5 mm (top), C-scan at 125 mm (middle), and B-scan at 450 mm (bottom)

Grid 2 was placed on the side wall of Segment E based on the thermal videos. The area was chosen based on the temperature change and that the change did not occur across a construction joint. There are other similar areas in this segment but the one chosen looked the most drastic based on all the videos. Figure 6.10 shows the chosen area from the thermal video taken during run 2.
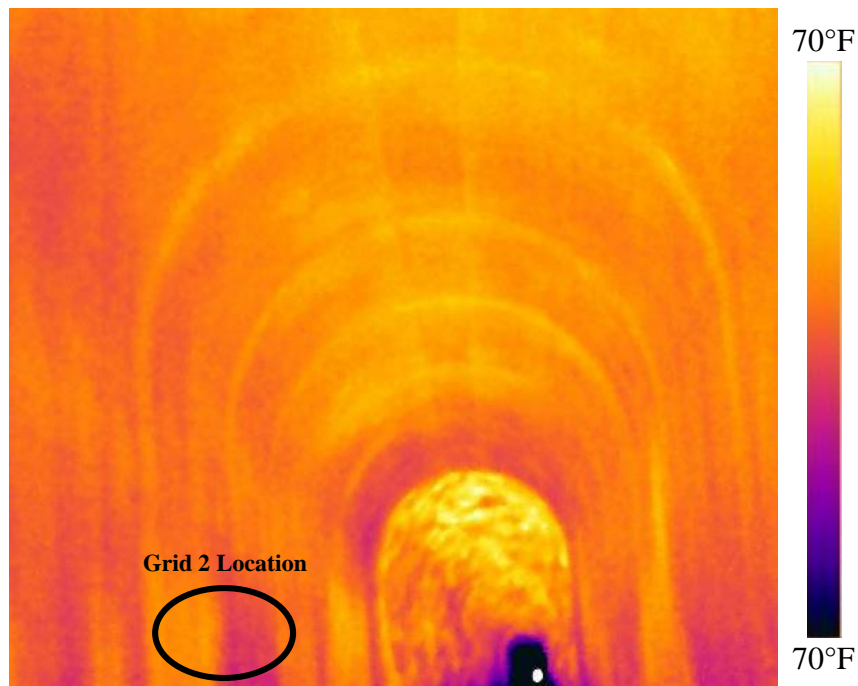
Figure 6.10. Run 2 image of Segment E

The GPR of this grid provided a lot of information on the construction of the tunnel lining. Since the grid was so large, many different features were found such as rebar in both directions and the spacing of the reinforcement beams. Figures 6.11 and 6.12 show

scans from the GPR with the various items identified. The spacing of the reinforcing beams was 1.5 m with two vertical rebar located in between. One area that is labeled "Unknown" is believed to be rebar that was not placed properly because it was not located at a consistent depth. It is visible in the C-scan at 61.5 mm, and in the B-scan it is shown at a depth of 160 mm. There was another reinforcing beam just outside of the grid that was detected which would mean that the "Unknown" rebar would be the second one between the two beams. The horizontal rebar can be seen in the deeper C-scan and the D-scan; they were spaced at 1.47 m. The GPR was also able to find the back wall of the lining; therefore, the lining must be partially debonded in this area.

The UST was able to detect all the rebar and beams including the "Unknown" bar; however, this was only possible because the grid was scanned with the MIRA device oriented in both directions. Figure 6.13 shows the data from the horizontal orientation, and Figure 6.14 is the vertical orientation data. When it was oriented horizontally it was only able to detect the vertical rebar. The horizontal rebar was only detected with the device oriented vertically, similarly the vertical rebar disappeared with this orientation. The reinforcing beams were detected in both scanning directions. Also, the back wall was detected in both sets of scans in a similar location as the GPR data.

No anomalies were discovered that would have caused the temperature variation detected with the thermal camera. The detection of the back wall seemed to correspond to the location of the temperature change, yet that difference would be too deep for the thermal camera to detect. The temperature difference was either due to environmental factors or undetected properties with the lining.

58
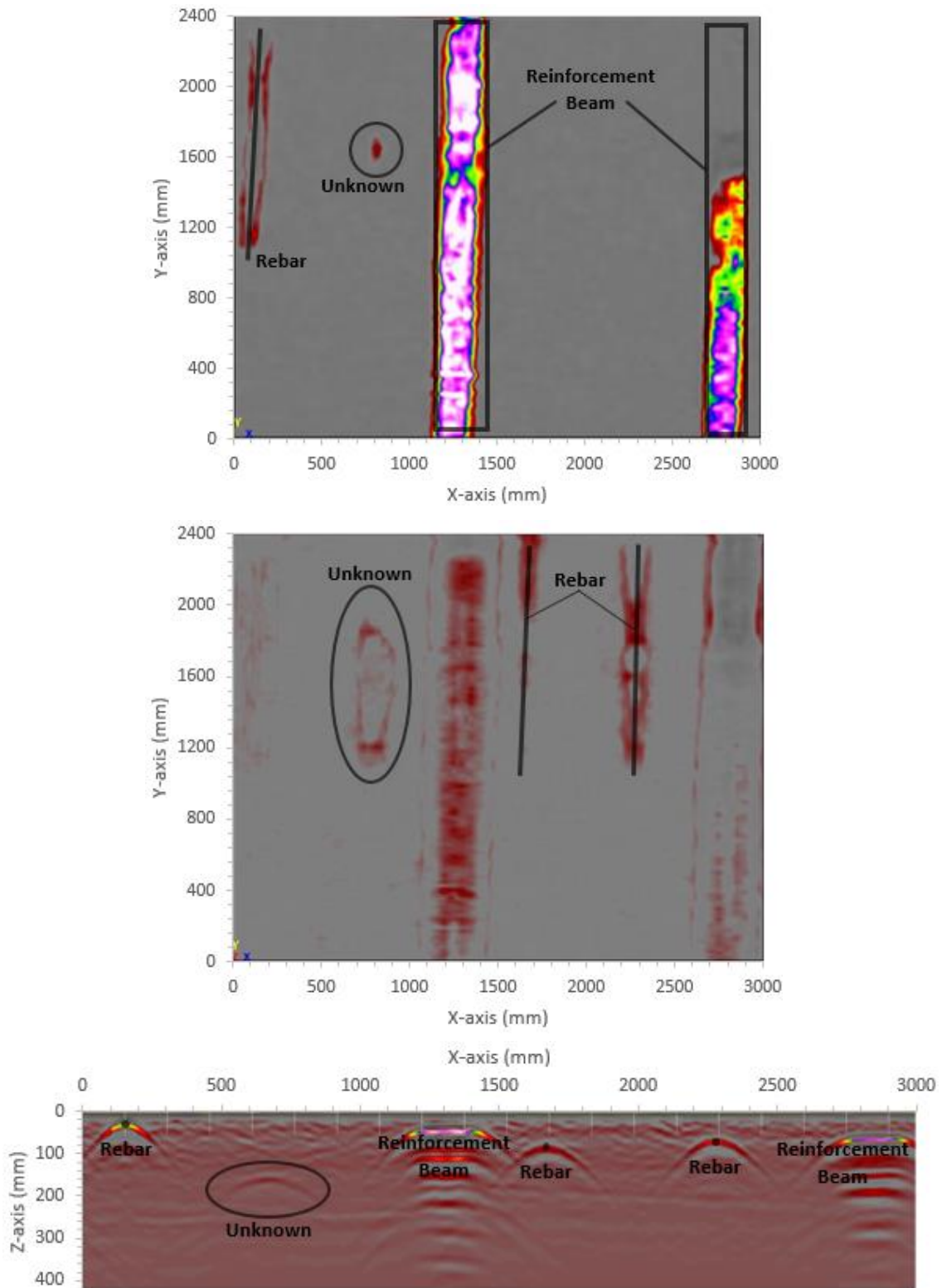
Figure 6.11. GPR data from Grid 2: C-scan at 61.5 mm (top), C-scan at 103 mm (middle), and B-scan at 2200 mm (bottom)
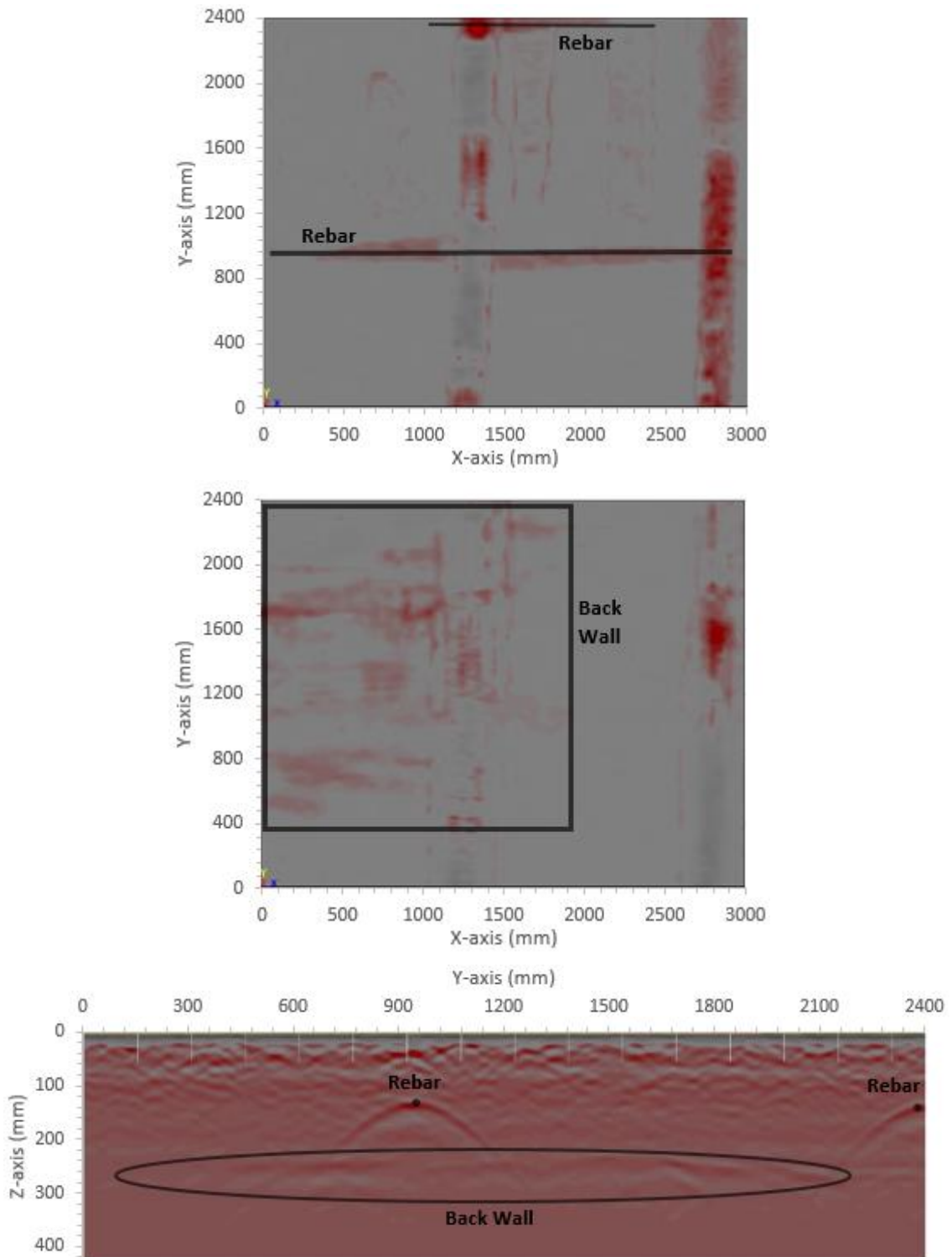
Figure 6.12. More GPR data from Grid 2: C-scan at 145 mm (top), C-scan at 274 mm (middle), and D-scan at 350 mm (bottom)
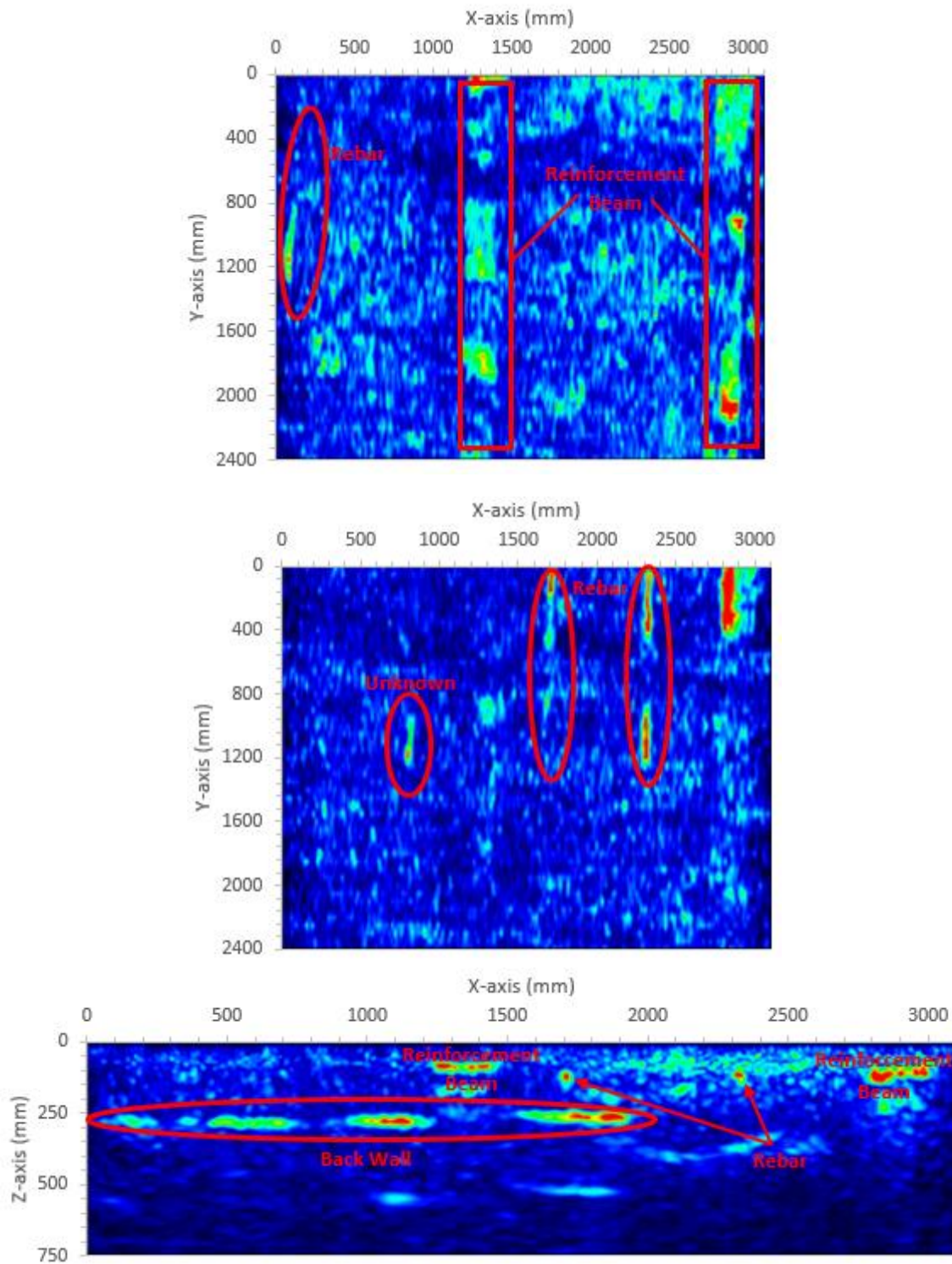
Figure 6.13. UST oriented horizontally data from Grid 2: C-scan at 80 mm (top), C-scan at 124 mm (middle), and B-scan at 850 mm (bottom)
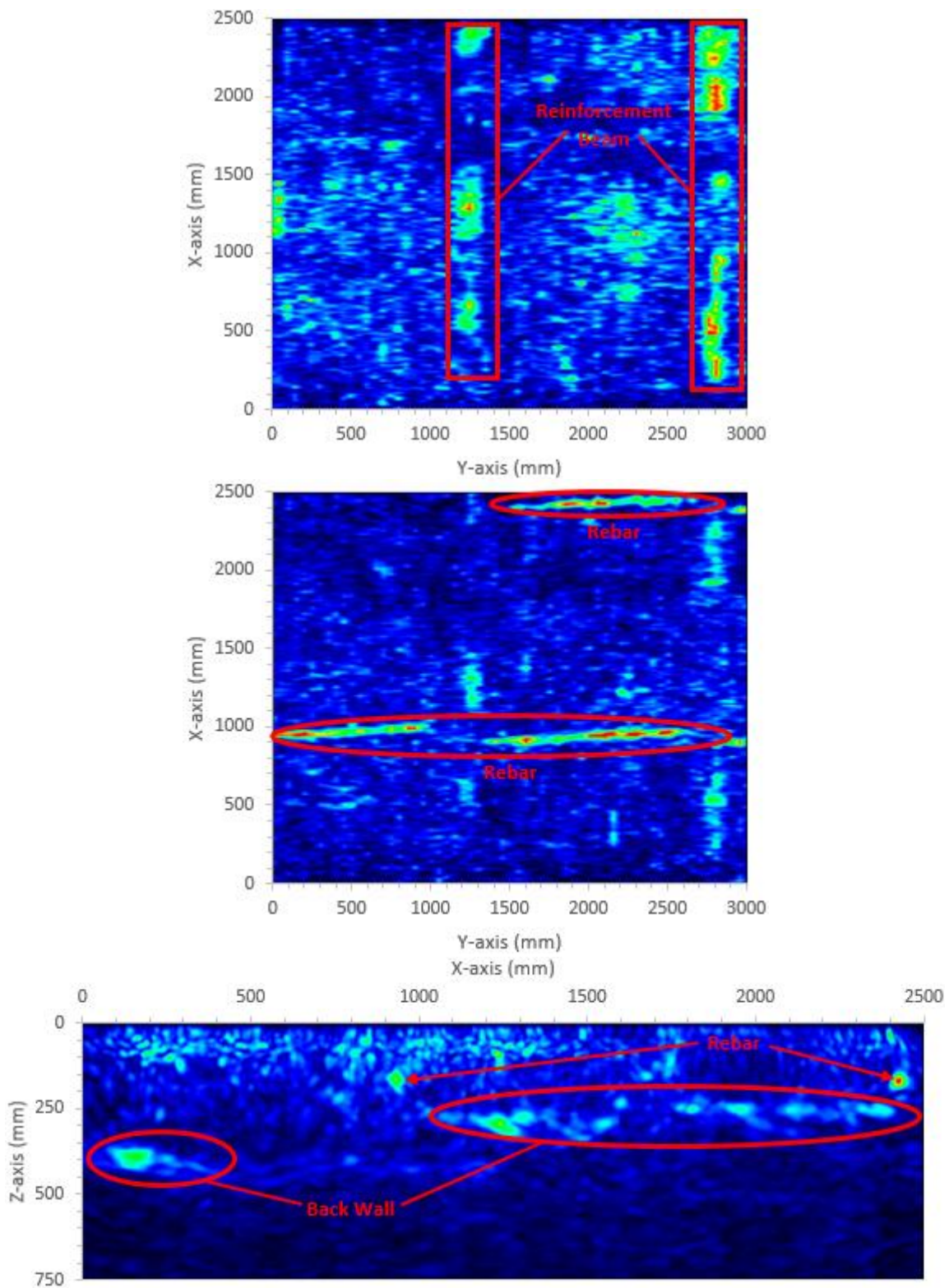
Figure 6.14. UST oriented vertically data from Grid 2: C-scan at 90.5 mm (top), C-scan at 172 mm (middle), and B-scan at 1900 mm (bottom)

62

6.3.3 Grid 3 Results

Grid 3 was used to determine the capabilities of the devices to detect rebar and how accurate their dimensions are. Since the rebar was exposed, the cover was known and could be compared to the detected depth. The measured cover of the rebar was 290 mm. Figure 6.15 shows that the exposed section of the rebar was detected with the thermal camera; however, this grid was primarily for the UST and GPR methods.
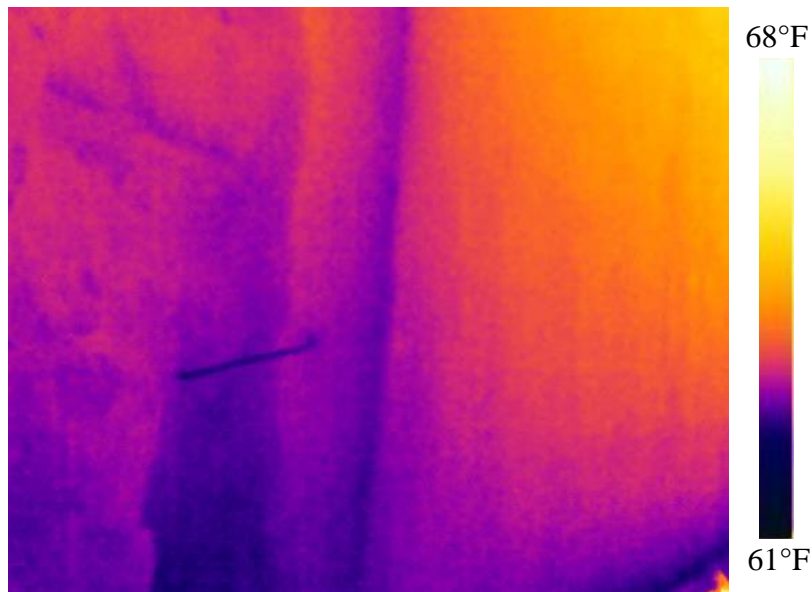
Figure 6.15. Infrared image of the exposed rebar at Grid 3

GPR found the rebar at a depth of 240 mm within the lining. This distance was 50 mm shallower than the measured cover which is an error of 17%. The UST detected the bar with more accuracy at a depth of 260 mm resulting in an error of 12.5 %. The accuracy of both devices can be improved by using more precise values for the dielectric constant

in GPR and the wave velocity in UST. Figure 6.16 and 6.17 show the GPR and UST data

from this grid. The reflections from the electromagnetic and shear waves were more faint

due to the depth of the rebar which could effect the accuracy of the devices as well.
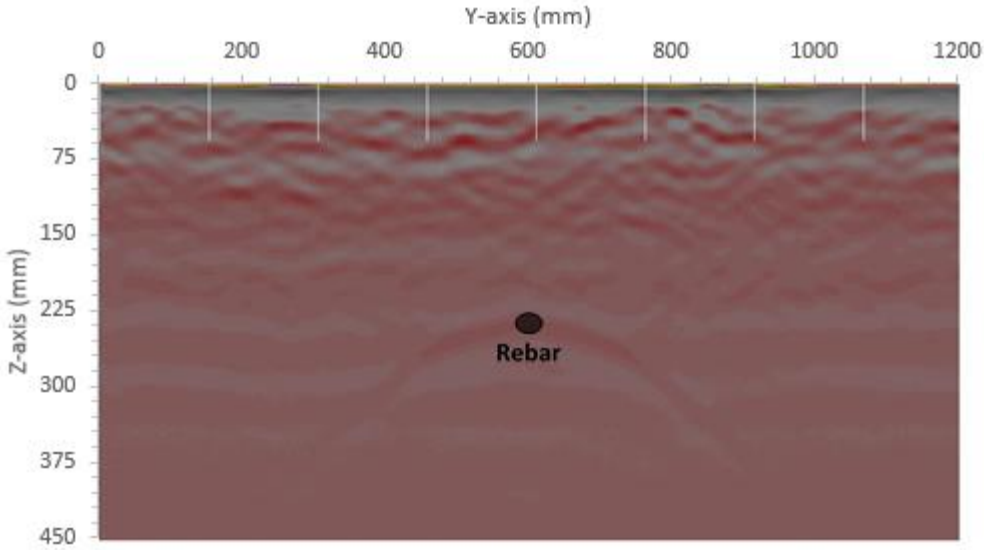
Figure 6.16. GPR of rebar at Grid 3
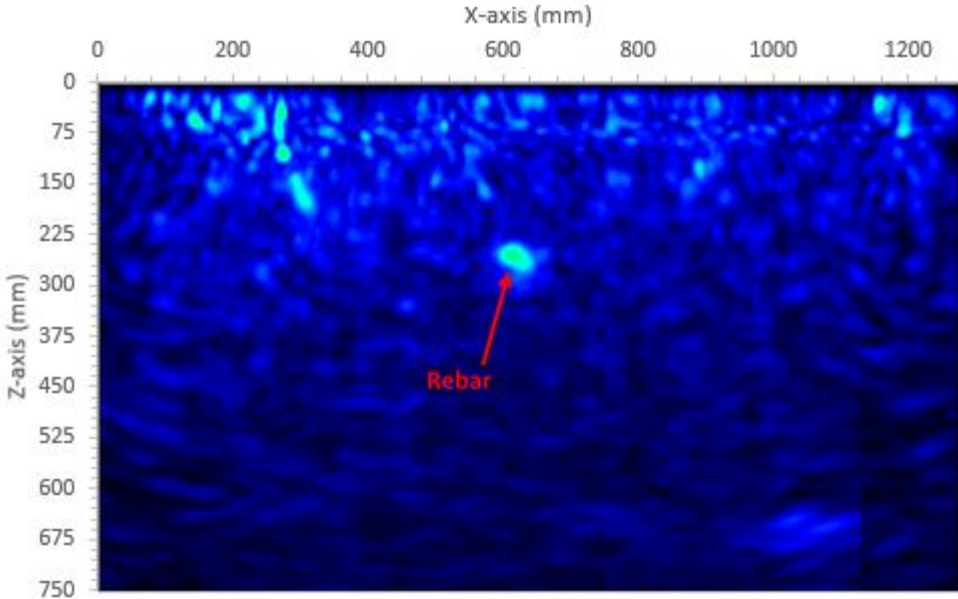
Figure 6.17. UST of rebar at Grid 3

64

6.3.4 Other Results

A major result from the infrared testing on the Moab Tunnel is that runs need to go in both directions through the tunnel. It provides two perspectives on all the surfaces and makes the biggest difference at the ends of tunnels. When the end of the tunnel is reached the thermal video is altered due to the heat from the sun shining through the portal. Figure 6.18 compares the thermal video from each direction on the east portal. The details of the portal can be seen better in the image from the video starting at the east portal which was Segment G.
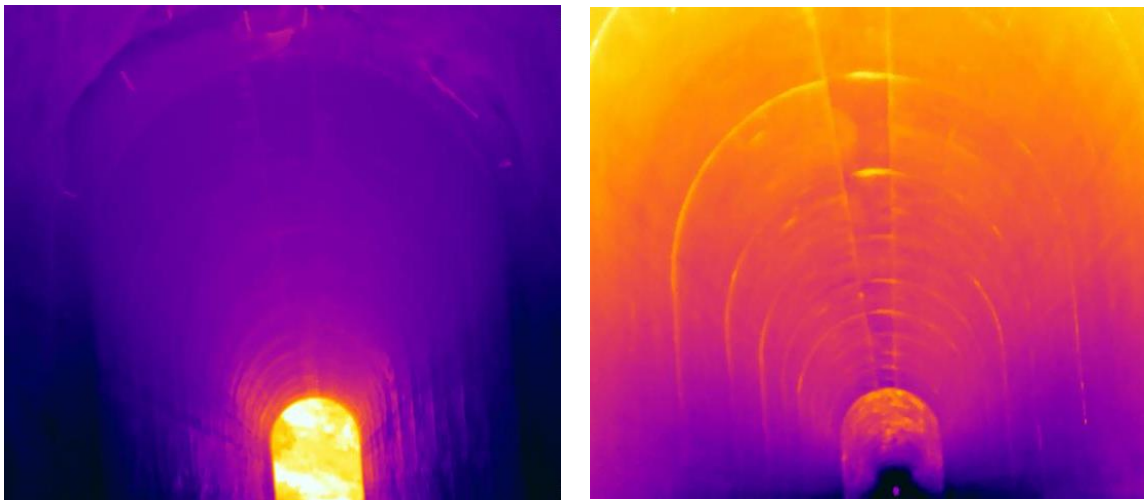
Figure 6.18. Thermal images of the east portal (Segment G): Image from Run 2 (left) and image from Run 4 (right)

A failure of the shotcrete lining within the rock Segment F. It was first noticed visually and then the thermal video was checked to see if it was noticeable. Figure 6.19

and 6.20 show the image from the thermal video and a thermal image and photo. A large

chunk of rock had fallen off at the location along with the shotcrete.

67°

62°

Spall Area
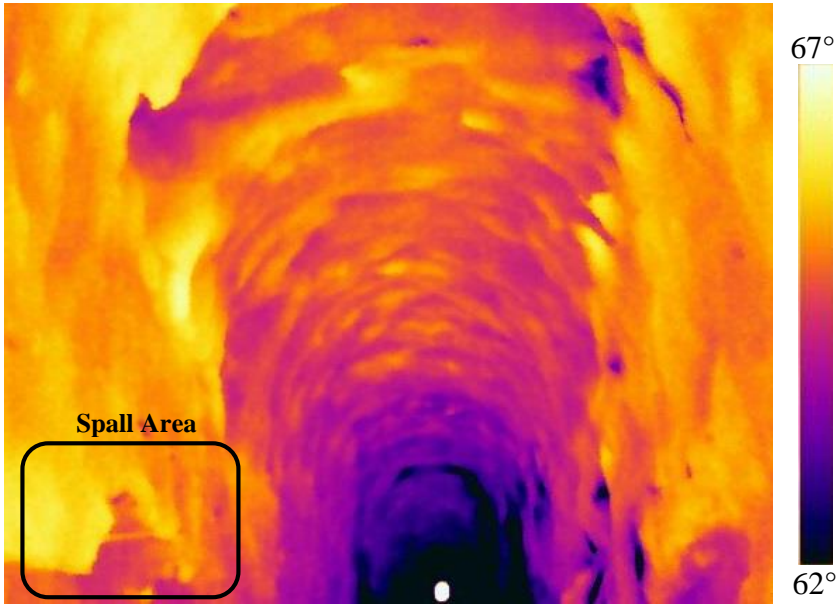
Figure 6.19. Thermal image from Run 4 of the spall in Segment F

68°

62°
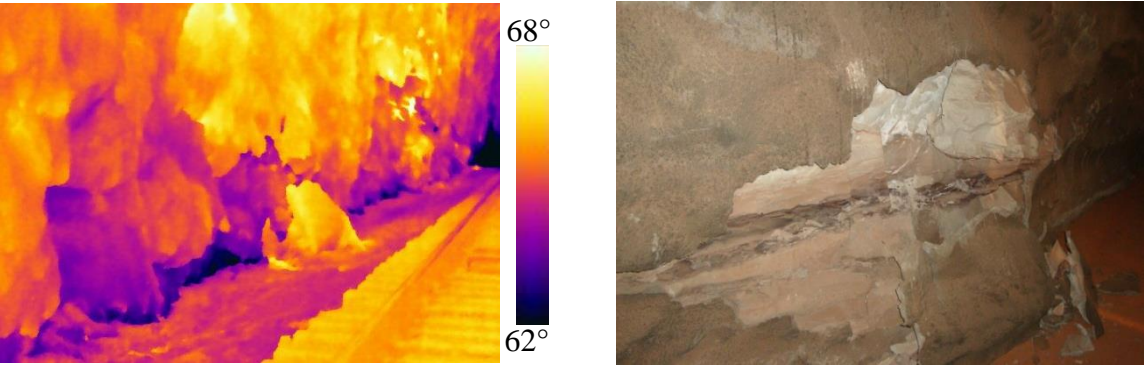
Figure 6.20. Thermal image and photo of the spall in Segment F

The thermal videos also worked very well for detecting water infiltration in the rock sections. Figure 6.21 is a thermal image showing a large area of water with in the rock Segment F. Water found within a concrete section would be an indication of other problems. The thermal camera detected the rock bolts as well. They could be seen in the thermal image in many locations when they were not visible. Figure 6.22 shows rock bolts that were located on the ceiling of the tunnel which would be difficult to see visually. The metal bolts heat and cool differently than the concrete and create more surface area for heat flux.
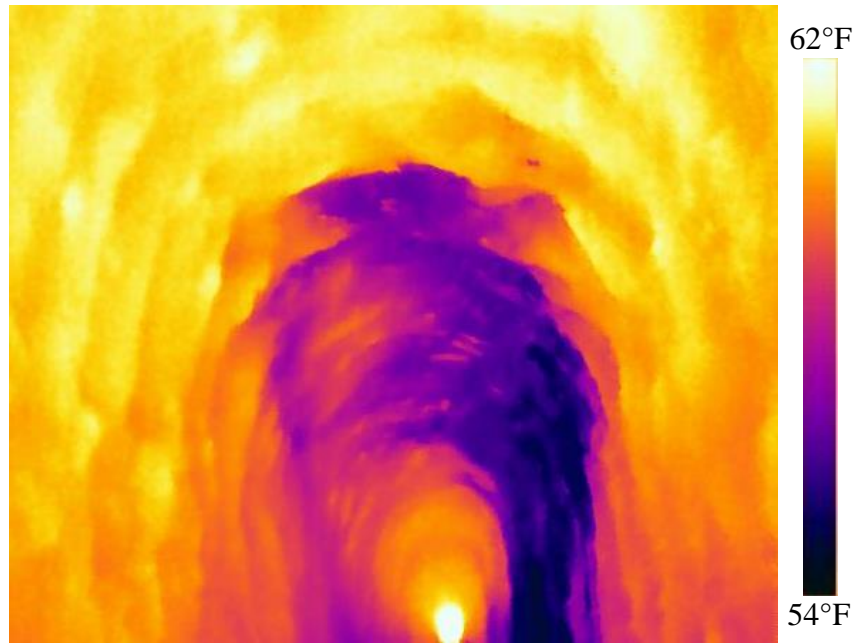
Figure 6.21. Thermal image of water infiltration

70°F

61°F
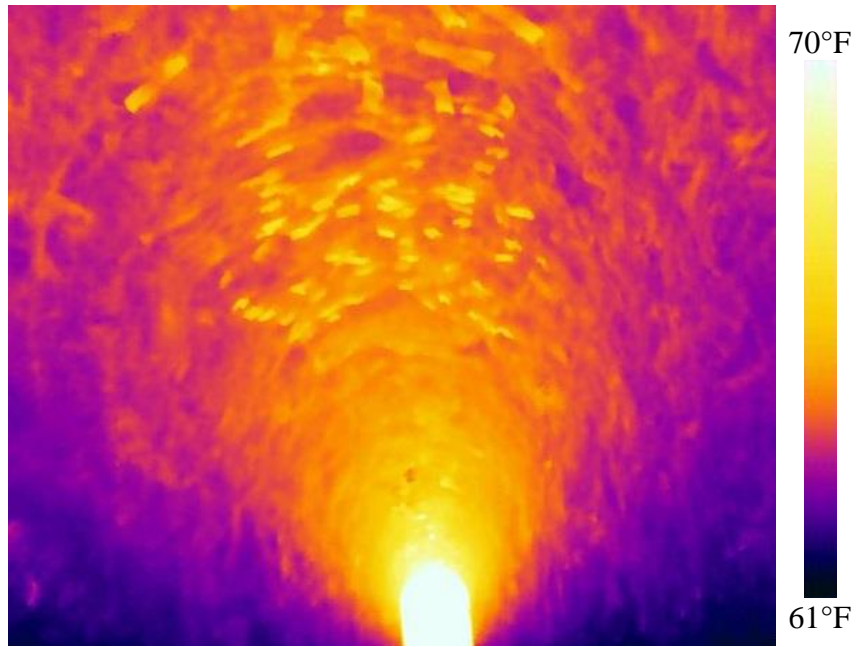
Figure 6.22. Thermal image of rock bolts on the ceiling of the tunnel

The temperature data can be seen in Figure 6.23. The exterior temperature data was placed on the graph to compare the change in temperature in the tunnel with the change in exterior temperature (Weather Underground 2014). The sensor located at the beginning of Segment C on July 17 registered temperature changes similarly to the exterior. However, the one located at the end of Segment E did not detect much of a temperature change. This was most likely due to it being located near the middle of the tunnel, and the temperature does not vary as much there.
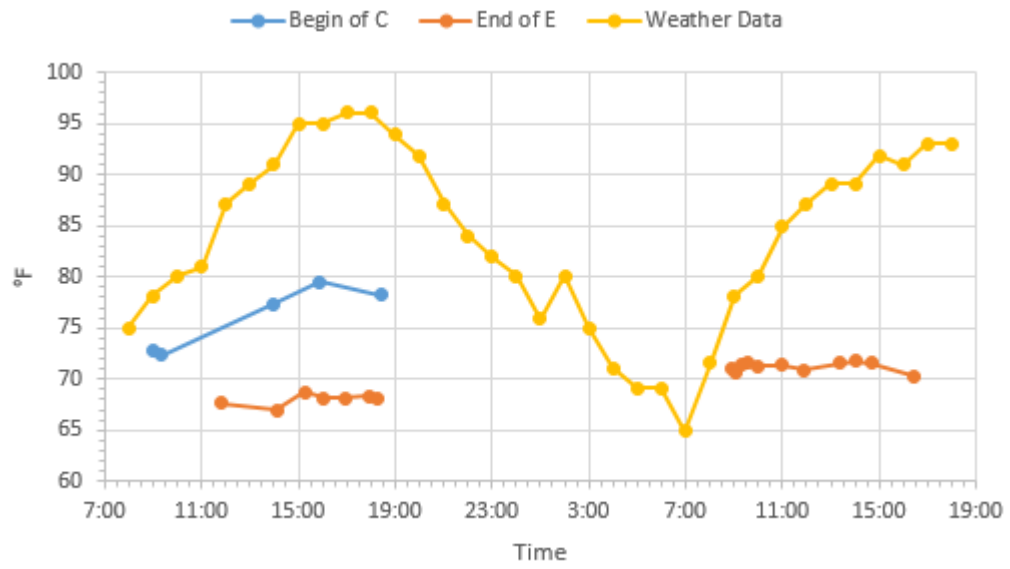
Figure 6.23. Temperature data from inside and outside the tunnel on July 16 and 17, 2014 (Weather Underground 2014)

CHAPTER VII

CONCLUSIONS AND RECOMMENDATIONS

This chapter will discuss the conclusions of the research and recommendations for future research. It will also provide some information on how to improve future data acquisition.

7.1 Conclusions

The infrared thermography, ground penetrating radar, and ultrasonic tomography were used to detect various types of anomalies in concrete and shotcrete. All of the methods worked appropriately and accomplished the overall task. The IRT method allowed for quick scanning of the Moab Tunnel and provided information for two detailed scanning locations. One of the locations had a defect that was detected with both the GPR and UST devices. Thermal imaging also proved to be useful in determining areas of water infiltration within tunnels. Scanning a tunnel needs to be done travelling in both directions to provide the best results, especially at tunnel portals. The slab testing exposed many of the limitations of IRT. The device is limited to detecting delaminations 50 mm deep and voids 100 mm deep. Temperature change is the lynch pin that allows for infrared detection to be useful. If the temperature is not changing, the device is not useful which was demonstrated by the slab testing done at various times through the day.

GPR provided detailed information about the steel within the concrete. It was able to detect all of the rebar in the slab testing and the expected rebar in the Moab Tunnel. It was also able to find most of the voids and delaminations in the slabs especially when the UST data was available to compare. GPR does not detect delaminations very well if the

gap is not adequate to reflect the electromagnetic waves. The depths to defects and thicknesses it detected were not very accurate; however, these can be improved by determining a more accurate dielectric constant prior to testing. The GSSI StructureScan Mini HR was easy to use and scanned faster than the MIRA device.

UST was the best at finding issues within the tunnel lining and the slabs. The majority of the defects in the slabs were detected by the MIRA device. The depths provided by it were more accurate than the GPR and could be improved more by determining the wave velocity better. This could be done by averaging over a larger sample of wave speeds before testing. The biggest drawback of the UST method is that it cannot pass through air voids and water filled voids. If there are any layered problems, it will only be able to detect the one on top. It is also a very slow process to scan a large area with the device. When the device is oriented appropriately it can detect rebar and other long slender objects. Therefore, scanning needs to be done twice so that both orientations can be used.

The three devices tested provided important information about the Moab Tunnel lining that could not be determined using current investigation standards. Implementing these methods would take improvement primarily due to the required track time to properly scan the tunnel. However, the research shows that these methods would improve tunnel inspections and would allow for more issues to be found earlier providing safer rail tunnels and cheaper maintenance.

7.2 Future Research

Future research should look into testing for other types of tunnel linings:

- Tunnels with no lining or rock.

- Linings that are not smooth.

- Metal linings constructed out of steel.

Testing should be conducted on the adequacy of air-coupled GPR for rail tunnel linings. The device is similar to the GPR used in this study, but it does not require the antenna to be in contact with the testing surface. It can be used at greater speeds than the ground-coupled GPR and could be used in conjunction with infrared thermography as another fast method. Temperature variations within tunnels relative to exterior temperatures should be studied. If there is a correlation between the changes in exterior ambient temperature and the interior tunnel temperature, testing with the infrared camera could be improved.

REFERENCES

Hoegh, K., Khazanovich, L., and Yu, H. T. (2011). "Ultrasonic Tomography for Evaluation of Concrete Pavements." *Transportation Research Record,* 2232(2232), 85-94.

Kamoi, A., Okamoto, Y., and Vavilov, V. (2004). "Study on detection limit of buried defects in concrete structures by using infrared thermography." *Key Eng Mat,* 270-273(II), 1549-1555.

Ko, B., Son, Y., Shin, D., and Han, C. (2003). "Development of an Inspection System for Cracks on the Lining of Concrete Tunnels." *Proceedings of the 20th ISARC,* Eindhoven, Holland, 457-463.

Li, C., Li, M., Zhao, Y., Liu, H., Wan, Z., Xu, J., Xu, X., Chen, Y., and Wang, B. (2011). "Layer recognition and thickness evaluation of tunnel lining based on ground penetrating radar measurements." *J.Appl.Geophys.,* 73(1), 45-48.

McCann, D. M. and Forde, M. C. (2001). "Review of NDT methods in the assessment of concrete and masonry structures." *NDT&E Int.,* 34(2), 71-84.

National Park Service. (2014). "Historic Railroad Trail." http://www.nps.gov/lake/planyourvisit/hikerr.htm (August, 19, 2014).

Orlando, L., Pezone, A., and Colucci, A. (2010). "Modeling and testing of high frequency GPR data for evaluation of structural deformation." *NDT&E Int.,* 43(3), 216-230.

Owen, R. D. (1998). "Portable linear accelerators for X-ray and electron-beam applications in civil engineering." *NDT&E Int.,* 31(6), 401-409.

Parkinson, G. and Ekes, C. (2008). "Ground Penetrating Radar Evaluation of Concrete Tunnel Linings." *12th International Conference on Ground Penetrating Radar*.

Rappaport, C., Holbrook, D., Adams, C., Busuioc, D., and Doughty, J. (2010). "Road surface quality measurement using inexpensive radar." *2010 IEEE International Geoscience and Remote Sensing Symposium,* 4318-4321.

Rens, K. and Kim, T. (2007). "Inspection of Quebec Street Bridge in Denver, Colorado: Destructive and Nondestructive Testing." *J.Perform.Constr.Facil.,* 21(3), 215-224.

Song, K., and Cho, G. (2009). "Bonding state evaluation of tunnel shotcrete applied onto hard rocks using the impact-echo method." *NDT&E Int.,* 42(6), 487-500.

SPACETEC. (2014). "SPACETEC Datengewinnung GmbH." http://www.spacetec.de/index-englisch.html (July 23, 2014).

Townsend, B. F. and Speers, C. R. (2007). "Introductory tunnel design - Lining types and selection: A case history of large span soft ground tunnel design." *Underground Space – the 4th Dimension of Metropolises,* 1 745-749.

USDOT. (2005). *Highway and Rail Transit Tunnel Inspection Manual (2005 Edition).* U.S. Department of Transportation.

Wang, F., He, S., Liu, J., and Qi, F. (2012). "Application of Ground Penetrating Radar for Quality Detection of Tunnel Lining." *Advanced Materials Research,* 503(2), 1655-1659.

Weather Underground. (2014). "Weather History for Moab, Utah." http://www.wunderground.com/history/airport/KCNY/2014/7/16/DailyHistory.html?req_city=NA&req_state=NA&req_statename=NA (9/18, 2014).

White, J., Hurlebaus, S., Shokouhi, P., Wittwer, A., and Wimsatt, A. (2014). "Noncontact techniques for monitoring of tunnel linings." *Structural Monitoring and Maintenance,* 1(2), 197-211.

Wimsatt, A., White, J., Leung, C., Scullion, T., Hurlebaus, S., Zollinger, D., Grasley, Z., Nazarian, S., Azari, H., and Yuan, D. (2013). "Mapping Voids, Debonding, Delaminations, Moisture, and Other Defects Behind or Within Tunnel Linings." *Rep. No. SHRP 2 Final Report S2-R06(G)-RW,* Strategic Highway Research Program 2, Washington, D.C.

www.railway-technology.com. "Great Belt Fixed Link, Denmark." http://www.railway-technology.com/projects/denmark/ (June 25, 2014).

APPENDIX A

Slab Testing Results

Table A.1. Slab overview

Specimen	Material	Actual				Measured					Difference****			
		Specimen Depth (mm)	Reinf. Detail (mm)	Defects	True Depth of Defects (mm)	Specimen Depth (mm)	Reinforcement Depth***		Defect		Specimen Depth (mm)	Reinforcement Depth		Defect Depth (mm)
							Top Layer (mm)	Bottom Layer (mm)	Type	Depth (mm)		Top Layer (mm)	Bottom Layer (mm)	
Alpha	Concrete	305	None	None	---	325	None	None	None	---	-20	---	---	---
Beta	Concrete	457	127*	Natural Crack	---	450	121	376	None	---	7	6	-46	---
Gamma	Concrete	305	127*	None	---	300	127	236	None	---	5	0	-58	---
Delta	Concrete	610	None	None	---	636	None	None	None	---	-26	---	---	---
Epsilon	Concrete	610	127*	None	---	620	129	None	None	---	-10	-2	Missed	---
Zeta	Concrete	381	127*	None	---	367	121	291	None	---	14	6	-37	---
Eta	Concrete	381	127*	0.05 mm thin plastic	51	369	124	312	Delamination	72	12	3	-58	-21
Theta	Concrete	381	127*	0.05 mm thin plastic	76	367	127	294	Delamination	98	14	0	-40	-22
Iota	Concrete	381	127*	0.05 mm thin plastic	25	355	124	271	Delamination	34	26	3	-17	-9
Kappa	Concrete	381	127*	Air-filled void (13mm foam)	203	375	127	274	Void	210	6	0	-20	-7
Lambda	Concrete	381	127*	Water-filled void (Ziploc bag)	203	367	118	268	Void	213	14	9	-14	-10
A	Shotcrete	102	None	None	---	98	None	None	None	---	4	---	---	---
B	Shotcrete	152	None	None	---	144	None	None	None	---	8	---	---	---
C	Shotcrete	203	None	None	---	188	None	None	None	---	15	---	---	---
D	Shotcrete	305	**	Air-filled void (13mm foam)	193	291		170	Void	182	14		---	11
E	Shotcrete	305	**	Water-filled void (Ziploc bag)	191	291		156	Void	196	14		---	-5
F	Shotcrete	305	**	Air-filled void (13mm foam)	76	297		164	Void	78	8		---	-2
G	Shotcrete	305	**	Water-filled void (Ziploc bag)	76	277		147	Void	83	28		---	-7
H	Shotcrete	305	**	0.25 mm thin cloth	203	268		150	Delamination	190	37		---	13
I	Shotcrete	305	**	0.25 mm thin cloth	102	283		158	Delamination	95	22		---	7
J	Shotcrete	305	**	0.25 mm thin cloth	76	289		167	Delamination	83	16		---	-7
K	Shotcrete	305	**	0.25 mm thin cloth	51	280		156	Delamination	68	25		---	-17
L	Shotcrete	305	**	0.25 mm thin cloth	25	277		150	Delamination	15	28		---	10
M	Shotcrete	305	**	None	---	277		158	None	---	28		---	---

*Two mats of No. 5 Rebar, at depth from top and bottom, and spaced 203 mm on center

**One lattice girder in center of slab, sitting on bottom form

*** Concrete layers are believed to be mat reinforcement, and the shotcrete slabs seem to have a single girder reinforcement in the lateral direction at the specified depth

****Negative value means measured value is deeper

76
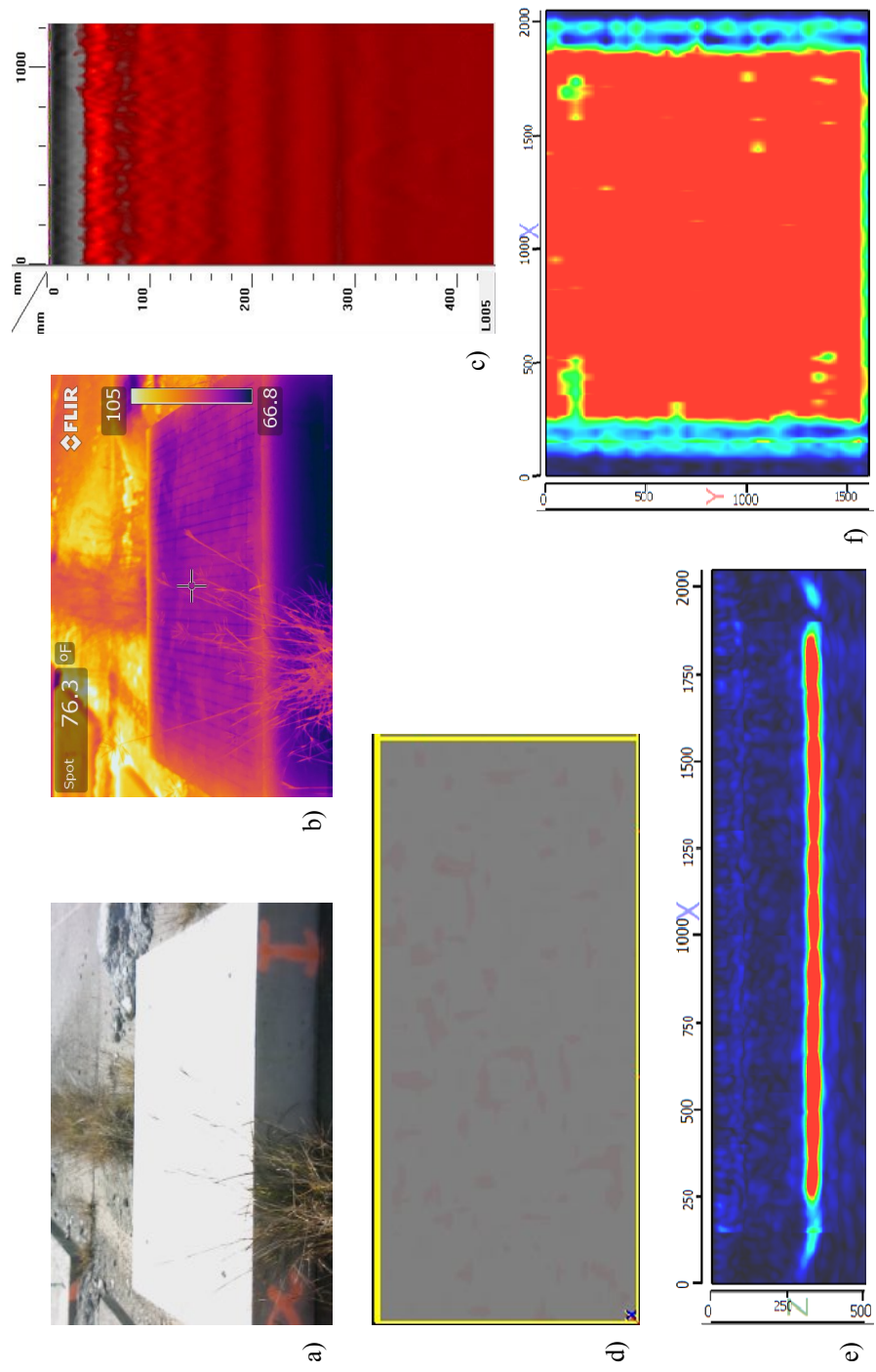
Figure A.1. Specimen Alpha with no defect: a) Image, b) Thermal image, c) GPR B-scan, d) GPR C-scan, e) UST B-scan, and f) UST C-scan
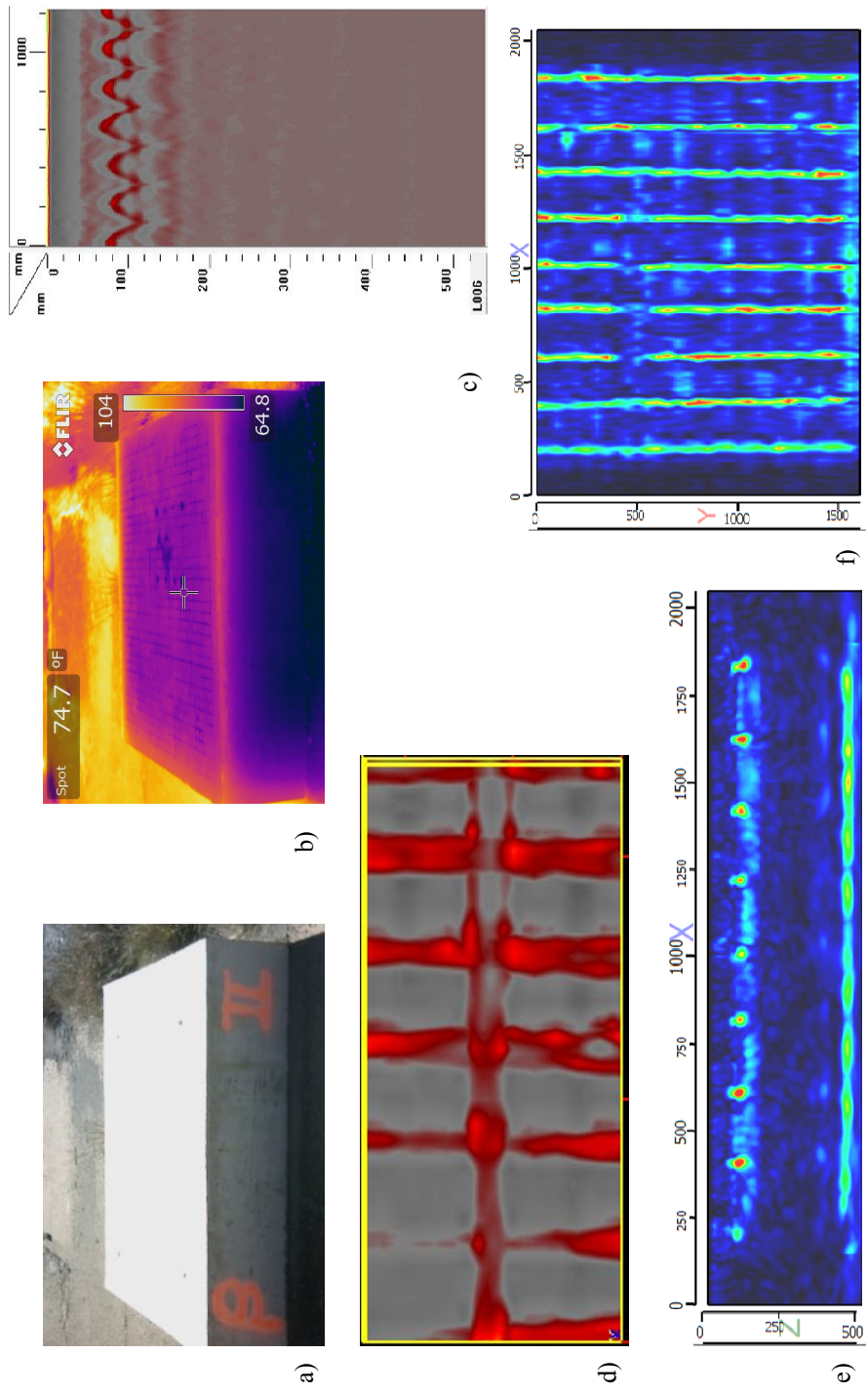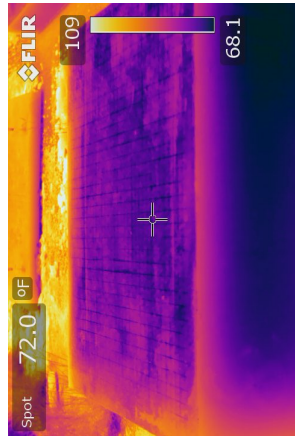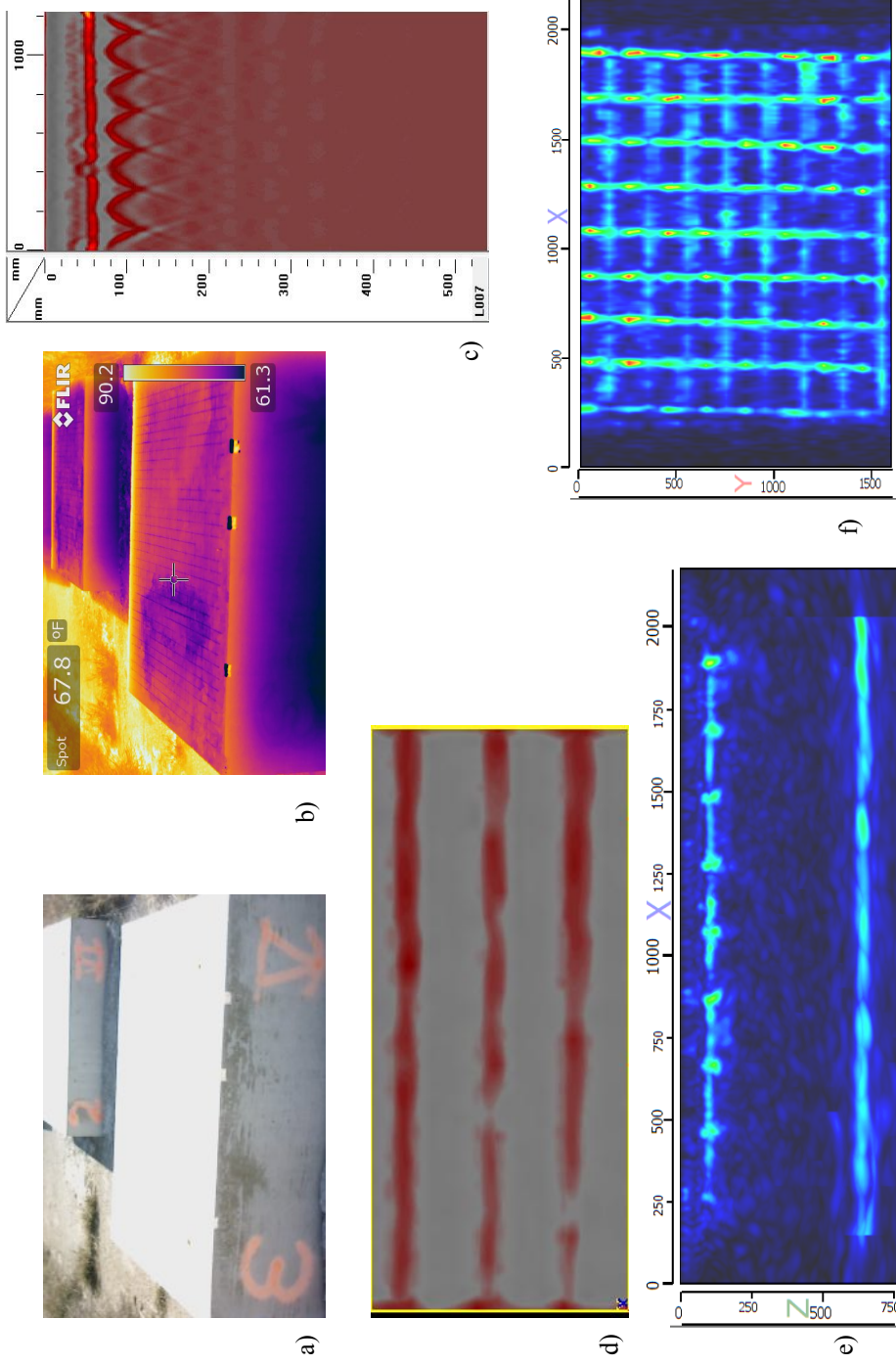
Figure A.2. Specimen Beta with no defect: a) Image, b) Thermal image, c) GPR B-scan, d) GPR C-scan, e) UST B-scan, and f) UST C-scan
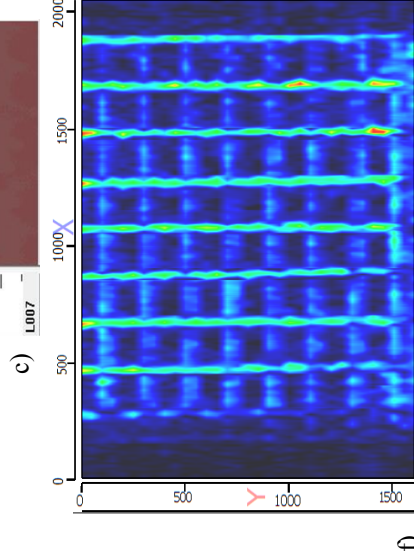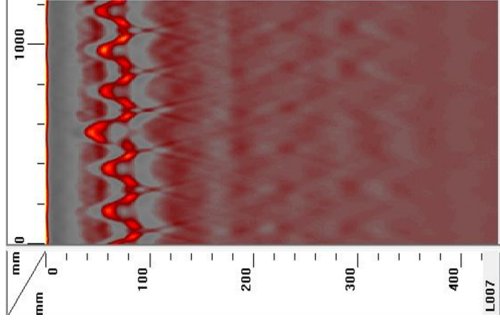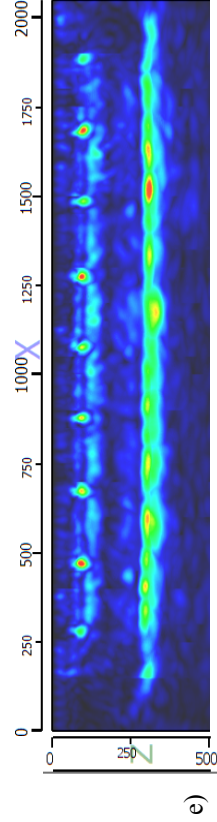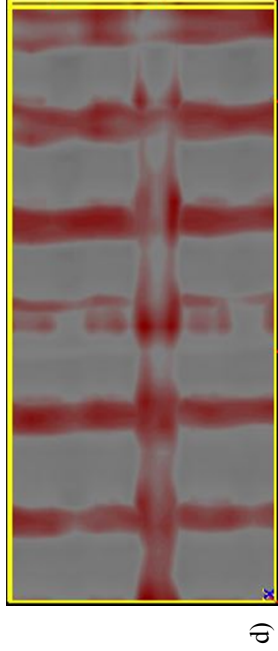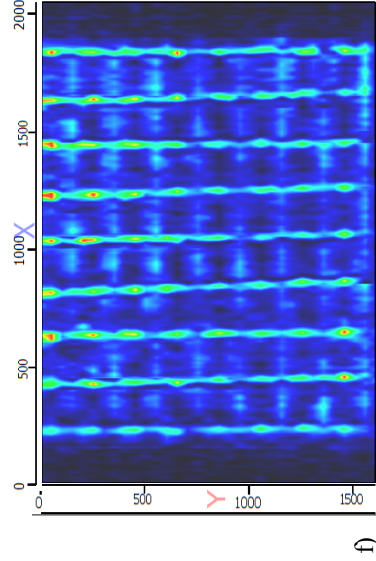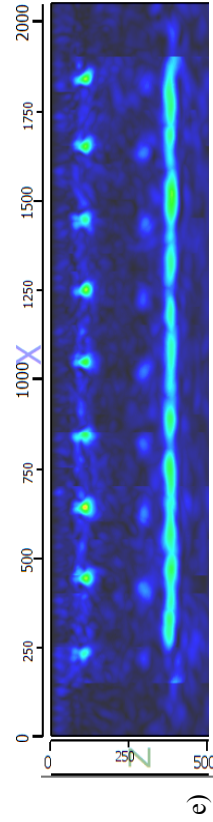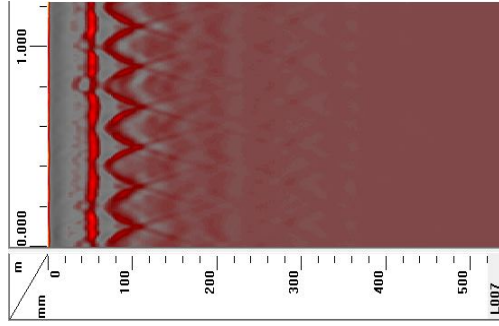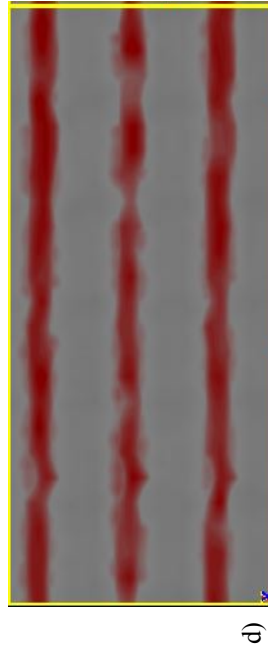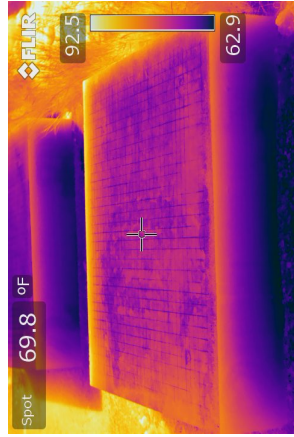
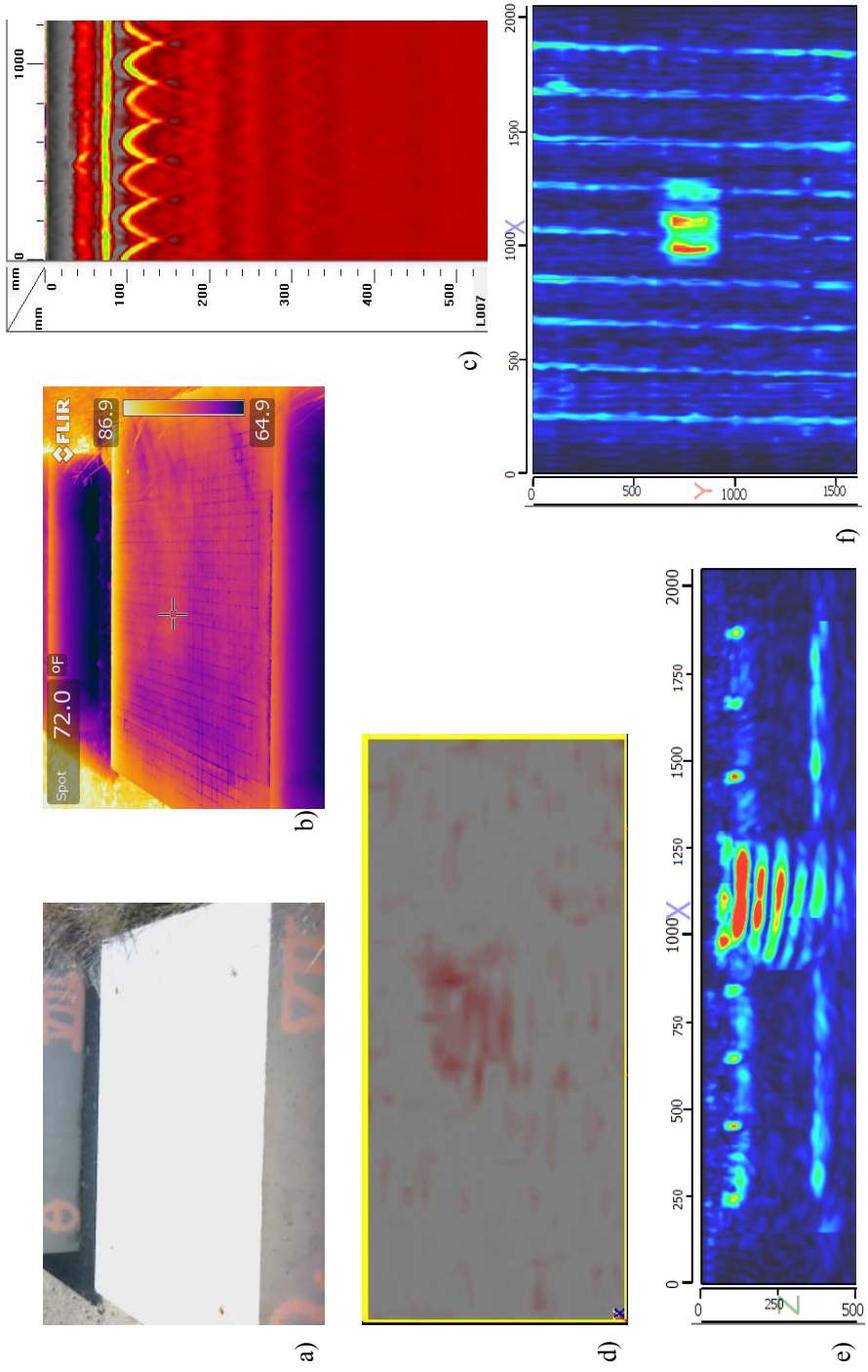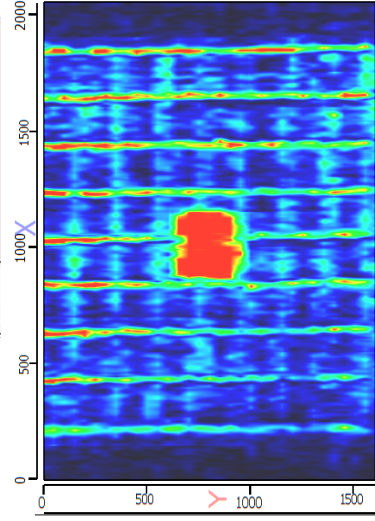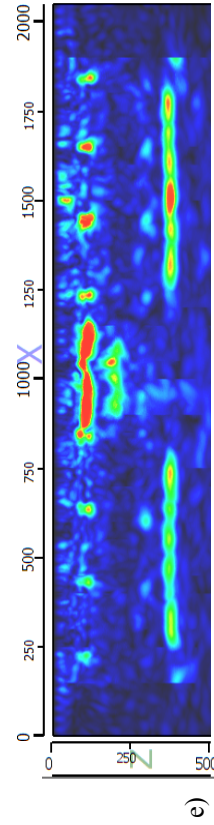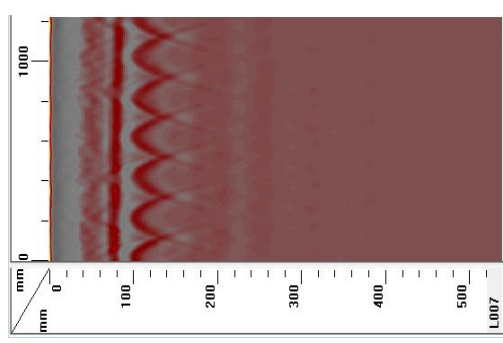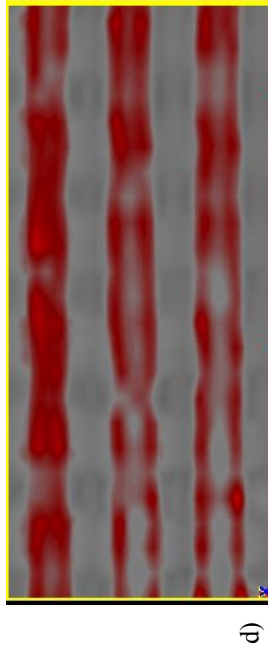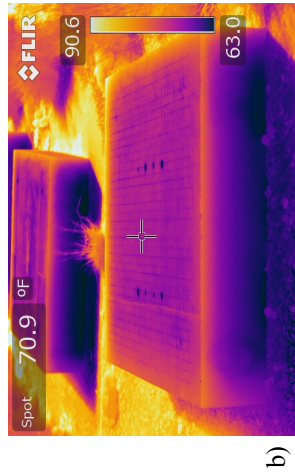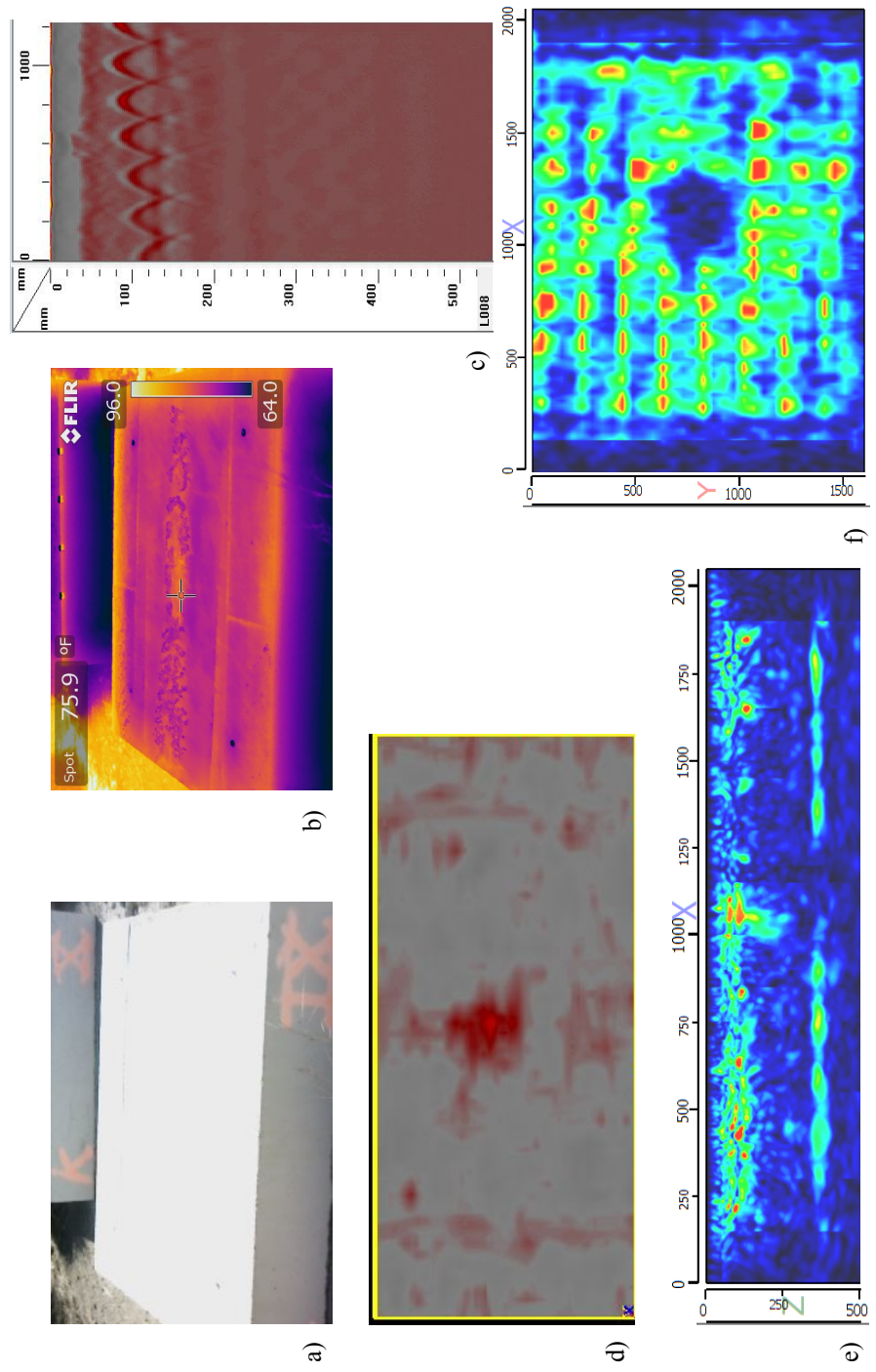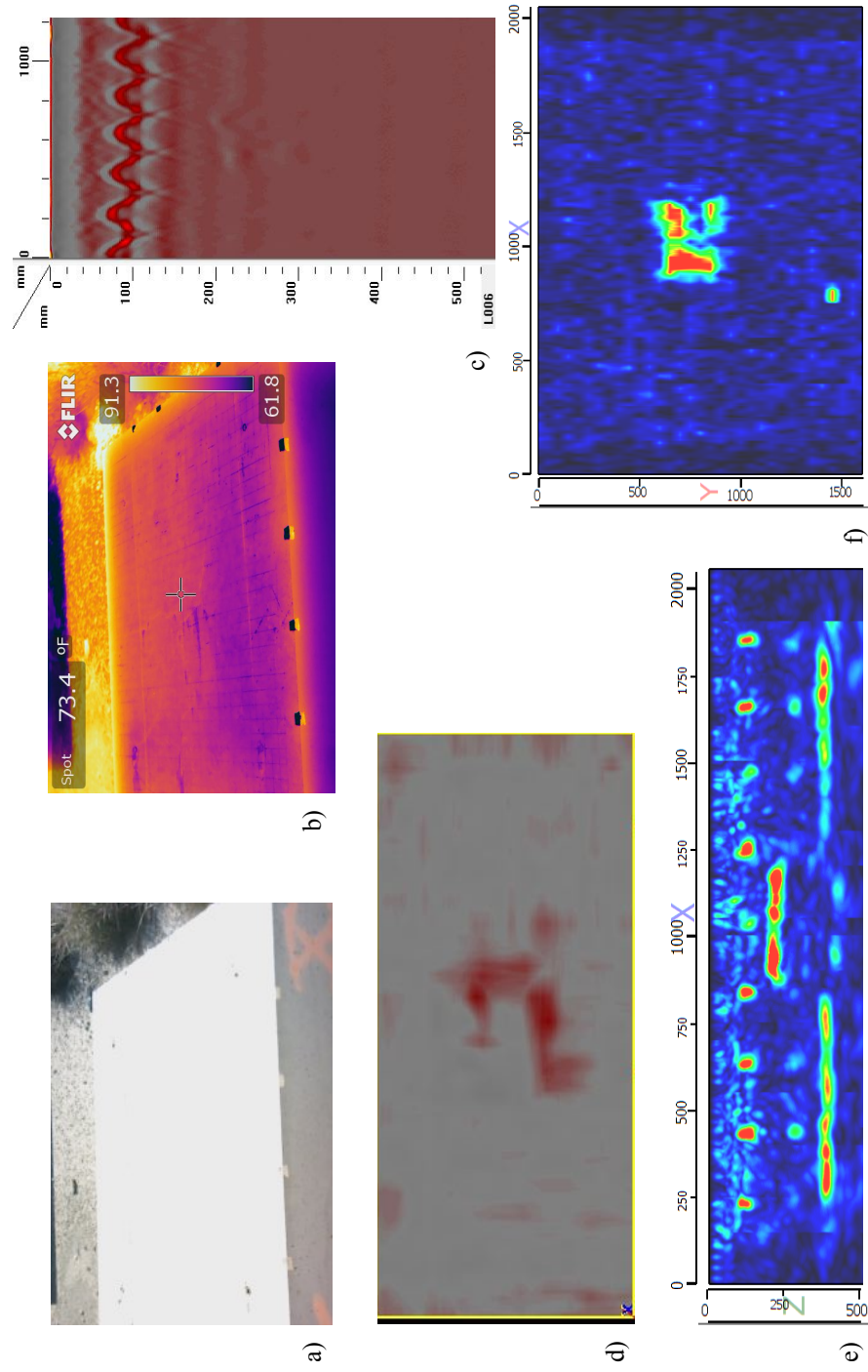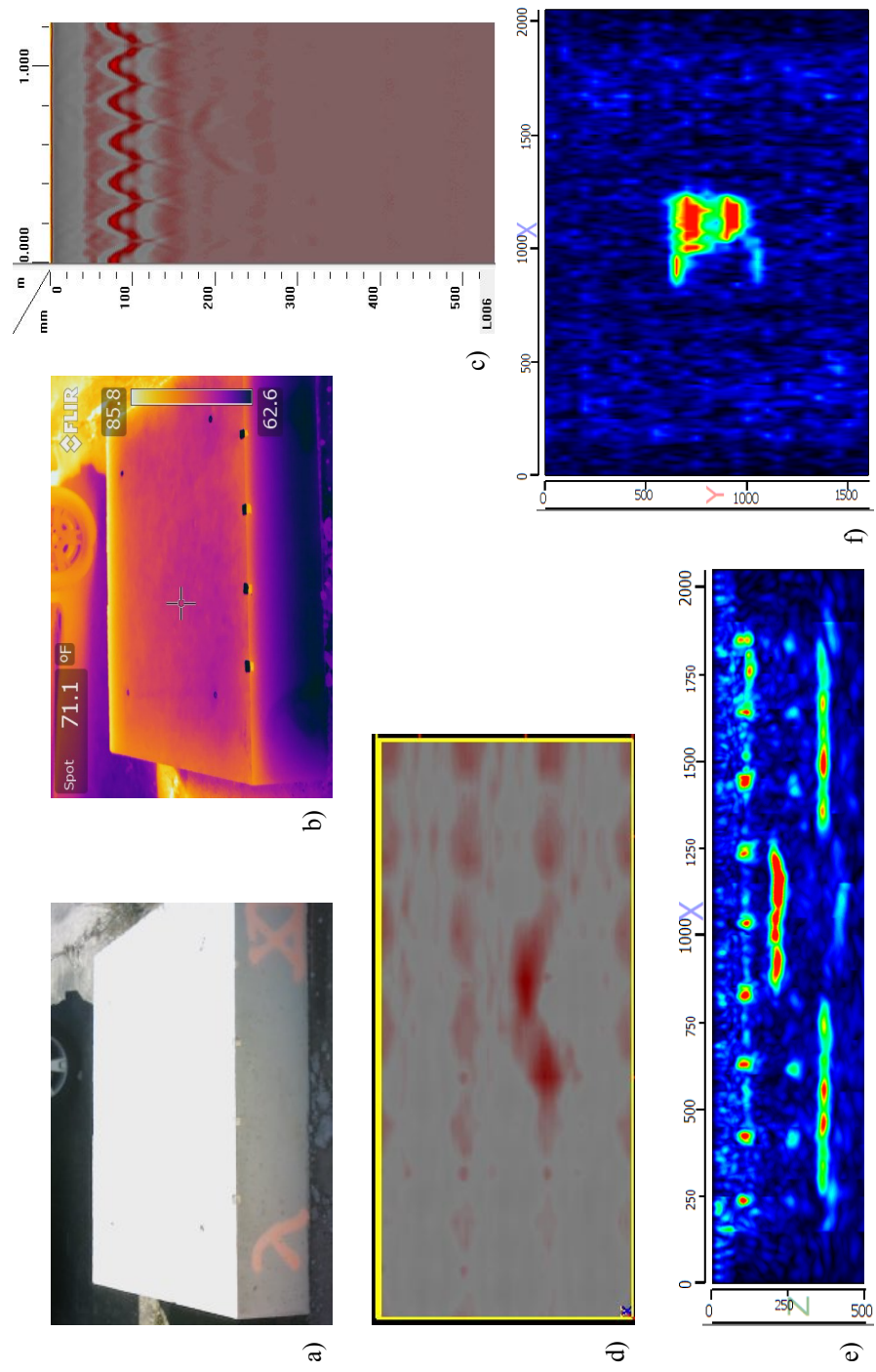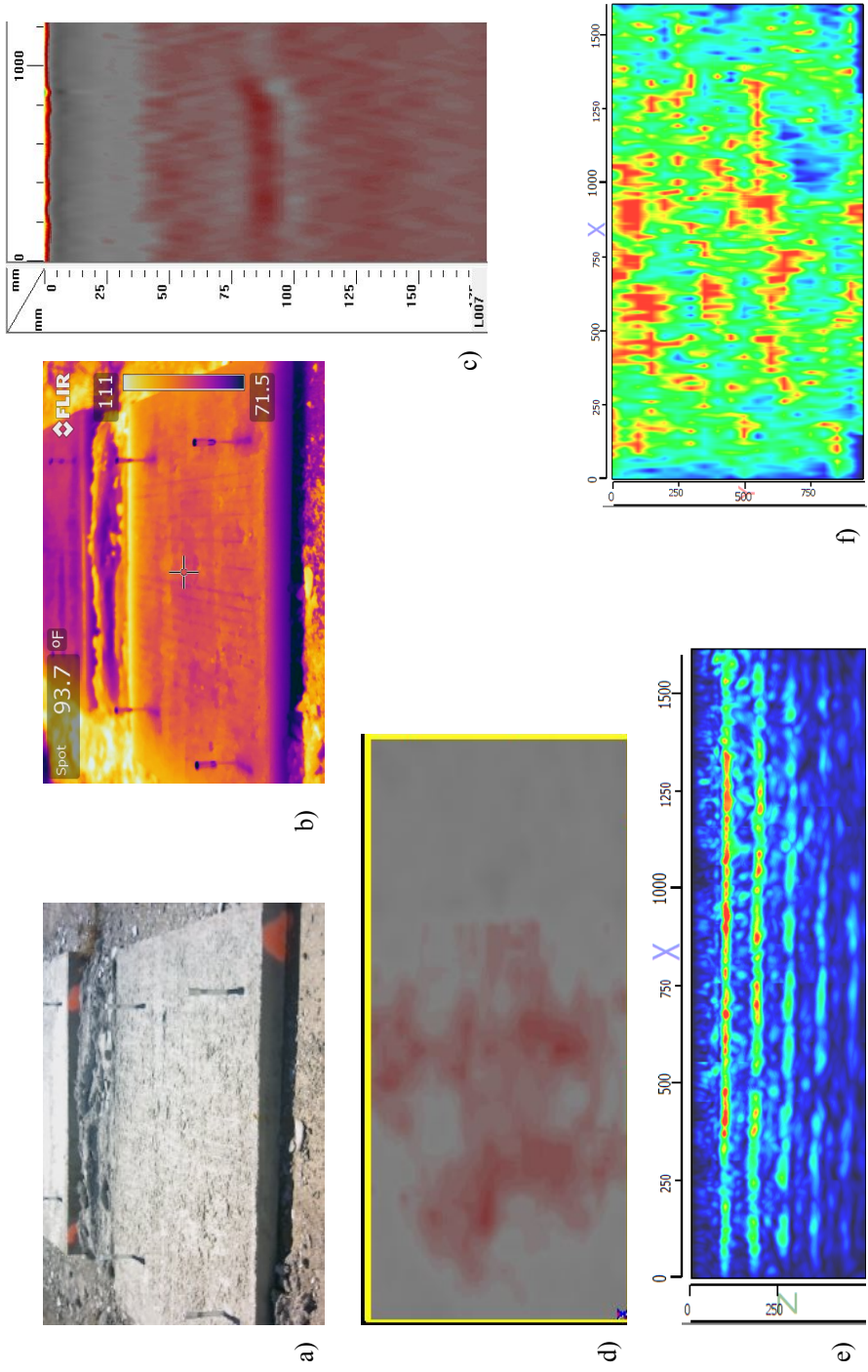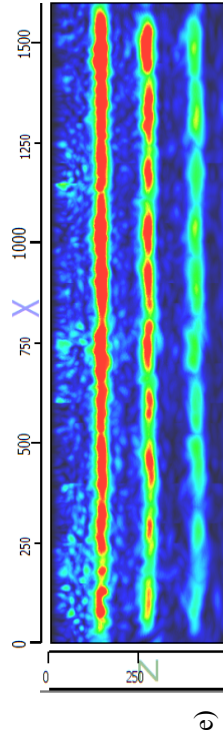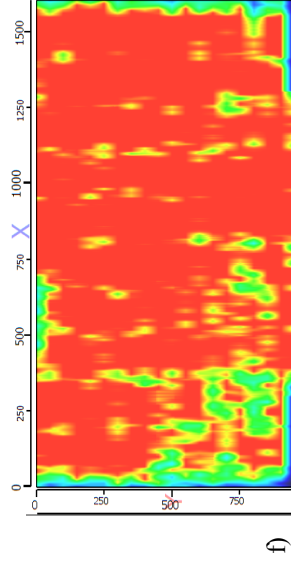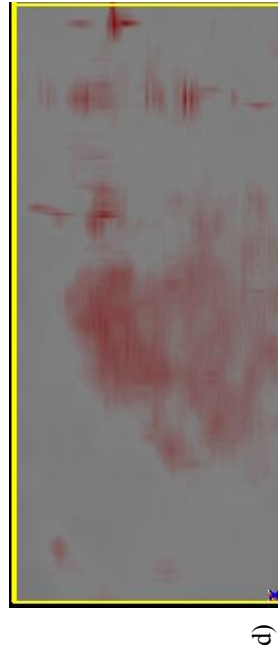Figure A.3. Specimen Gamma with no defect: a) Image, b) Thermal image, c) GPR B-scan, d) GPR C-scan, e) UST B-scan, and f) UST C-scan
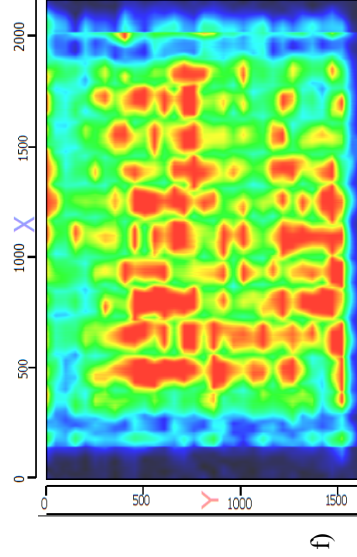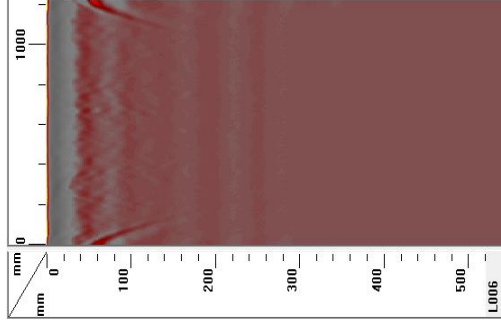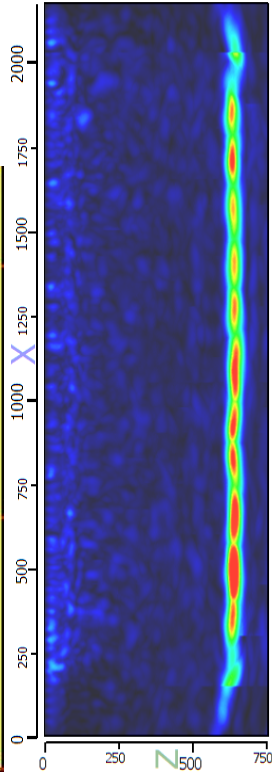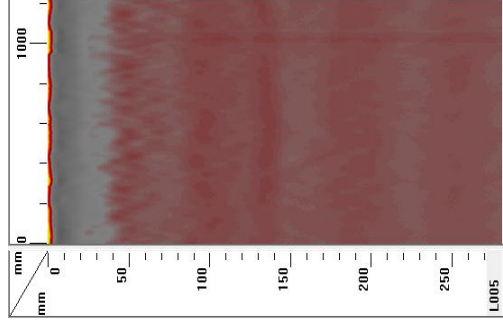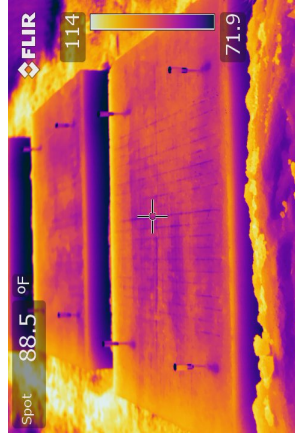
Figure A.4. Specimen Delta with no defect: a) Image, b) Thermal image, c) GPR B-scan, d) GPR C-scan, e) UST B-scan, and f) UST C-scan

Figure A.5. Specimen Epsilon with no defect: a) Image, b) Thermal image, c) GPR B-scan, d) GPR C-scan, e) UST B-scan, and f) UST C-scan
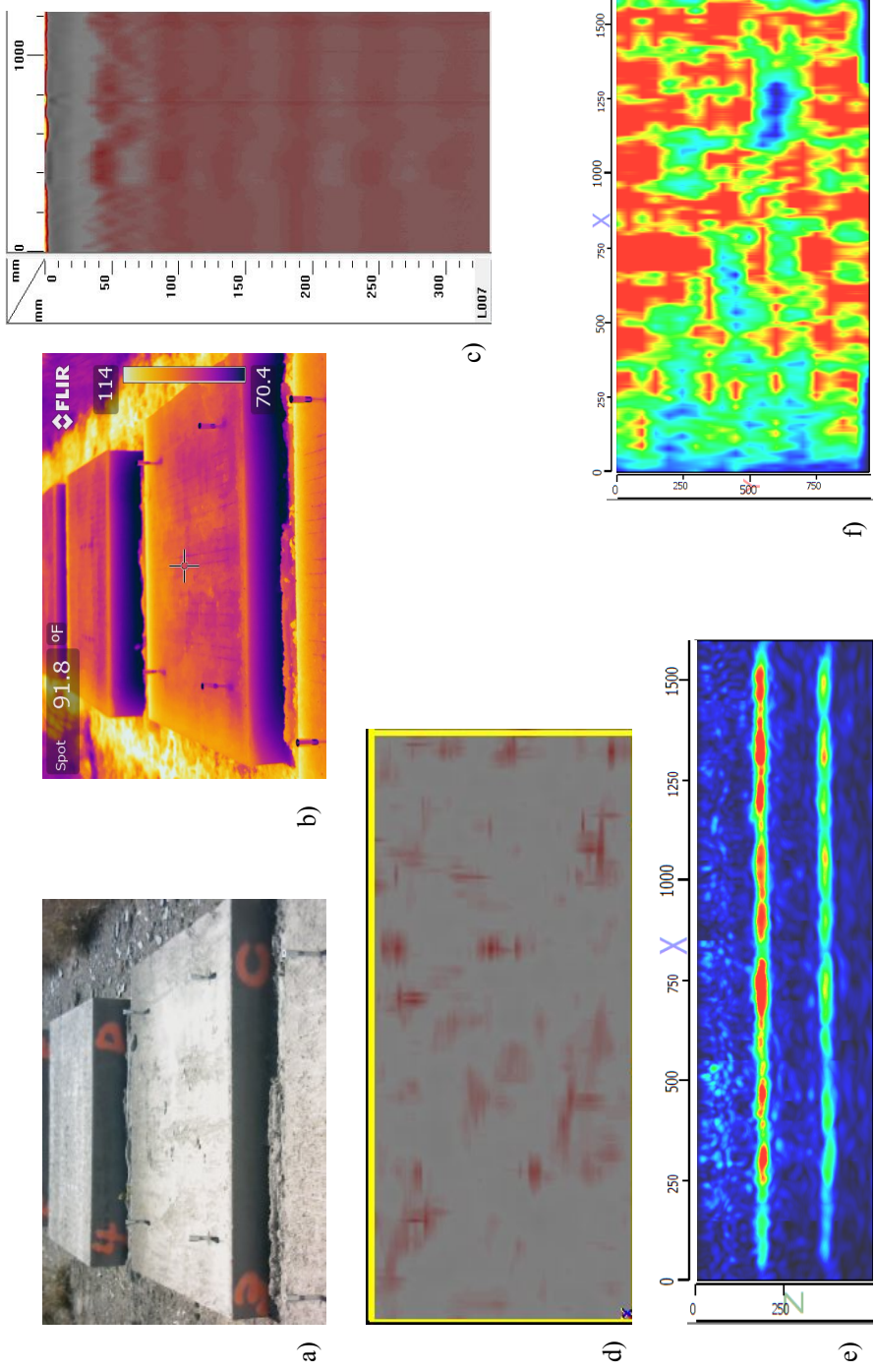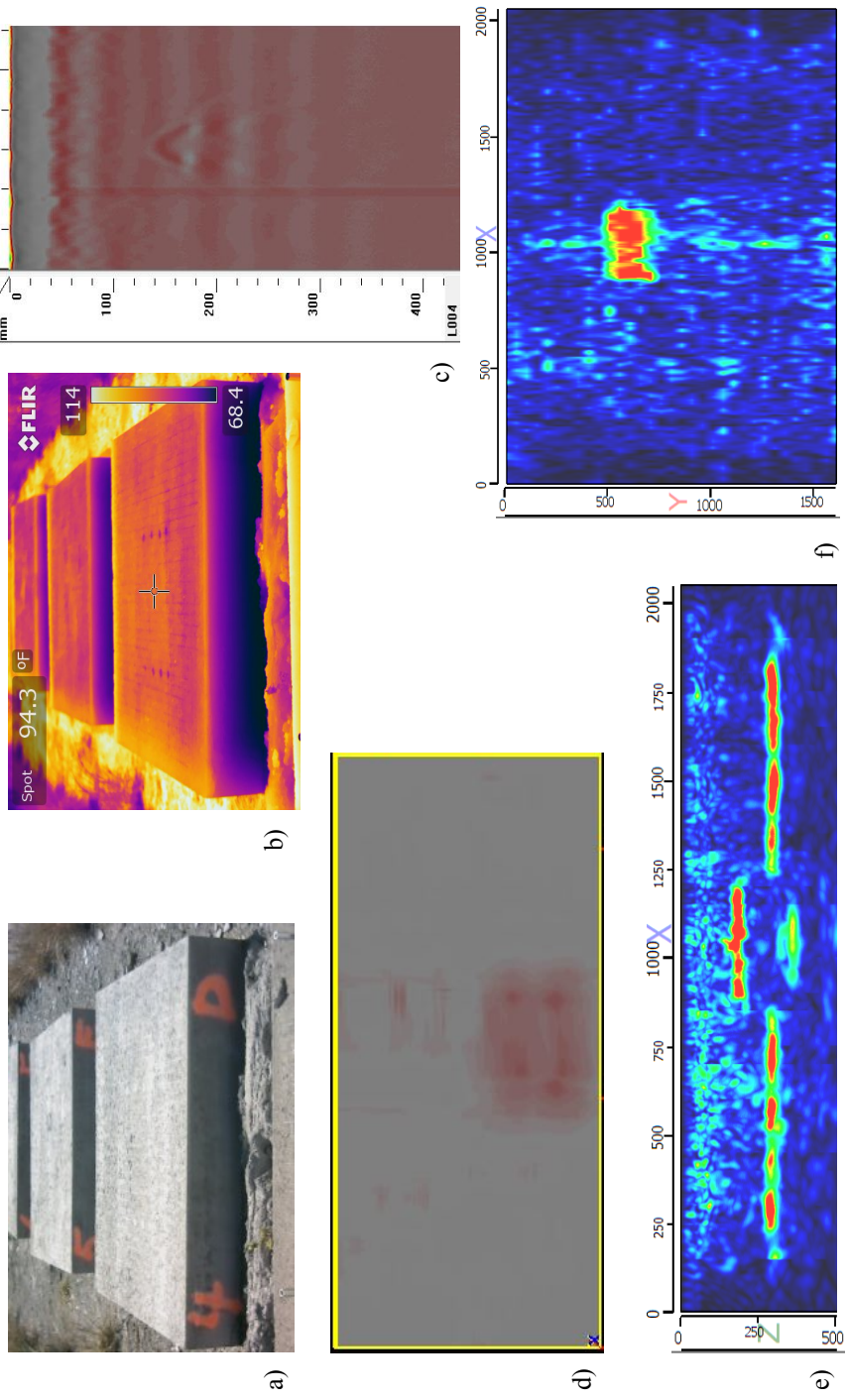
81

Figure A.6. Specimen Zeta with no defect: a) Image, b) Thermal image, c) GPR B-scan, d) GPR C-scan, e) UST B-scan, and f) UST C-scan

Figure A.7. Specimen Eta with a delamination at 72 mm: a) Image, b) Thermal image, c) GPR B-scan, d) GPR C-scan, e) UST B-scan, and f) UST C-scan

Figure A.8. Specimen Theta with a delamination at 98 mm: a) Image, b) Thermal image, c) GPR B-scan, d) GPR C-scan, e) UST B-scan, and f) UST C-scan

a)

b)

c)

d)

e)

f)

Figure A.9. Specimen Iota with a delamination at 34 mm: a) Image, b) Thermal image, c) GPR B-scan, d) GPR C-scan, e) UST B-scan, and f) UST C-scan

Figure A.10. Specimen Kappa with a void at 210 mm: a) Image, b) Thermal image, c) GPR B-scan, d) GPR C-scan, e) UST B-scan, and f) UST C-scan
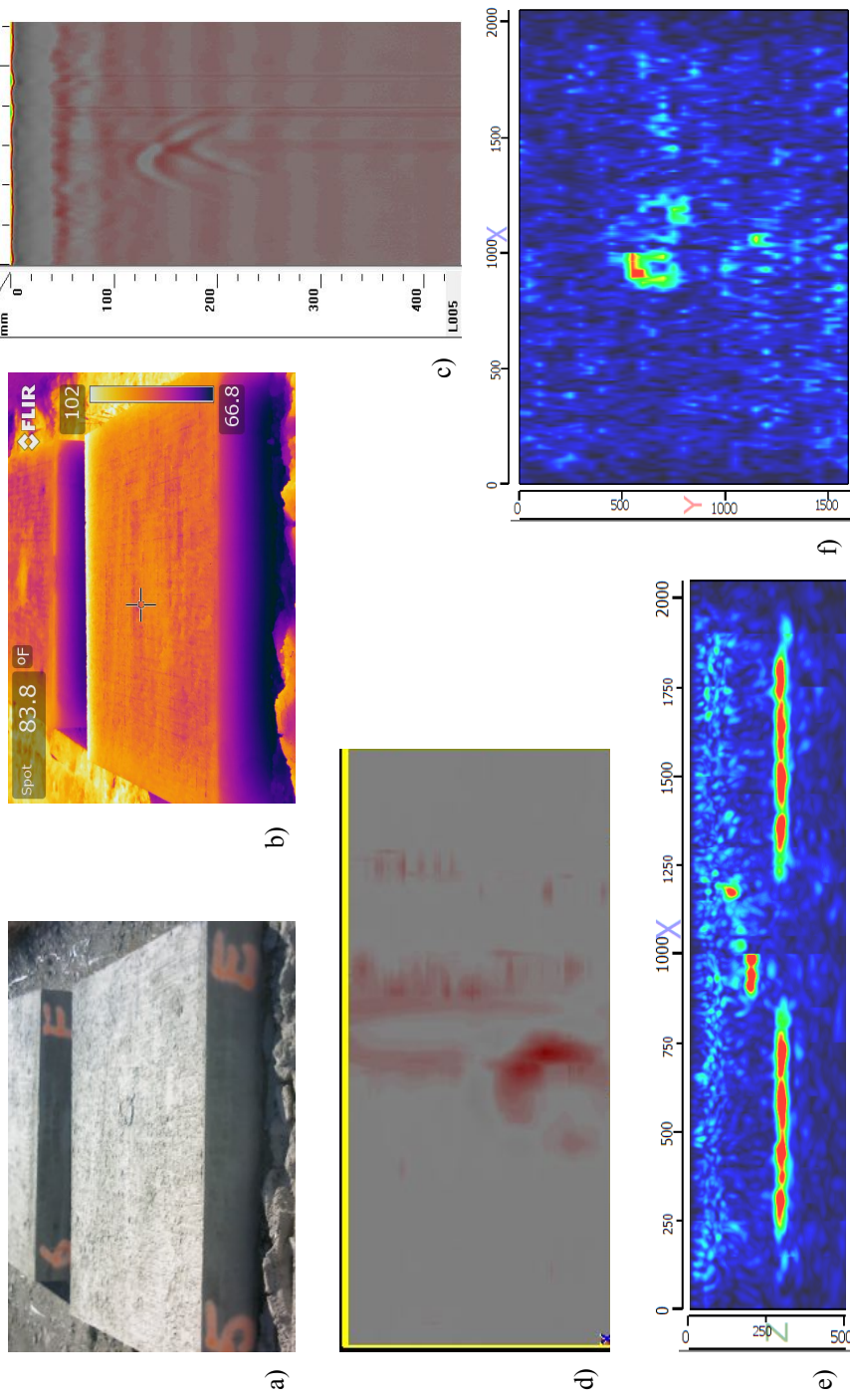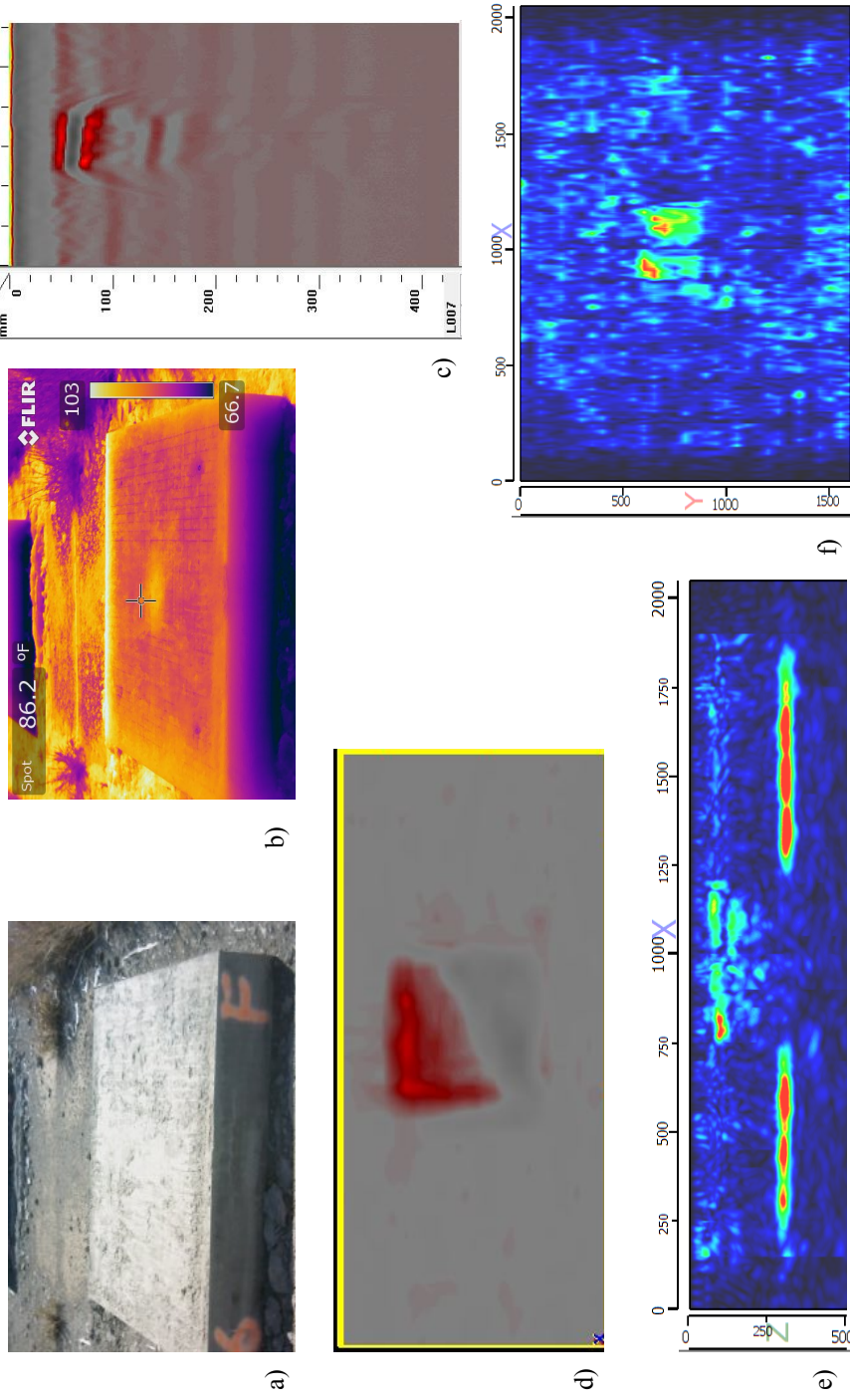
86

Figure A.11. Specimen Lambda with a void at 213 mm: a) Image, b) Thermal image, c) GPR B-scan, d) GPR C-scan, e) UST B-scan, and f) UST C-scan

Figure A.12. Specimen A with no defect: a) Image, b) Thermal image, c) GPR B-scan, d) GPR C-scan, e) UST B-scan, and f) UST C-scan

Figure A.13. Specimen B with no defect: a) Image, b) Thermal image, c) GPR B-scan, d) GPR C-scan, e) UST B-scan, and f) UST C-scan

Figure A.14. Specimen C with no defect: a) Image, b) Thermal image, c) GPR B-scan, d) GPR C-scan, e) UST B-scan, and f) UST C-scan

Figure A.15. Specimen D with a void at 182 mm: a) Image, b) Thermal image, c) GPR B-scan, d) GPR C-scan, e) UST B-scan, and f) UST C-scan
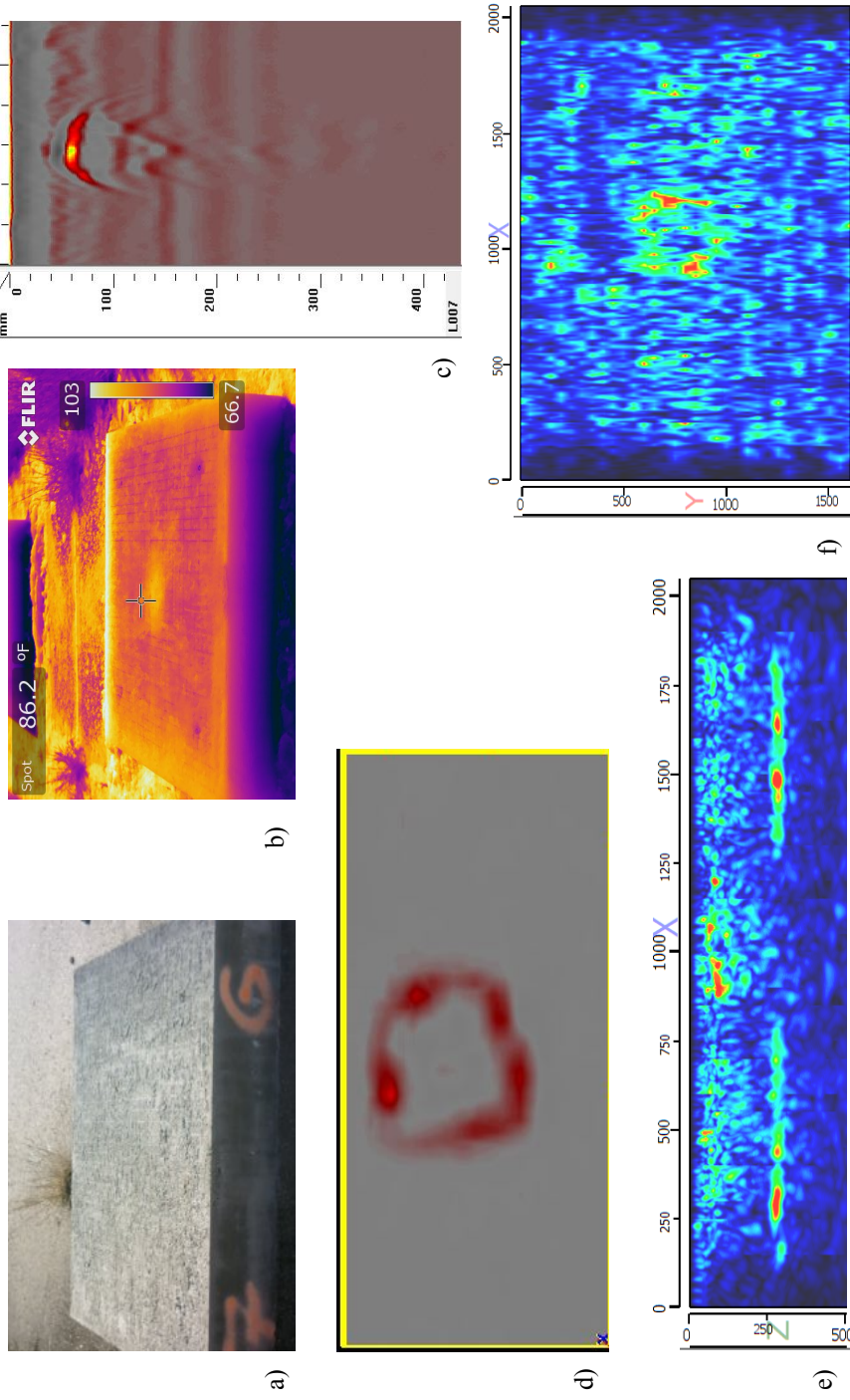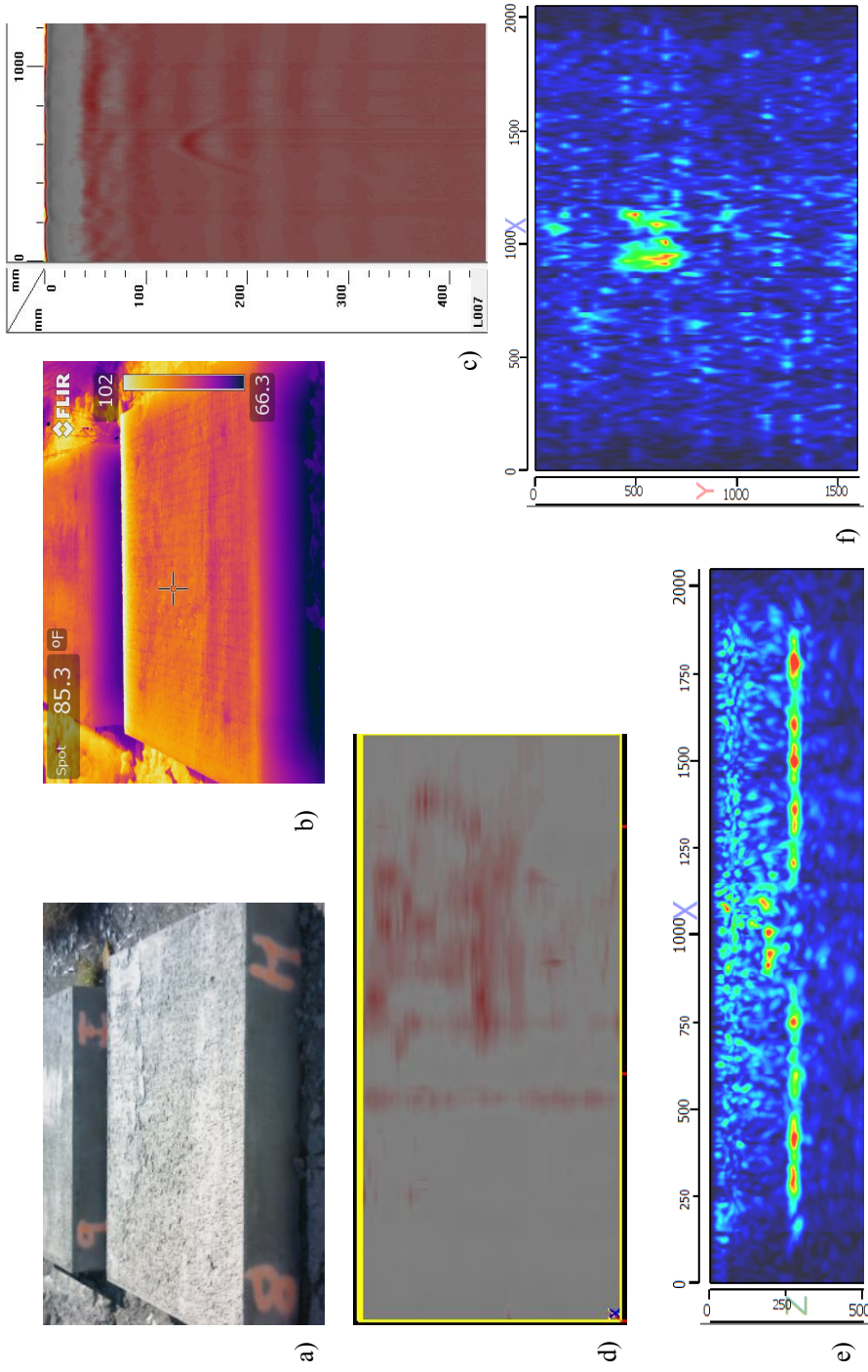
Figure A.16. Specimen E with a void at 196 mm: a) Image, b) Thermal image, c) GPR B-scan, d) GPR C-scan, e) UST B-scan, and f) UST C-scan

Figure A.17. Specimen F with a void at 78 mm: a) Image, b) Thermal image, c) GPR B-scan, d) GPR C-scan, e) UST B-scan, and f) UST C-scan

Figure A.18. Specimen G with a void at 83 mm: a) Image, b) Thermal image, c) GPR B-scan, d) GPR C-scan, e) UST B-scan, and f) UST C-scan

94

Figure A.19. Specimen H with a delamination at 190 mm: a) Image, b) Thermal image, c) GPR B-scan, d) GPR C-scan, e) UST B-scan, and f) UST C-scan
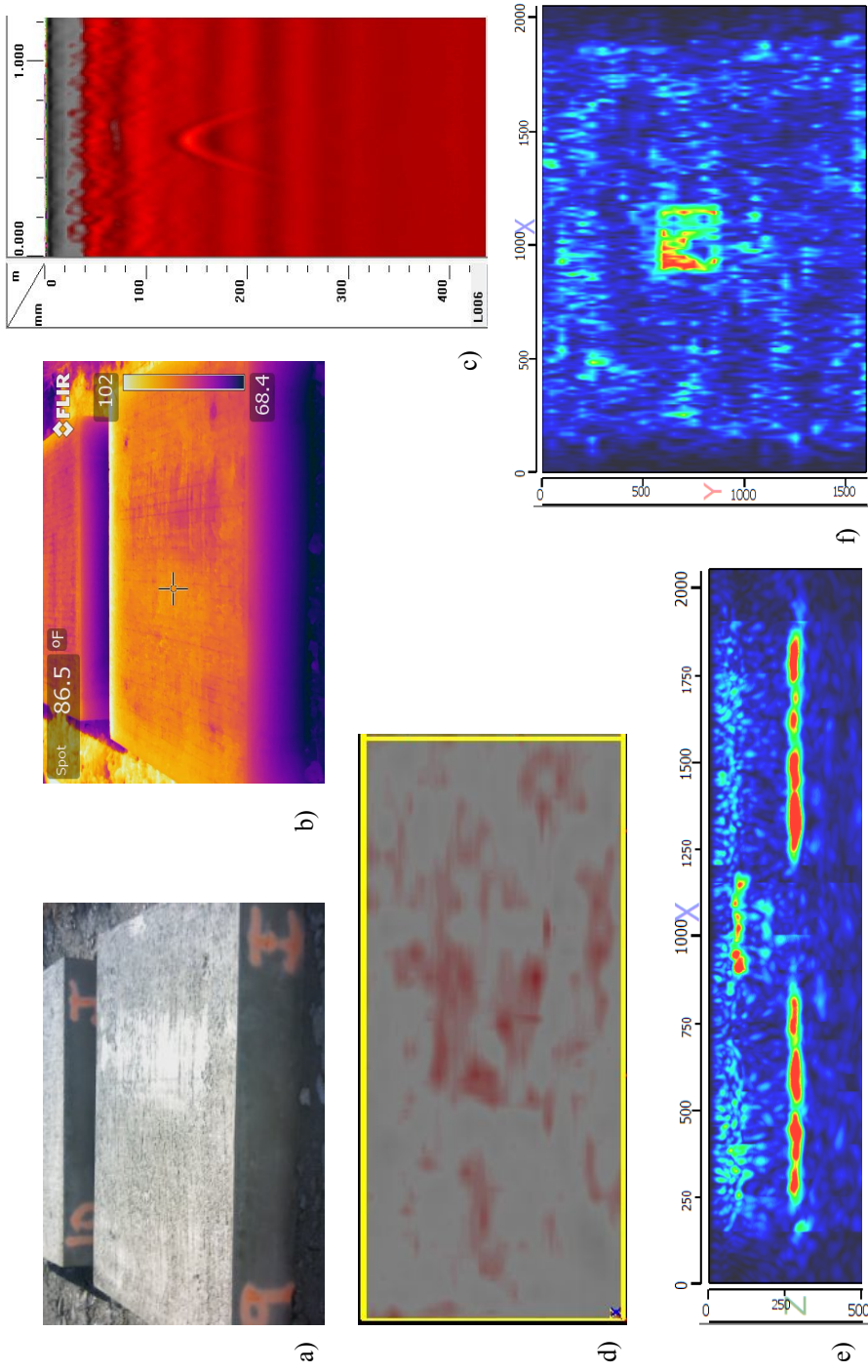
95

Figure A.20. Specimen I with a delamination at 95 mm: a) Image, b) Thermal image, c) GPR B-scan, d) GPR C-scan, e) UST B-scan, and f) UST C-scan
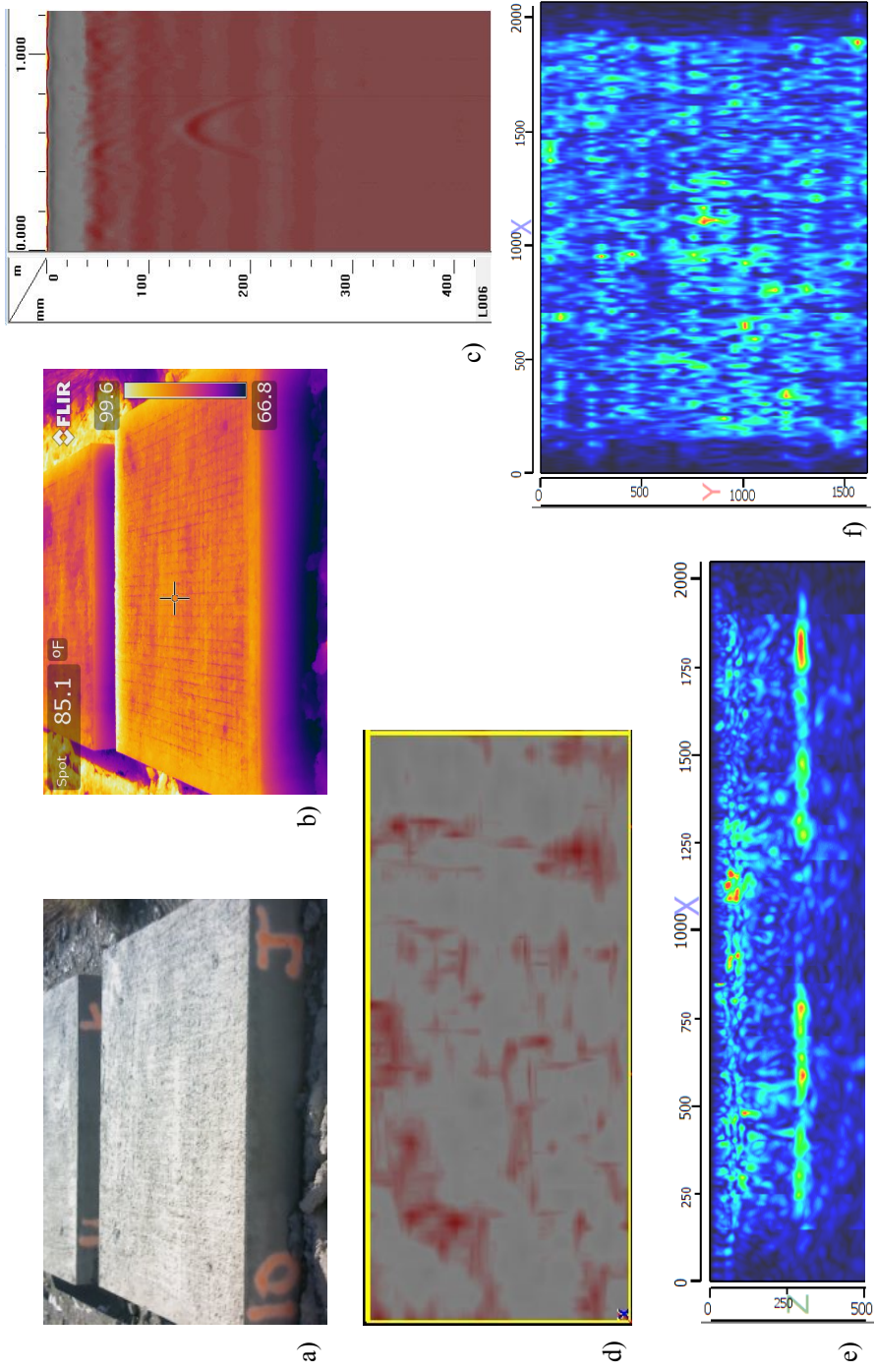
Figure A.21. Specimen J with a delamination at 83 mm: a) Image, b) Thermal image, c) GPR B-scan, d) GPR C-scan, e) UST B-scan, and f) UST C-scan
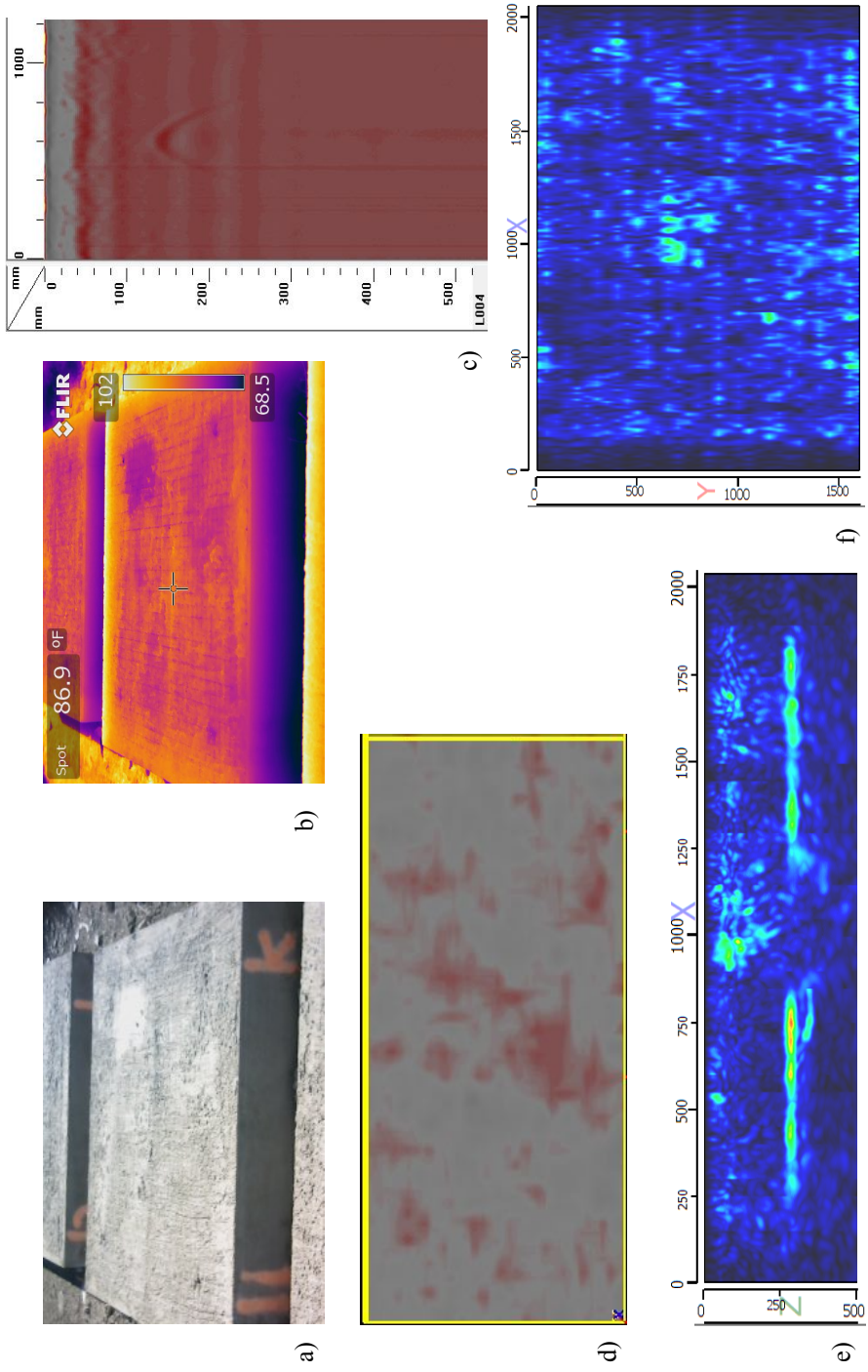
Figure A.22. Specimen K with a delamination at 68 mm: a) Image, b) Thermal image, c) GPR B-scan, d) GPR C-scan, e) UST B-scan, and f) UST C-scan
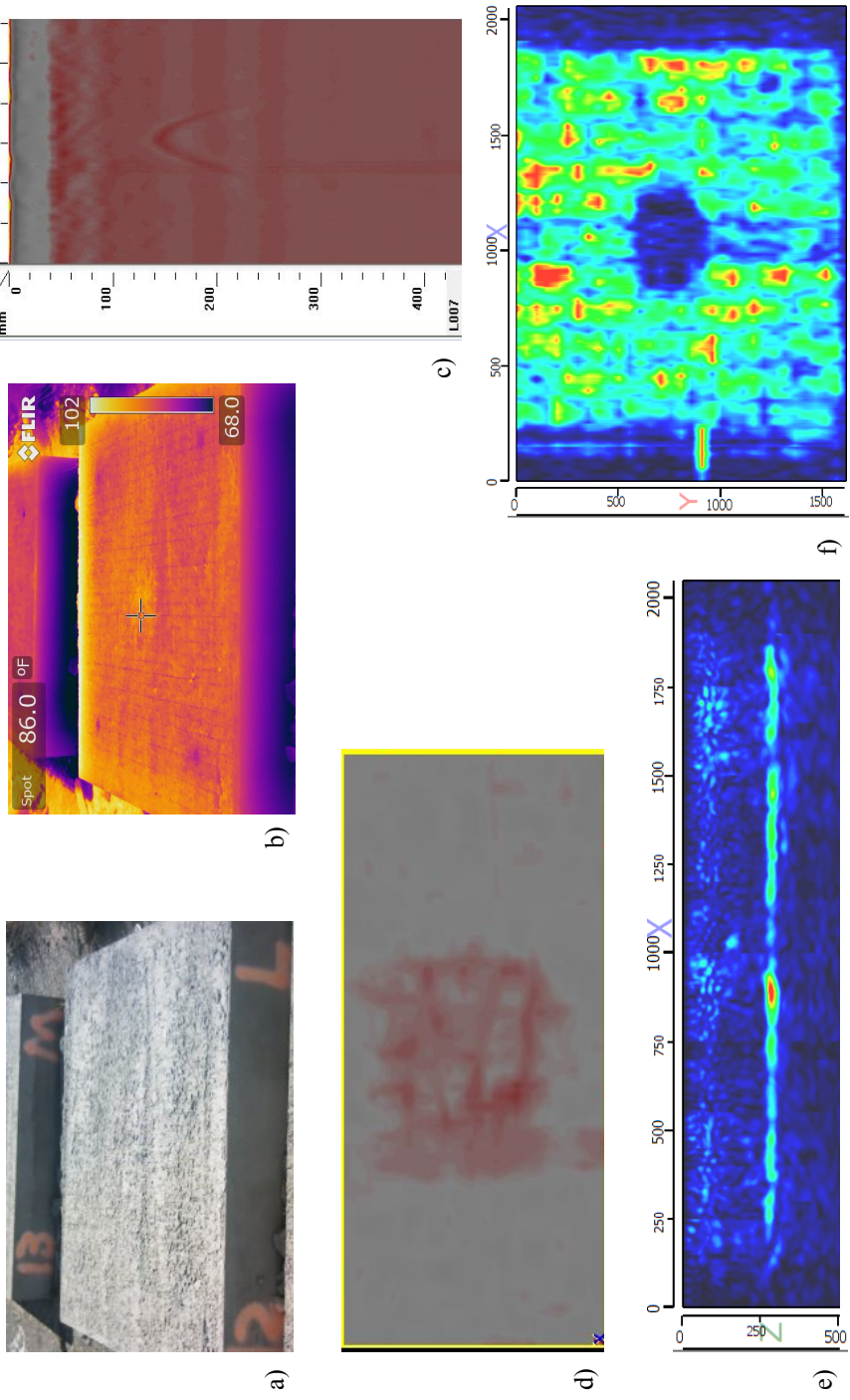
Figure A.23. Specimen L with a delamination at 15 mm: a) Image, b) Thermal image, c) GPR B-scan, d) GPR C-scan, e) UST B-scan, and f) UST C-scan
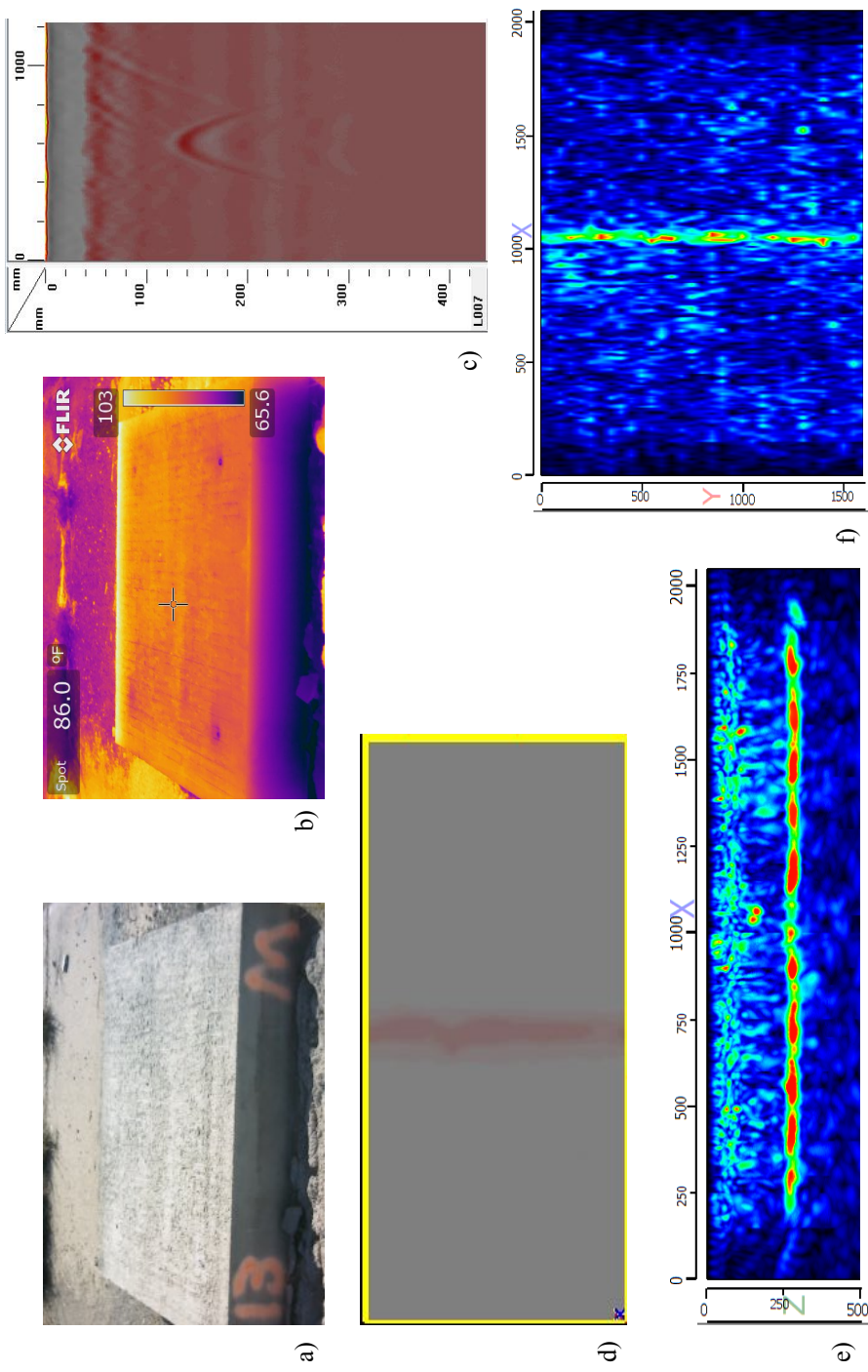
Figure A.24. Specimen M with no defect: a) Image, b) Thermal image, c) GPR B-scan, d) GPR C-scan, e) UST B-scan, and f) UST C-scan